

THESIS FOR THE DEGREE OF DOCTOR OF PHILOSOPHY

Quantum Hall devices on epitaxial graphene:  
towards large-scale integration

ARSENIY LARTSEV

Quantum Device Physics Laboratory  
Department of Microtechnology and Nanoscience  
CHALMERS UNIVERSITY OF TECHNOLOGY  
Göteborg, Sweden 2015

Quantum Hall devices on epitaxial graphene: towards large-scale  
integration

ARSENIY LARTSEV

ISBN 978-91-7597-262-6

© Arseniy Lartsev, 2015

Doktorsavhandlingar vid Chalmers tekniska högskola

Ny series nr 3943

ISSN 0346-718X

ISSN 1652-0769

Technical Report MC2-317

Quantum Device Physics Laboratory

Department of Microtechnology and Nanoscience – MC2

Chalmers University of Technology

41296 Göteborg, Sweden

Telephone +46(0) 31 772 1000

Cover: false color scanning electron microscopy image of a part of a quantum  
Hall array fabricated on epitaxial graphene.

Chalmers Reproservice

Göteborg, Sweden 2015

# Quantum Hall devices on epitaxial graphene: towards large-scale integration

ARSENIY LARTSEV

Department of Microtechnology and Nanoscience – MC2  
Chalmers University of Technology

## Abstract

Quantum Hall devices have been used as the primary standard of electrical resistance for over two decades, and they are unlikely to be replaced in this role any time soon. The work presented in this thesis was being done towards the goal of establishing epitaxial graphene on silicon carbide as a new material of choice for these devices. Experiments on individual devices have already demonstrated that due to unique electronic properties of graphene and peculiarities of its interaction with the SiC substrate, quantum resistance standards based on epitaxial graphene can operate at higher temperatures, lower magnetic fields, or higher current densities, as compared to their state-of-the-art gallium arsenide counterparts. Here, we were aiming at developing the technology for reliable mass-production of the devices.

One of the issues that we address is the carrier density control. We have found that photochemical gating, a technique which has previously been used for this purpose, becomes unreliable when the electron density needs to be lowered by more than  $10^{16} \text{ m}^{-2}$ . Instead, corona discharge can be used for efficient electrostatic gating, enabling us to sweep the carrier density from  $4 \cdot 10^{16} \text{ electrons}\cdot\text{m}^{-2}$  to  $5 \cdot 10^{16} \text{ holes}\cdot\text{m}^{-2}$  and to observe the quantum Hall effect at low doping.

The presence of bilayer patches in majority-monolayer samples is another important problem. We have observed both metallic and insulating behaviour of these patches while driving the monolayer into the quantum Hall regime. When the bilayer is metallic, we show that a patch completely crossing the Hall bar will break down the quantum Hall effect in a way that agrees with theoretical expectations. Further, we propose imaging these patches by optical microscopy as a way of avoiding them, by selecting substrates where the patches are sufficiently small and sparse. We demonstrate that, despite the optical contrast being less than 2%, the bilayer areas can be imaged in real time using digital post-processing. Also, we show that optical microscopy can be used to detect the steps that form on the SiC surface during graphene growth, and even measure their height: steps as low as 1.5 nm could be clearly seen.

Finally, we have fabricated arrays of 100 Hall bars connected in parallel, devices which provide a low-ohmic quantum standard if every single Hall bar works correctly. We have chosen a substrate with a sufficiently low bilayer content, and adapted the geometry of the Hall bar to the shape of the patches. One out of four devices has performed correctly within the relative measurement precision of  $10^{-4}$  in magnetic fields above 7 tesla. We see this as a confirmation that the quality of graphene was sufficiently high to enable  $\geq 99\%$  yield of working Hall bars.

**Keywords:** epitaxial graphene, magnetotransport, quantum Hall effect, quantum Hall array, resistance metrology.



# Publications

This thesis is based on the work that has been published in the following papers:

- 1. Quantum Hall Effect and Quantum Point Contact in Bilayer-Patched Epitaxial Graphene**  
C. Chua, M. Connolly, A. Lartsev, T. Yager, S. Lara-Avila, S. Kubatkin, S. Kopylov, V. Fal'ko, R. Yakimova, R. Pearce, T. J. B. M. Janssen, A. Tzalenchuk, and C. G. Smith  
Nano Letters 14, 3369–3373 (2014)
- 2. Express Optical Analysis of Epitaxial Graphene on SiC: Impact of Morphology on Quantum Transport**  
T. Yager, A. Lartsev, S. Mahashabde, S. Charpentier, D. Davidovikj, A. Danilov, R. Yakimova, V. Panchal, O. Kazakova, A. Tzalenchuk, S. Lara-Avila, and S. Kubatkin  
Nano Letters 13, 4217–4223 (2013)
- 3. Tuning carrier density across Dirac point in epitaxial graphene on SiC by corona discharge**  
A. Lartsev, T. Yager, T. Bergsten, A. Tzalenchuk, T. J. B. M. Janssen, R. Yakimova, S. Lara-Avila, and S. Kubatkin  
Applied Physics Letters 105 no. 6, 063106 (2014)
- 4. A prototype of  $R_K/200$  quantum Hall array resistance standard on epitaxial graphene**  
A. Lartsev, S. Lara-Avila, A. Danilov, A. Tzalenchuk, R. Yakimova, and S. Kubatkin  
Journal of Applied Physics 118, 044506 (2015)

Other publications that are outside the scope of this thesis:

- **Magnetic Scanning Probe Calibration Using Graphene Hall Sensor**  
V. Panchal, Ó. Iglesias-Freire, A. Lartsev, R. Yakimova, A. Asenjo, and O. Kazakova  
IEEE Transactions on Magnetics 49 no. 7, 3520 (2013)
- **Local electric field screening in bi-layer graphene devices**  
V. Panchal, C. E. Giusca, A. Lartsev, R. Yakimova, and O. Kazakova  
Frontiers in Physics 2:3 (2014)
- **Visualisation of edge effects in side-gated graphene nanodevices**  
V. Panchal, A. Lartsev, A. Manzin, R. Yakimova, A. Tzalenchuk, and O. Kazakova  
Scientific Reports 4, 5881 (2014)

# Contents

<i>Publications</i>	<i>v</i>
<i>List of Figures</i>	<i>ix</i>
<i>Preface</i>	<i>xi</i>
<b>Introduction</b>	<b>1</b>
<b>1 Background and theory</b>	<b>5</b>
1.1 Graphene: basic electronic structure . . . . .	5
1.2 Electron transport in graphene . . . . .	9
1.3 The quantum Hall effect . . . . .	12
1.3.1 The theory of quantum Hall effect . . . . .	14
1.3.2 Current-induced breakdown of quantum Hall effect . .	19
1.4 Quantum Hall effect in graphene . . . . .	21
1.5 Epitaxial graphene on silicon carbide . . . . .	23
1.6 Substrate effects in epitaxial graphene . . . . .	24
1.7 Quantum Hall circuits . . . . .	27
1.7.1 Quantum Hall device as a circuit element . . . . .	28
1.7.2 Quantum Hall arrays . . . . .	29
1.7.3 Bordering QHE domains with different filling factors . .	31
1.8 Optical reflection and absorption of graphene . . . . .	33
<b>2 Experimental techniques</b>	<b>37</b>
2.1 Microfabrication . . . . .	37
2.2 Optical microscopy . . . . .	40
2.2.1 Differential interference contrast . . . . .	40
2.2.2 Transport of intensity phase imaging . . . . .	41
2.2.3 Confocal microscopy . . . . .	43
2.3 Magnetotransport and QHE measurements . . . . .	43

<b>3</b>	<b>Carrier density control</b>	<b>45</b>
3.1	Limitations of photochemical gating . . . . .	46
3.2	Gating by static charge . . . . .	47
<b>4</b>	<b>Effect of bilayer patches</b>	<b>49</b>
4.1	Metallic bilayer . . . . .	49
4.2	Insulating bilayer . . . . .	52
4.3	Bilayer in the quantum Hall regime . . . . .	55
4.4	Summary . . . . .	56
<b>5</b>	<b>Morphology characterization</b>	<b>57</b>
5.1	Optical imaging of the bilayer domains . . . . .	57
5.2	Optical imaging of the steps . . . . .	60
<b>6</b>	<b>Quantum Hall arrays</b>	<b>63</b>
6.1	Device design . . . . .	64
6.1.1	Hall bars and the choice of the substrate . . . . .	64
6.1.2	Interconnections . . . . .	65
6.2	Circuit simulations . . . . .	66
6.2.1	The method . . . . .	66
6.2.2	Effect of connection resistance . . . . .	67
6.2.3	Bilayer-related defects . . . . .	67
6.2.4	Leakage of the insulation . . . . .	69
6.3	Measurements on the arrays . . . . .	71
6.3.1	Connection resistance and leakage . . . . .	71
6.3.2	QHE measurements . . . . .	72
	<b>Summary and outlook</b>	<b>77</b>
<b>A</b>	<b>Arbitrary multiple-parallel connection</b>	<b>79</b>
<b>B</b>	<b>Fabrication recipes</b>	<b>81</b>
B.1	Lift-off deposition . . . . .	81
B.2	Patterning graphene . . . . .	82
B.3	Suggested sequence for fabricating the quantum Hall array . . . . .	82
	<b>Bibliography</b>	<b>85</b>
	<b>Appended papers</b>	<b>101</b>

# List of Figures

1.1	Direct and reciprocal lattice of monolayer graphene . . . . .	6
1.2	Energy dispersion in monolayer graphene . . . . .	6
1.3	Crystal lattice and energy dispersion of bilayer graphene . . . . .	8
1.4	Gate-dependent electric transport in monolayer graphene . . . . .	11
1.5	An example of QHE measurement . . . . .	13
1.6	Equipotential lines in a quantum Hall system . . . . .	15
1.7	Landau levels in a quantum Hall system . . . . .	15
1.8	Aharonov-Bohm geometry for a quantum Hall system . . . . .	17
1.9	QHE breakdown in a GaAs device . . . . .	20
1.10	Charge transfer between epitaxial graphene and the substrate . . . . .	24
1.11	Charge transfer to the substrate in the QHE regime . . . . .	26
1.12	Breakdown current density in GaAs and epitaxial graphene . . . . .	27
1.13	Equipotential lines in a quantum Hall device . . . . .	28
1.14	Parallel connection of quantum Hall bars . . . . .	30
1.15	Potential distribution in bordering QHE domains . . . . .	32
1.16	Fresnel reflection with a graphene layer at the border . . . . .	34
2.1	Patterning graphene by plasma etching . . . . .	38
2.2	Lift-off deposition on graphene . . . . .	38
2.3	An example of a pattern for two interconnected Hall bars . . . . .	39
2.4	Differential interference contrast . . . . .	41
3.1	Tuning the carrier density in epitaxial graphene by corona discharge . . . . .	47
4.1	A bilayer patch inside a monolayer Hall bar . . . . .	50
4.2	Measurement on a Hall bar with a metallic bilayer patch cutting across . . . . .	51
4.3	Insulating behavior of the bilayer patches . . . . .	53
4.4	An n-p-n QHE junction created by a local gate . . . . .	54
4.5	A Hall bar with bilayer patch in QHE regime . . . . .	55

5.1	Bilayer patches imaged by optical microscopy . . . . .	59
5.2	Phase gradients in optical images of epitaxial graphene . . . . .	60
5.3	Observation of steps on SiC substrate by optical microscopy . . . . .	61
6.1	Design of the Hall bars, adapted to the bilayer patches . . . . .	65
6.2	Design of the interconnects in the array . . . . .	66
6.3	Bilayer-related defects in graphene Hall bars . . . . .	69
6.4	Modeling insulation leakage in a quantum Hall array . . . . .	70
6.5	Measurement of the insulation leakage in the array . . . . .	71
6.6	QHE measurements on the arrays . . . . .	72
6.7	Comparison of QHE in an array and single Hall bars . . . . .	74
A.1	Arbitrary multiple-parallel connection of any number of Hall bars . . . . .	79

# Preface

The main purpose of this thesis is answering the question: how to make quantum Hall devices on epitaxial graphene? In addition to this, the background chapter aims to contain everything one may possibly need to know about electronic and optical properties of graphene in general and epitaxial graphene in particular. Furthermore, it provides an extensive theoretical description of the quantum Hall effect, for readers interested in a deeper understanding of the underlying physics.

Experimental findings presented in chapters 3 to 5 emphasize the problems that epitaxial graphene presents as a material for quantum Hall devices, and chapter 6 describes the steps that we undertook to address various issues. The appendix contains information deemed too technical for the main text, yet still important. All in all, this thesis should be helpful to anyone willing to make some more Hall bars.

An electronic version of this thesis, which includes  $\LaTeX$  source and other extra materials as attachments, is available from Chalmers MC2 E-Nailed Doctoral Theses and from the Chalmers Publication Library.



# Introduction

The quantum Hall effect is a very important phenomenon in solid state physics. It provides a means to produce devices with electrical resistance almost exactly equal to a combination of fundamental constants:  $h/2e^2$ , where  $h$  is the Planck's constant and  $e$  the elementary charge. "Almost exactly" means three things: first, the quantum Hall resistance is reproducible within the relative precision of  $\sim 5 \cdot 10^{-11}$  [1, 2] – and for all we know, the actual reproducibility can be even better, it's just that the measurements could not be performed more accurately than this. Second, this resistance matches with the known value of  $h/2e^2$  with  $10^{-7}$  precision [3], limited by how well that comparison can be performed. Finally, it is expected that the relative deviation from  $h/2e^2$  under the correct conditions is no more than  $10^{-20}$  [4], which justifies dropping the word "almost" and simply saying that this value of quantized Hall resistance is exact, as far as we know.

Such remarkable reproducibility and the fundamental nature of the quantum Hall effect means that it can be used for defining electrical units, in much the same way as atomic spectra and the speed of light are used for the definitions of the second and the meter. In the current version of the *Système International* electrical units are defined by fixing the values of the magnetic constant  $\mu_0$  and the vacuum permittivity  $\epsilon_0$ . In particular, the ohm is defined as  $1/119.9169832\pi$  of the free space impedance  $\mu_0 c$ . Realisation of the electrical units through macroscopic electrodynamics requires electromechanical measurements involving moving plate capacitors [5], and the accuracy of these measurements is only approaching  $10^{-8}$ . Meanwhile, electrical-only realisation of the ohm through the quantum Hall effect has the accuracy of  $3 \cdot 10^{-10}$ , limited by the precision of the known value of the fine structure constant  $\alpha = \mu_0 c / (2h/e^2)$ . However, electrical measurements on quantum Hall devices per se have an accuracy better than  $1 \cdot 10^{-10}$ . This has led to a new unit of resistance: a "quantum ohm" which is different from the SI ohm, and is defined as  $1/12906.4037217$  of the quantum Hall resistance [6]. Furthermore, alternative versions of the ampere, coulomb, henry, farad and watt have been

introduced as derivative units of this new ohm<sup>1</sup>. It is likely that these alternative units will become the real ones in the new revision of SI.

Observation of the quantum Hall effect requires a high quality quasi-two-dimensional conducting material, a low temperature, and a strong magnetic field. The current state-of-the-art quantum Hall resistance standards are based on gallium arsenide, and for this material “low temperature” means 1 kelvin and “strong field” is 10 tesla. The discovery of graphene has opened a new page in resistance metrology because the unique electronic properties of graphene relax these requirements to 4 kelvin and 5 tesla [7, 8], making it easier and cheaper to perform the measurements. Out of all different ways to produce graphene, epitaxial graphene on silicon carbide has so far been the most successful candidate for fabricating the next generation of quantum Hall standards. Apart from being, unlike most other brands of graphene, large-area and single-crystal, it brings an additional advantage: quantum Hall devices made of epitaxial graphene can sustain higher current densities before they get overheated so much that the quantum Hall state breaks down, as compared to their gallium arsenide counterparts [9]. This is important for metrology because a higher measurement current translates into a better precision. It has already been demonstrated that graphene can provide the same  $10^{-10}$  accuracy as gallium arsenide does [10], and an even higher accuracy can be expected in the future. To summarize, quantum Hall devices made of graphene are already, in principle, better than the current state of the art, thus making them the new state of the art is a matter of developing the technology, and also our goal.

To date, several groups have reported high-precision measurements of the quantum Hall resistance in graphene produced on silicon carbide by either thermal decomposition of the substrate or chemical vapor deposition [10–12]. Thus, graphene is already on a way to becoming a well-established technology for quantum Hall devices. However, quantum Hall resistance metrology does not end at single devices with the resistance of  $h/2e^2 \approx 13 \text{ k}\Omega$ . High-precision material resistors ranging from milliohms to gigaohms need to be created by calibrating against a quantum Hall standard. Therefore, it would be advantageous to have a set of quantum standards with a range of values as wide as possible. This can be achieved by connecting a number of Hall bars in series or in parallel, but such task imposes much stricter requirements on the technology as it involves fabricating tens, possibly hundreds of individual devices which must all work at the same time. One of our objectives in this work was exploring whether epitaxial graphene can provide that kind of reliability.

---

<sup>1</sup>A “quantum volt” is defined independently through the Josephson effect.

This thesis is organized as follows. Chapter 1 describes electronic properties of graphene, including those specific to epitaxial graphene on silicon carbide, and their impact on the quantum Hall effect in this material. The microscopic theory of the quantum Hall effect and the theory of quantum Hall circuits are also presented. Chapter 2 is devoted to techniques used for device fabrication, measurement and material characterization. In chapter 3 we address the issue of carrier density control: for the measurements of the quantum Hall effect to be possible, the carrier density in the material must assume a certain value, and in epitaxial graphene the doping can often be too high. We discuss the techniques that we use to tune the carrier density and show that we can reliably reach the desired parameters regardless of the initial doping. Chapter 4 describes how certain structural features of epitaxial graphene, the bilayer patches, can destroy the quantum Hall effect. A practical way to deal with the problem of the patches is shown in chapter 5: we demonstrate that it is possible to completely characterize the morphology of the samples in a quick and non-invasive way by optical microscopy. Using our knowledge of the material, we have designed and fabricated quantum Hall arrays consisting of up to a hundred individual Hall bars, and the measurements on these devices are presented in chapter 6. Our results suggest that not only individual high-quality quantum Hall devices, but also a huge number of them with close to 100% yield, is possible on epitaxial graphene.



# Chapter 1

## Background and theory

### 1.1 Graphene: basic electronic structure

Graphene, a single atomic layer of graphite or a stack of few such layers, was for the first time produced in 2004 from bulk graphite in a Noble prize-winning discovery [13], as well as by thermal decomposition of silicon carbide in an independent study published a few months later [14]. However, electronic properties of graphene, including the monolayer, have been studied theoretically since 1947 [15] for the purpose of understanding properties of graphite. It has been predicted, and much later verified experimentally, that an elementary substance with the crystal lattice of monolayer graphene, of which graphene is the only reasonably technologically mature example<sup>1</sup>, has an unusual property of zero charge carrier effective mass. This is what causes graphene-based quantum Hall devices to operate at higher temperatures and lower fields. In this section, basic electronic properties of monolayer and bilayer graphene will be reviewed in detail.

A graphene layer consists of carbon atoms in a honeycomb lattice (Figure 1.1a) which has two atoms A and B in the unit cell of a triangular lattice. The reciprocal lattice (Figure 1.1b) is also triangular, and the first Brillouin zone is a hexagon. Each carbon atom has 4 valence electrons, 3 out of which are involved in covalent  $\sigma$ -bonds with the nearest neighbouring atoms. The remaining electrons, one per atom, can be thought of as forming a giant aromatic  $\pi$ -bond spanning the whole crystal. It's these  $\pi$ -electrons that form valence and conduction bands in graphene.

The energy dispersion as calculated from the tight-binding model for a

---

<sup>1</sup>Silicon and germanium based analogs of graphene, called silicene and germanene, are known to exist, but are much less studied due to their instability in air.

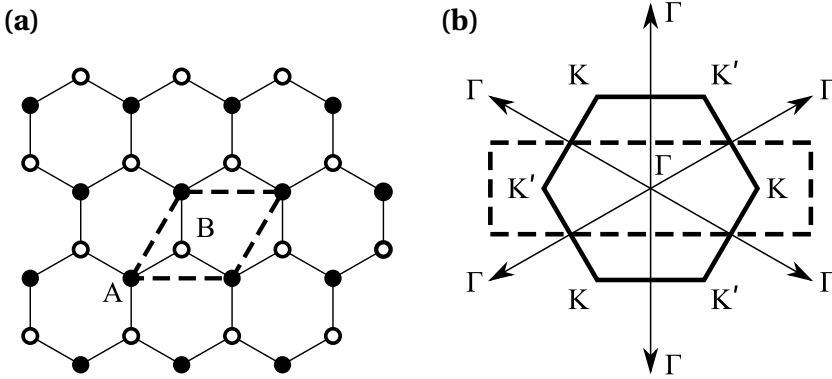


Figure 1.1: (a) Crystal lattice of the graphene layer, dashed lines highlight a unit cell. (b) Reciprocal lattice, showing the first Brillouin zone (hexagon) and a rectangular shaped unit cell used for plotting  $E(\vec{k})$  in Figure 1.2 (dashed line). Points equivalent to  $\vec{k} = 0$  are labeled  $\Gamma$ ;  $K$  and  $K'$  are the corners of the first Brillouin zone, which are also minima (maxima) of the conduction (valence) bands.

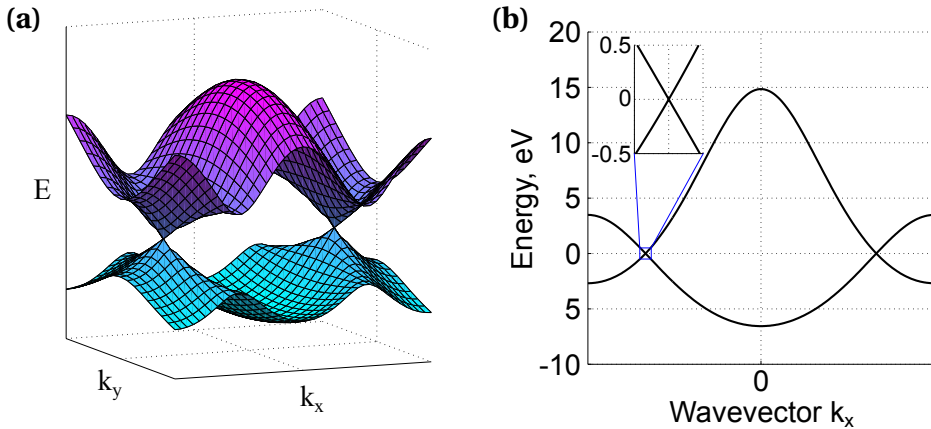


Figure 1.2: (a) Two-band energy dispersion for electrons in graphene calculated within one unit cell of the reciprocal lattice. (b) A cross-section through the Dirac points.

single layer is shown in Figure 1.2. There are two energy bands arising from the A and B sublattices, which touch each other at two points. These two points are the two non-equivalent corners of the first Brillouin zone, called K- and K'-points and also referred to as Dirac points. The total number of states in each band is twice the number of atoms in a sublattice (twice due to spin degeneracy), which is equal to the total number of  $\pi$ -electrons. Thus graphene is a semimetal with the Fermi level at an energy where the two bands touch each other; the two Dirac points form two valleys of the Fermi surface.

In the vicinity of both Dirac points, energy dispersion has the form [16]

$$\mathcal{E}(\vec{K} + \vec{q}) \approx \pm \hbar v_F |\vec{q}|$$

where  $\vec{K}$  is the wavevector of a K- or K'-point, and  $v_F \approx 1 \cdot 10^6$  m/s is the Fermi velocity. The two-band Hamiltonian in this region is

$$\hat{H} = v_F \begin{pmatrix} 0 & \pm \hat{p}_x - i \hat{p}_y \\ \pm \hat{p}_x + i \hat{p}_y & 0 \end{pmatrix} \quad (1.1)$$

with plus sign for the K-point and minus sign for K'. This is similar to the Hamiltonian, and the corresponding energy dispersion, of massless particles described by the two-dimensional relativistic Dirac equation, with the speed of light replaced by  $v_F$ .

The Hamiltonians for the two Dirac points differ by swapping the A and B sublattices and changing the overall sign. The two sublattices only differ by a  $60^\circ$  rotation and are usually physically equivalent, so swapping them does not matter. The overall sign does not matter either because the corresponding Schrödinger equation has similar solutions with positive and negative energies, an analogue of particles and antiparticles from the relativistic theory. Thus the two Hamiltonians are often equivalent, and so it is common to speak of a single Dirac point rather than two, with a double degeneracy, a so called valley degeneracy, for each electron state (in addition to the usual spin degeneracy).

The crystal lattice of bilayer graphene consists of two layers stacked on top of each other as shown in Figure 1.3a. There are four atoms A1, B1, A2 and B2 in a unit cell, and atoms B2 and A1 are on top of each other (this is called A-B stacking). The band structure (Figure 1.3b) reminds of that of the monolayer, except there are four bands instead of two. However, two of these bands are separated by some 0.4 eV gap and thus are in most cases not of interest for the electronic properties. The other two bands, corresponding to the B1 and A2 sublattices, touch each other at the same two points  $K$  and  $K'$  as they do

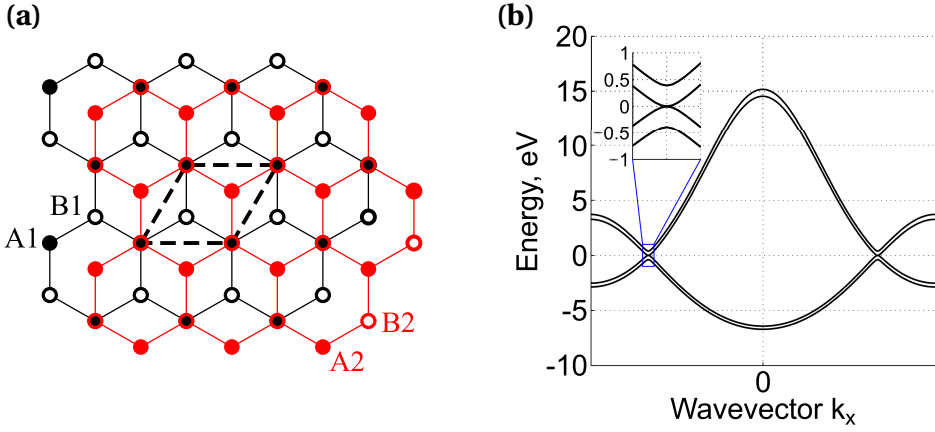


Figure 1.3: a) Crystal lattice of bilayer graphene, black and blue are the two layers and the dashed lines highlight a unit cell. b) Calculated four-band energy dispersion in bilayer graphene (a cross-section through the Dirac points).

in the monolayer, and the simplified two-band Hamiltonian in the vicinity of these points is

$$\hat{H} = -\frac{1}{2m} \begin{pmatrix} 0 & (\pm\hat{p}_x - i\hat{p}_y)^2 \\ (\pm\hat{p}_x + i\hat{p}_y)^2 & 0 \end{pmatrix} \quad (1.2)$$

where  $m \approx 0.033m_e$  is the effective mass. The corresponding energy dispersion is quadratic:  $\mathcal{E}(\vec{p}) = \pm p^2/2m$ , which is somewhat similar to ordinary semiconductors, but this doesn't imply similarity of electronic properties because of the zero band gap and a substantially different Hamiltonian. The B1 and A2 sublattices are usually equivalent, so the electron states in bilayer graphene feature the same additional valley degeneracy as they do in the monolayer.

The intrinsic Hamiltonian of bilayer graphene is modified when an external perpendicular electric field is applied [17, 18]. The reason is that the external field is not completely screened in between the layers, giving rise to an internal electric field  $E_i$  which depends on the fields above the top layer and below the bottom layer, as well as on the carrier density. This internal field creates a potential difference between the layers, and the Hamiltonian (1.2) is then transformed into

$$\hat{H}(E_i) = -\frac{1}{2m} \begin{pmatrix} -eE_i c/2 & (\pm\hat{p}_x - i\hat{p}_y)^2 \\ (\pm\hat{p}_x + i\hat{p}_y)^2 & eE_i c/2 \end{pmatrix} \quad (1.3)$$

where  $c \approx 3.3 \text{ \AA}$  is the interlayer distance. The energy dispersion with this Hamiltonian is  $\mathcal{E}(p) = \pm \sqrt{(p^2/2m)^2 + (eE_i c/2)^2}$ , which means that a band gap with the magnitude  $U = |eE_i c|$  is created. This, however, won't make bilayer graphene exactly similar to ordinary semiconductors because the energy dispersion just above the gap is  $\mathcal{E}(p) \approx U/2 + p^4/4m^2U$  – fourth-power instead of quadratic.

## 1.2 Electron transport in graphene

Charge carrier density and mobility are important parameters for most conductive materials, and knowing them is one of the essential goals of material characterization. In graphene, the carrier density can also easily be changed by the field effect or through doping by adsorption of various molecules. In fact, graphene devices often feature field-effect-transistor-type behavior: the carrier density is tuned until it assumes the desired value.

In a semiconductor with only one type of charge carriers present, the carrier density  $n$ , along with the mobility  $\mu$ , can be directly extracted from measurements of the resistivity tensor in magnetic fields. For a two-dimensional material in a perpendicular magnetic field  $B_z$ , the resistivity has the form

$$\rho = \begin{pmatrix} \rho_{xx} & \rho_{xy} \\ -\rho_{xy} & \rho_{xx} \end{pmatrix}$$

with the components equal to

$$\rho_{xx} = \frac{1}{e|n|\mu}, \quad \rho_{xy} = \frac{B_z}{en} \quad (1.4)$$

In a right-hand coordinate system and with the sign convention introduced above,  $n > 0$  for negatively charged carriers (electrons) and  $n < 0$  for holes. The material parameters can thus be calculated according to

$$n = \left( e \frac{\rho_{xy}}{B_z} \right)^{-1}, \quad \mu = \frac{|\rho_{xy}/B_z|}{\rho_{xx}} \quad (1.5)$$

In graphene, zero intrinsic band gap makes the situation more complicated. Carrier density dependence of the resistivity  $\rho_{xx}$  and the Hall coefficient  $\rho_{xy}/B_z$  in graphene should, in general, be expressed in terms of ambipolar transport:

$$\rho_{xx}(n', T) = \frac{1}{e(\mu_n(n', T)n(n', T) + \mu_p(n', T)p(n', T))} \quad (1.6)$$

$$\frac{\rho_{xy}}{B_z}(n', T) = \frac{\mu_n^2(n', T)n(n', T) - \mu_p^2(n', T)p(n', T)}{e(\mu_n(n', T)n(n', T) + \mu_p(n', T)p(n', T))^2} \quad (1.7)$$

where the electron and hole mobilities  $\mu_n$  and  $\mu_p$  and the densities of electrons and holes  $n$  and  $p$  are all functions of temperature  $T$  and the relative charge density  $n' = n - p$  which is the parameter controlled by a gate or doping.

The behavior of  $n(n', T)$  is qualitatively depicted in Figure 1.4a. The density of holes behaves the same way: due to the symmetry between electron and hole bands,  $p(n', T) = n(-n', T)$ . At higher temperatures, an increasingly large number of electrons exist as minority carriers in the region  $n' < 0$  due to thermal excitations. At low temperatures, minority carriers are still present due to stochastic spatial variations of the chemical potential caused by long-range disorder that leads to the formation of electron-hole puddles at low carrier densities [20–22]. Quantitatively, this can be written as [23]

$$n(\mathcal{E}_F, T) = \int_{-\infty}^{\infty} P(\mathcal{E}') d\mathcal{E}' \int_0^{\infty} D(\mathcal{E}) f(\mathcal{E}, \mu(\mathcal{E}_F + \mathcal{E}', T), T) d\mathcal{E} \quad (1.8)$$

where  $P(\mathcal{E}')$  is the distribution of the variations of the chemical potential,  $D(\mathcal{E})$  is the density of states ( $D(\mathcal{E}) = 2|\mathcal{E}|/\pi(\hbar v_F)^2$  for monolayer graphene),  $f(\mathcal{E}, \mu, T)$  is the Fermi-Dirac distribution, and  $\mu(\mathcal{E}_F, T)$  is the temperature-dependent chemical potential given by charge conservation

$$\begin{aligned} \int_0^{\infty} D(\mathcal{E}) f(\mathcal{E}, \mu(\mathcal{E}_F, T), T) d\mathcal{E} - \int_{-\infty}^0 D(\mathcal{E}) (1 - f(\mathcal{E}, \mu(\mathcal{E}_F, T), T)) d\mathcal{E} = \\ = \text{sgn}(\mathcal{E}_F) \cdot \int_0^{|\mathcal{E}_F|} D(\mathcal{E}) d\mathcal{E} \end{aligned}$$

In particular, a special case of (1.8) for  $P(\mathcal{E}) = \frac{1}{2}(\delta(\mathcal{E} - \Delta) + \delta(\mathcal{E} + \Delta))$  and  $k_B T \ll \Delta$  has been considered in [19, 24], yielding

$$\begin{aligned} n(\mathcal{E}_F, T) = \int_0^{\infty} D(\mathcal{E}) f(\mathcal{E}, \mu(\mathcal{E}_F, T_{eq}(T)), T_{eq}(T)) d\mathcal{E} \\ T_{eq}(T) = \sqrt{T^2 + \frac{3}{\pi^2 k_B^2} \Delta^2} \end{aligned}$$

The mobilities  $\mu_n$  and  $\mu_p$  in monolayer graphene typically increase with decreasing temperature due to diminishing thermal vibrations, and decrease

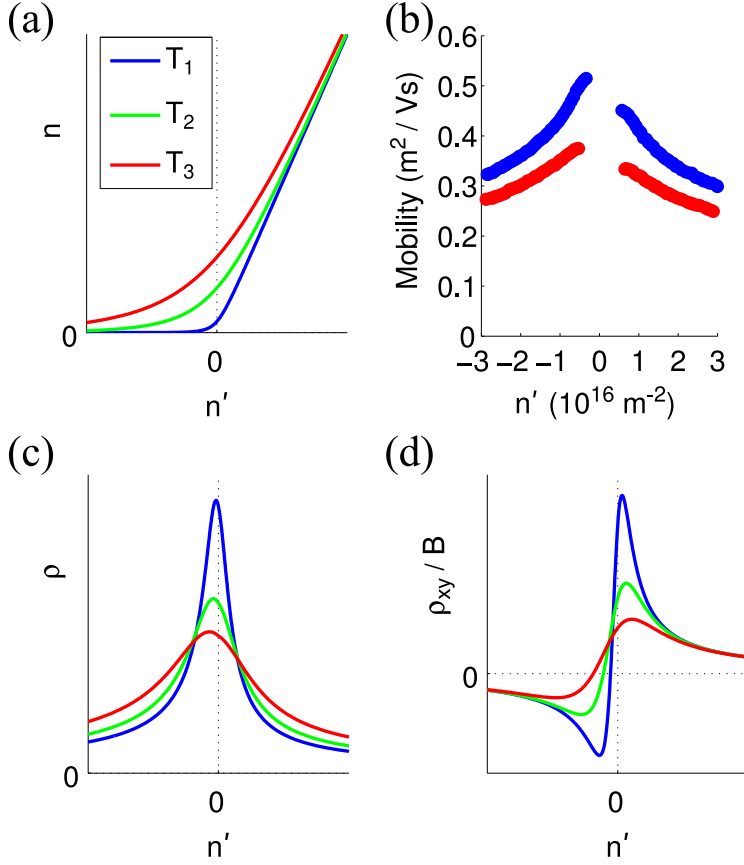


Figure 1.4: (a) Gate dependence of the electron density in graphene for different temperatures  $T_1 < T_2 < T_3$ , calculated according to equation 1.8 with Gaussian  $P(\mathcal{E})$ . (b) Temperature and gate dependence of mobility in a monolayer graphene sample (adapted from [19]). (c), (d) Calculated temperature and gate dependence of resistivity and Hall coefficient (for the case  $\mu_n > \mu_p$ ). The temperatures (and colors) are the same as in (a).

with increasing  $|n'|$  weaker than  $1/|n'|$ , as shown in Figure 1.4b. Electron and hole mobilities can, in general, be different. Equations (1.6) and (1.7) with this mobility dependence, and  $n(n', T)$  and  $p(n', T)$  described above, lead to temperature and gate dependence of  $\rho$  and  $\rho_{xy}/B$  similar to those shown in Figure 1.4c,d. The gate dependence is asymmetric when  $\mu_n \neq \mu_p$  ( $\mu_n > \mu_p$  in Figure 1.4c,d).

At high carrier densities, there are no minority carriers, so the carrier density and mobility can be determined from resistance and Hall measurements according to the usual formulas (1.5). However, a different approach is required in order to do this in the region of ambipolar transport at low carrier densities. In particular, it is, strictly speaking, impossible to extract the carrier density from a single Hall measurement: according to Figure 1.4d, for almost any possible value of the Hall coefficient, there are two values of the carrier density. Additional information, such as longitudinal resistivity or a gate sweep to determine the sign of  $d\rho_{xy}/dn'$ , can be used to resolve the ambiguity.

As a final note, the above model gives infinite resistivity for a uniform, charge-neutral graphene sheet at absolute zero ( $P(\mathcal{E}) = \delta(\mathcal{E})$ ,  $n' = 0$ ,  $T = 0$ ) due to vanishing density of states at the Fermi level. However, what it actually means is that the description of electron states using the density of states is not applicable, and a more detailed picture of quantum transport is needed instead. Theoretical results on this are somewhat controversial [25], but most theories predict a maximum resistivity of  $\rho_{max} = \pi h/4e^2$  for an ideal graphene sheet [26–30], something that could not be confirmed by experiments [31] probably due to the lack of ideal graphene sheets in the real world.

### 1.3 The quantum Hall effect

The quantum Hall effect (QHE) has received a lot of attention immediately after its discovery in 1980 [32]. It is sometimes referred to as an example of a macroscopic quantum phenomenon, meaning that it reveals quantum features of an (in principle) arbitrarily large system, which require not just quantum statistics but the fundamental concepts of Hamiltonian operators and wave functions for any qualitative explanation.

The QHE is observed during magnetotransport measurements (Figure 1.5a, inset) in quasi-two-dimensional conductors at low temperatures in strong perpendicular magnetic fields. Under normal conditions (for example, in small fields or in thick samples) the transverse or Hall resistance, which is defined as  $R_{xy} = V_{xy}/I$  and approximately equal to the off-diagonal component of the

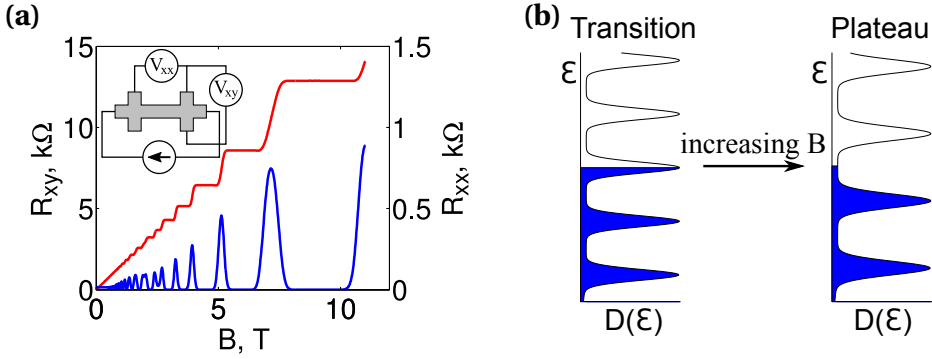


Figure 1.5: (a) An example of a QHE measurement in a GaAs/AlGaAs heterostructure (adapted from [33]). Inset: the measurement setup. (b) Evolution of the density of states with the magnetic field. Fermi level in the middle of a Landau level (left) corresponds to a transition between two QHE plateaus. At a higher field, the Fermi level will be between two Landau levels (right), which corresponds to the QHE regime.

resistivity tensor, increases linearly with magnetic field according to equation 1.4:

$$R_{xy}(B) \approx \rho_{xy} = \frac{B}{en}$$

When the conducting layer is so thin that motion of the charge carriers can be treated as purely two-dimensional (that is, its thickness is on the order of the Fermi wavelength of the charge carriers or less<sup>2</sup>), then at low temperatures and in certain regions of magnetic field the sample can go into the so called quantum Hall regime characterized by unusual transport properties (Figure 1.5a). Namely, the transverse resistance depends on neither the magnetic field, current nor the sample geometry and is nearly exactly equal to

$$R_{xy} = R_H = \frac{h}{\nu e^2} \quad (1.9)$$

where  $\nu$  is a small<sup>3</sup> integer, and the longitudinal resistance  $R_{xx} = V_{xx}/I$  essentially vanishes. The only known corrections to this are the ones due to finite

<sup>2</sup>Which is equivalent to the distance between the energy levels arising from confinement in the 3rd dimension being on the order of the Fermi level or above, meaning that only one or a few minibands are being filled.

<sup>3</sup>The maximum filling factor can be as high as a few tens, although metrological precision has only been reached for  $\nu \leq 4$ .

temperature and finite current (which are below  $10^{-10}$  in a typical experiment but can, in principle, be arbitrarily small), and the extremely small (on the level of  $10^{-20}$ ) correction predicted by quantum field theory [4].

To some extent<sup>4</sup>, a material in the quantum Hall regime can be described by two-dimensional resistivity tensor of a form

$$\rho = \begin{pmatrix} 0 & R_H \\ -R_H & 0 \end{pmatrix} \quad (1.10)$$

Probably the most remarkable feature of the QHE is that the measured transverse resistance is equal to the quantized value (1.9) with a relative accuracy better than  $10^{-7}$  in real samples with a considerable amount of disorder present. There are other systems where resistance quantization is observed, such as point contacts or ballistic nanowires, but the quantization precision there is not nearly as good. This precision is what makes the QHE relevant for metrology.

The quantum Hall effect is a consequence of Landau quantization [37, 38] in strong magnetic fields. When an ideal 2D electron gas (without disorder) is subject to a uniform perpendicular magnetic field  $B$ , the (originally continuous) energy spectrum of the electrons is transformed into a discrete set of massively degenerate energy levels, called Landau levels (LL). Disorder will lift the degeneracy of the LL's, causing them to broaden from delta-function-like features in the density of states into peaks of finite width. However, as long as the disorder is not too strong, these peaks will remain well separated.

The number of states per unit area in each LL is approximately  $n_L(B) = eB/h$  which is proportional to  $B$ . Hence as the magnetic field is increased while the carrier density stays constant, the LL's will gradually move up with respect to the Fermi level as every single one can accommodate more and more carriers (Figure 1.5b). The QHE regime occurs when the Fermi level is in between the peaks in the density of states, if the temperature is low enough that the peak above the Fermi level is empty: that is, the thermal energy  $k_B T$  is much less than half the distance between the LL's. In the next section, the above arguments will be given a stricter interpretation.

### 1.3.1 The theory of quantum Hall effect

Disregarding the spin, the energies of pure Landau levels can be found from the Schrödinger equation for a 2D gas of free non-interacting electrons in a uniform perpendicular magnetic field:

---

<sup>4</sup>Complicated, magnetic-field-dependent distributions of potential and current density inside a quantum Hall domain [34–36] cannot be explained by a simple resistivity tensor.

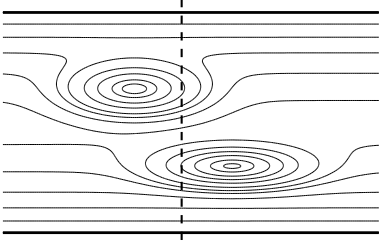


Figure 1.6: Equipotential lines in a quantum Hall system

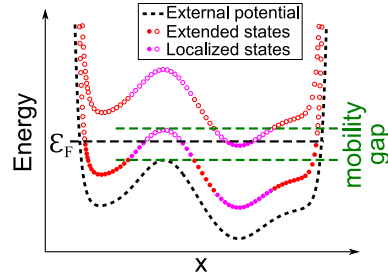


Figure 1.7: Landau levels in a quantum Hall system (a cross-section of Figure 1.6)

$$[\hat{H}_0(-i\hbar\vec{\nabla} + e\vec{A})]\psi = \mathcal{E}\psi \quad (1.11)$$

Here,  $\hat{H}_0(\vec{p})$  is the momentum-dependent Hamiltonian, and  $\vec{A}(x, y)$  is the vector potential of the uniform magnetic field. For example, in ordinary semiconductors  $\hat{H}_0 = \vec{p}^2/2m$ , and the LL's are then  $\mathcal{E}_n = \hbar \frac{eB}{m} (n + \frac{1}{2})$ .

Now, consider the same 2DEG but with an additional electrostatic potential of the form

$$V(x, y) = V_C(x) + V_D(x, y)$$

where  $V_C(x)$  is a confining potential which is close to zero in the range  $|x| < L_x/2$  and goes to infinity when  $|x| > L_x/2$ , therefore confining the 2DEG to a stripe of the width  $L_x$ , and  $V_D(x, y)$  is a stochastic disorder potential. The single-electron Schrödinger equation will then read

$$[\hat{H}_0(-i\hbar\vec{\nabla} + e\vec{A})]\psi + V(x, y)\psi = \mathcal{E}\psi \quad (1.12)$$

For a slowly varying disorder potential  $V_D$ , solutions to (1.12) can be qualitatively described as follows [39–41]. The wavefunction of each eigenstate will be localized within the distance on the order of  $l_B = \sqrt{\hbar/eB}$  from some equipotential line of  $V(x, y)$ , and the eigenenergies will approximately follow the external potential:

$$\mathcal{E}_{p,n} \approx V_p + \mathcal{E}_n \quad (1.13)$$

where  $V_p$  is the value of  $V(x, y)$  on the equipotential line of  $p$ -th state, and  $\mathcal{E}_n$  are the original Landau levels. The first term in (1.13) causes disorder broadening of the LL's in a real system.

There will be two types of equipotential lines, as can be seen in Figure 1.6. Some will go all the way along the stripe (there will always be such lines at least along the edges where  $V(x, y)$  increases sharply), while others will form closed loops around minima and maxima of  $V_D$ . Eigenstates associated with open equipotential lines are referred to as extended states, and those corresponding to closed equipotential lines are called localized states. Only the extended states can carry electric current.

It is reasonable to assume that  $|V_D(x, y)|$  is large only within a set of isolated areas, since it can be expected to be close to zero on the average. In this case, all those states in the bulk of the stripe which have energy considerably different from that of an unperturbed LL (without disorder) will be localized. Extended states in the bulk will have energy close to an unperturbed LL, differing by at most some  $\Delta\mathcal{E}_{max}$  which can be much less than the maximum value of  $|V_D|$ . There will still be extended states at any energy at the edges. If now the magnetic field is strong enough that  $\mathcal{E}_{n+1} - \mathcal{E}_n > 2\Delta\mathcal{E}_{max}$ , the extended states of different LL's, except at the edges, will be separated by an energy gap which is called the mobility gap. Localized states of different LL's might not be separated by a gap, but this does not matter for the QHE. The quantum Hall regime occurs when the Fermi level is inside the mobility gap, so that the only extended states at the Fermi level are on the edges. All bulk extended states below the Fermi level must be filled, and all extended states belonging to "non-filled" LL's must be empty, which is why the QHE breaks down at high temperatures. Strictly speaking, there is a correction to the quantized Hall resistance at any finite temperature, but it quickly vanishes in the  $T \rightarrow 0$  limit.

In the picture of non-interacting electrons, resistance quantization can, to some extent, be derived by considering Aharonov-Bohm type of geometry, as originally suggested by Laughlin [42] and Halperin [43]. A stripe of 2DEG forms a ring (or a cylinder, but we assume ring geometry here) in a perpendicular magnetic field, with a confining potential going to infinity at the inner and outer radii of the ring, and a disorder potential inside the ring. An additional magnetic flux  $\Phi$  is piercing the ring but does not enter the area where the 2DEG is confined (Figure 1.8a). An external voltage  $V$  is applied between the inner and outer radii of the ring, which gives rise to a current circulating the ring.

The same analysis of eigenstates and eigenenergies as the one for a stripe applies here. Again, there will be extended states which are defined as ones that encircle the opening in the ring, and localized states which don't encircle it. Only filled extended states contribute to the current.

Similar to the Aharonov-Bohm effect, the additional flux  $\Phi$  will affect the

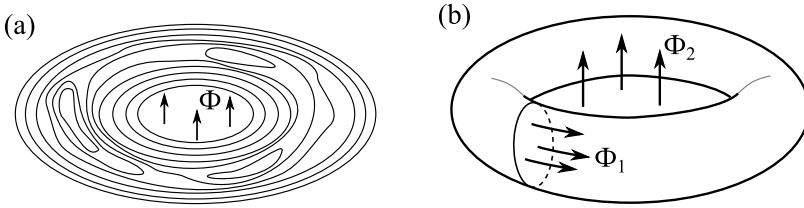


Figure 1.8: (a) 2DEG in Aharonov-Bohm type of geometry as considered in [43]; (b) the “double Aharonov-Bohm geometry” used to link quantized Hall conductance to a topological invariant.

eigenstates of the system because even though the magnetic field that creates it does not enter the 2DEG, its vector potential does. And the effect of the flux on the energy  $\mathcal{E}_\alpha$  of an eigenstate  $\psi_\alpha$  is related to the circular current carried by that state [44]:

$$I_\alpha = \frac{\partial \mathcal{E}_\alpha}{\partial \Phi}$$

The localized states are not affected by the flux since they don't encircle it, and they don't carry any current either. The total current is therefore

$$I = \sum_\alpha \frac{\partial \mathcal{E}_\alpha}{\partial \Phi} = \frac{\partial}{\partial \Phi} \sum_\alpha \mathcal{E}_\alpha = \frac{\partial U}{\partial \Phi} \quad (1.14)$$

where the sum is taken over all occupied states.

As the flux  $\Phi$  is increased, the contours along which the extended states go will move towards the neighbouring extended state, all in the same direction (say, towards the outer radius), their energies changing accordingly. However, a change of flux by  $\Phi_0 = h/e$  does not affect the states since it is equivalent to a gauge transformation [42], therefore mapping the entire set of eigenstates and eigenenergies onto itself by mapping each extended state onto the neighbouring one. At this point, an assumption is made that occupations of the states will not change during adiabatic change of the flux. Then due to the presence of the mobility gap, the net effect of the change of flux by  $\Phi_0$  will be that the inner-most extended state in each LL (which is an edge state at the inner radius) becomes empty while a state next to the outer-most extended state (which, similarly, is an outer edge state) becomes occupied. The change in energy will be  $\Delta U_{LL} = \Delta\mu$  per each filled LL, where  $\Delta\mu = eV$  is the chemical potential difference between the edges. The total change in energy is then  $\Delta U = N \cdot \Delta U_{LL} = N \cdot eV$ , where  $N$  is the amount of filled LLs.

The current does not depend on the flux  $\Phi$  as the latter adiabatically increases by one quantum<sup>5</sup>. Therefore, the derivative in (1.14) can be replaced by a ratio of finite changes yielding

$$I = \frac{\Delta U}{\Phi_0} = N \frac{e^2}{h} V$$

and (1.9) with  $v = N$  immediately follows. The mobility gap appears to decrease with the increase of the Landau level index, which is why very high filling factors cannot be observed. If the Landau levels had spin degeneracy then only even filling factors would be seen; Zeeman splitting allows observation of odd filling factors in semiconductors. The current density will be roughly proportional to the gradient of the external potential: it can thus be particularly large at the edges, but also non-zero in the bulk.

The absence of electron-electron interactions and the unproven assumption that the occupations of energy eigenstates are not affected by the flux are two serious shortcomings of the Laughlin's method. Niu, Thouless and Wu [45] have dealt with both of these problems by considering a quantum Hall domain with the shape of a torus<sup>6</sup> pierced by two independent fluxes (Figure 1.8b), at the expense of ignoring the edges. In this approach, electron-electron interactions are explicitly taken into account by using a multiparticle Hamiltonian instead of a single-particle one. Zero-temperature version of the Kubo linear response formula for the electrical conductivity [46, 47] can be used at finite temperatures because only excitations above the mobility gap can affect the conductivity. For the QHE problem this formula gives [45, 48]

$$\sigma_{xy} = \frac{ie^2}{\hbar} \left( \frac{\Phi_0}{2\pi} \right)^2 \left( \left\langle \frac{\partial \psi_0}{\partial \Phi_1} \middle| \frac{\partial \psi_0}{\partial \Phi_2} \right\rangle - \left\langle \frac{\partial \psi_0}{\partial \Phi_2} \middle| \frac{\partial \psi_0}{\partial \Phi_1} \right\rangle \right)$$

where  $\psi_0$  is the multiparticle ground state. Once again, the conductivity does not depend on the fluxes [45, 49], so this expression can be replaced by its average value

$$\sigma_{xy} = \frac{ie^2}{2\pi\hbar} \int_0^{\Phi_0} \int_0^{\Phi_0} d\Phi_1 d\Phi_2 \left( \left\langle \frac{\partial \psi_0}{\partial \Phi_1} \middle| \frac{\partial \psi_0}{\partial \Phi_2} \right\rangle - \left\langle \frac{\partial \psi_0}{\partial \Phi_2} \middle| \frac{\partial \psi_0}{\partial \Phi_1} \right\rangle \right)$$

The integrand is the curvature of a certain closed 3-dimensional hypersurface in 6-dimensional space [48, 50].  $i/2\pi$  times the area integral of the curva-

<sup>5</sup>At least, a similar property for the “double Aharonov-Bohm geometry”, a torus pierced by two fluxes, has been proven.

<sup>6</sup>More specifically, a torus with flat surface is typically used in theoretical work, which is realised as a square  $0 \leq x, y \leq L$  where points  $(0, y)$  and  $(L, y)$  are defined to be the same point, as are  $(x, 0)$  and  $(x, L)$ .

ture is a topological invariant known as the first Chern number [51, 52] which is an integer, and thus resistance quantization (1.9) is established. This is, however, still not a rigorous proof as only bulk conductivity is studied. Quantum field-theoretical calculations by Ishikawa and others [53, 54], especially those taking the edges into account [55], provide the most complete understanding of the quantum Hall effect.

A detailed analysis [41] shows that the mobility gap occurs not only in a slowly varying disorder potential. If an arbitrary strong as well as fast-varying potential is added in some isolated regions that don't cross the QHE domain from side to side and are sufficiently far away from each other, the current quantization is preserved. Clearly, addition of such potential can change some extended states into localized ones. However, the energies of the remaining extended states will still be close to those of the unperturbed LL's, and the mobility gap is preserved. Furthermore, an additional omnipresent, fast-varying but sufficiently weak potential  $V_W$  will also preserve the mobility gap: a very weak potential cannot turn too many localized states into extended ones, and the energies of the existing extended states can change by at most  $\max(|V_W|)$  which is assumed small. Finally, electron-electron interaction is a small correction that preserves the mobility gap as well; in fact, it can create additional gaps, leading to the fractional quantum Hall effect.

It appears that not only does the disorder preserve the QHE (up to a point), but even facilitates it. Indeed, plateaus in magnetoresistance are observed when the only states at the Fermi level are the edge states and bulk localized states. The stronger the disorder, the more localized states are there for the Fermi level to go through as it moves between two Landau levels, and therefore the plateaus become wider. However, the exact quantization breaks down if the disorder is too strong.

### 1.3.2 Current-induced breakdown of quantum Hall effect

The area for practical application of the quantum Hall effect is resistance metrology, and it means that measurements of quantized Hall resistance must be as accurate as possible. One of the most important factors limiting the precision is the signal to noise ratio which can be improved by increasing the excitation current used in the measurement. However, there is always a limit to how much current a quantum Hall device can sustain, and if that limit is exceeded, the QHE breaks down [56–59]: the longitudinal resistance becomes finite, and the Hall resistance starts to deviate from the quantized value (1.9). A typical current dependence of the longitudinal resistivity in a GaAs device is shown in Figure 1.9. Strictly speaking, any finite current will cause a deviation from

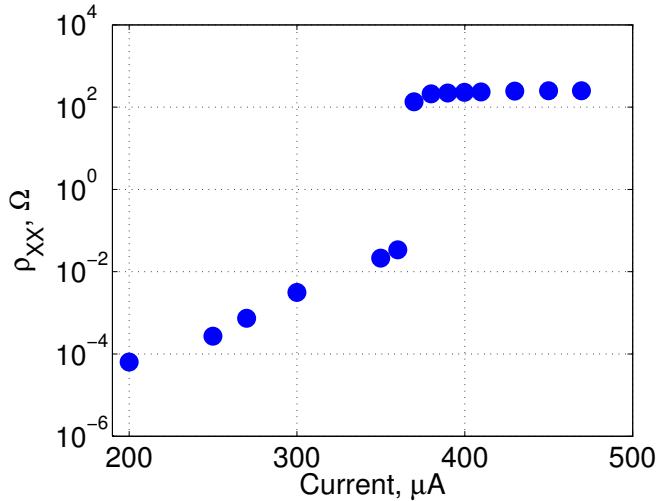


Figure 1.9: An example of dependence of the finite longitudinal resistivity on the excitation current in a GaAs-based QHE device (adapted from [61]).

the exact resistance quantization, but this effect can, in principle, be arbitrarily small. The measurement current is usually chosen under the assumption that the correction to the Hall resistance is on the order of the longitudinal resistivity, which is sometimes the case [60], although in other situations the correction can actually be much smaller [58]. The exact value of the critical current can be defined as the one at which the measured longitudinal voltage exceeds certain arbitrary threshold (typically on the order of a microvolt which is small but still well above the noise level of a good voltmeter).

The critical current (at least in GaAs) is often proportional to the width of the device [62, 63]; when a nonlinear width dependence is observed [64, 65], the critical current is typically smaller than usual, suggesting that those samples are somewhat defective. This means that the breakdown current density is the proper quantity to use, and it is a property of the material. In the best GaAs devices, the breakdown current density is on the level of 1 A/m.

The most widely accepted theory, the one by Komiyama [66, 67], claims that the QHE breakdown is caused by overheating of the electron system. Even at small currents in a “perfect” quantum Hall state, there is a finite, although vanishingly small, longitudinal resistivity  $\rho_{xx}$  due to the finite temperature. This means that the power density equal to  $\rho_{xx}j^2$ , where  $j$  is the current density, will be dissipated inside the device, bringing the electron temperature  $T_e$  somewhat above the lattice temperature  $T_L$ . In turn,  $\rho_{xx}$  increases with

increasing  $T_e$  (since the QHE breaks down at high temperatures). The final electron temperature is then found from the power balance equation

$$\rho_{xx}(T_e) j^2 = \frac{\mathcal{E}(T_e) - \mathcal{E}(T_L)}{\tau(T_e)}$$

where  $\mathcal{E}(T_e)$  is the thermal energy of the electrons per unit area and  $\tau(T_e)$  is the energy relaxation time that describes thermal coupling between the electrons and the lattice. This can be rewritten as

$$\left( \frac{1}{\rho_{xx}(T_e)} \frac{\mathcal{E}(T_e) - \mathcal{E}(T_L)}{\tau(T_e)} \right)^{1/2} = j \quad (1.15)$$

Thus the model does not make a distinction between temperature-induced breakdown and current-induced breakdown. At small electron temperatures, the left part of (1.15) increases with  $T_e$  [68], which means that the equilibrium electron temperature increases with the current density. This is what causes the initial slow increase of  $\rho_{xx}$  seen in Figure 1.9. The subsequent abrupt jump is attributed to non-monotonous behavior of the left part of the equation 1.15 at higher currents [66, 68].

The critical current is a crucial figure of merit for the performance of a quantum Hall device, since a larger measurement current translates into a better precision. One important trend is that the larger the mobility gap, the larger is the critical current. This means that small separation between the Landau levels or a strong disorder that broadens the regions of extended states and shrinks the mobility gap will ruin the performance of the device by decreasing the critical current. For example, odd filling factors, as well as filling factors above 4, cannot be used in metrology for this reason.

## 1.4 Quantum Hall effect in graphene

Landau levels in graphene are different from the ones in normal semiconductors. For monolayer graphene, the LL's calculated by substituting Hamiltonian (1.1) into (1.11) are (for both valleys)

$$\mathcal{E}_n = \pm v_F \sqrt{2\hbar e B n}, \quad n \geq 0$$

In a simple model, each level has an additional four-fold degeneracy due to spin and valley degrees of freedom, so that every filled LL contributes  $4e^2/h$  to the Hall conductance. The exception is the level  $\mathcal{E}_0 = 0$  which, although it

has the same degeneracy, must be treated specially because it is at the border of two bands. When this level is completely filled with electrons, half of its states belong to the completely filled valence band, and therefore do not contribute to the conductance, so that the whole level contributes only  $2e^2/h$ . Thus the most commonly observed sequence of filling factors for QHE in monolayer graphene is  $\nu_n = 4(n + \frac{1}{2}) = 2, 6, 10, \dots$ . Both spin and valley degeneracy can be lifted in strong magnetic fields [69–72], leading to an extended series such as  $\nu = 0, 1, 2, 4, 6, 10, 14, \dots$ , but the additional filling factors are rarely seen and of no interest for metrology due to small separation between the split LL's.

In bilayer graphene with Hamiltonian (1.2), the energies of the Landau levels are

$$\mathcal{E}_n = \pm \frac{\hbar e B}{m} \sqrt{n(n-1)}$$

Each level has the same four-fold degeneracy as the one present in the monolayer, except for the zero-energy level which is eight-fold-degenerate because  $\mathcal{E}_0 = \mathcal{E}_1$ . Every filled LL contributes  $4e^2/h$  to the Hall conductance, so the filling factors are  $\nu_n = 4n$ ,  $n \geq 1$ :  $\nu = 4, 8, 12, \dots$ . If, however, a band gap is created by a gate, so that the Hamiltonian is (1.3) instead, then the  $\mathcal{E} = 0$  level separates into two four-fold-degenerate levels belonging to different bands, and thus the  $\nu = 0$  filling factor is added.

Unlike in a conventional semiconductor, Landau levels in monolayer graphene are not equidistant: the separation  $|\mathcal{E}_{n+1} - \mathcal{E}_n|$  is maximal for  $n = 0$  and decreases with increasing  $n$ , which constitutes an additional reason why only the lowest filling factor ( $\nu = 2$ ) is relevant for metrology. The equivalent temperature corresponding to the separation between the two lowest Landau levels is  $\Delta\mathcal{E}/k_B = v_F \sqrt{2\hbar e B}/k_B \approx (460 \text{ K/T}^{1/2}) \cdot \sqrt{B}$ . To compare, in gallium arsenide  $\Delta\mathcal{E}/k_B = \hbar e B/mk_B \approx (20 \text{ K/T}) \cdot B$ , and in indium antimonide which probably has the lowest finite charge carrier effective mass among all known semiconductors (bilayer graphene included)  $\Delta\mathcal{E}/k_B \approx (75 \text{ K/T}) \cdot B$ . Typical conditions for high-precision quantum Hall effect in gallium arsenide are  $B = 11 \text{ T}$  and  $T = 1.3 \text{ K}$  [2] which means that the ratio  $\Delta\mathcal{E}/k_B T \approx 170$ . Theoretically, in indium antimonide the same ratio of  $\Delta\mathcal{E}/k_B T$  is achieved at 3 tesla and 1.3 kelvin, and in monolayer graphene at 3 tesla and 4.7 kelvin. This explains why graphene-based quantum Hall devices can operate at higher temperatures and lower fields.

## 1.5 Epitaxial graphene on silicon carbide

There are three main techniques for producing graphene: mechanical exfoliation of bulk graphite, chemical vapour deposition (CVD) growth on various substrates, and epitaxial growth on silicon carbide. Exfoliated graphene has the highest quality, but forms individual flakes of small size, rarely bigger than 10 microns. CVD-grown graphene sheets can be indefinitely large but are usually polycrystalline. Epitaxial graphene formed on high quality SiC has the same crystalline orientation throughout the wafer, which is defined by the crystal lattice of the substrate, and can be therefore regarded as a large single-crystal sheet. The latter is true for graphene produced both by thermal decomposition of the substrate (the original “epitaxial graphene”) and by CVD on SiC. However, since not much is known about the difference between the two, and the second method has also been referred to as “epitaxy” [73], we will not make a distinction here. All material used in our work was produced by thermal decomposition.

Quantum Hall metrology applications impose certain requirements on the material. Despite their high quality, using exfoliated flakes is problematic due to the small size. Boundaries between single-crystal domains (grains) in polycrystalline CVD graphene present themselves as regions of strong disorder covering the whole sample like a mesh, which breaks down the QHE [74, 75]. Epitaxial graphene which is both large-area and single-crystal is therefore the natural choice.

Production of graphene by thermal decomposition of silicon carbide is performed at temperatures above 1000° C in argon atmosphere. At these temperatures, silicon atoms sublime from the surface and the remaining carbon atoms form graphene layers. To mention, CVD growth is done at similar temperatures, but in a mixture of argon and hydrocarbons, so that extra carbon is deposited instead. The first layer of carbon atoms, called the buffer or interface layer, is covalently bonded to the substrate [76]. Although the buffer layer has the honeycomb structure of graphene [77], its conductivity is completely destroyed by the interaction with the substrate. This layer can therefore be regarded as a part of the substrate.

High quality epitaxial graphene can (at least, so far) only be produced on hexagonal silicon carbide, on a surface which follows the (0001) crystallographic plane. However, the SiC wafers are cut out of a large bulk crystal, and therefore, their surface cannot exactly follow a crystallographic face. Namely, the surface is neither completely flat nor perfectly parallel to the crystallographic direction, so it consists of atomically flat areas separated by few angstrom high atomic steps. High temperatures involved in graphene growth

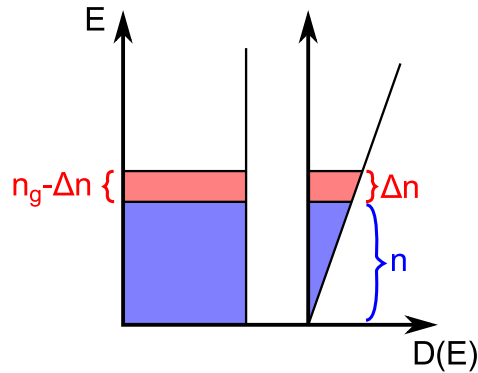


Figure 1.10: Charge transfer between epitaxial graphene and the substrate. This picture does not take into account the possibility that an electric field between graphene and the localized states in the substrate can create a potential difference between the two, shifting the energy levels with respect to each other. However, there is no universally accepted theory that would give quantitative agreement with the experimentally observed values of the gate efficiency, and for a qualitative explanation, this simple picture is sufficient.

lead to restructuring of the surface which causes the steps to bunch together, increasing their height to anywhere between 1 and 10 nanometers. However, graphene layers are continuous over these steps [78, 79], and although the steps introduce disorder due to high curvature of the graphene sheet, this disorder is not strong enough to break down the QHE.

The steps on the surface of SiC are closely related to another, more important source of graphene non-uniformity because formation of graphene layers, at least by the better-studied thermal decomposition technique, originates at the steps [80–83]. When monolayer graphene is formed across the entire surface, the second layer will typically have already started to form at some places, mainly along the steps. Epitaxial graphene will therefore not be completely single-layer, but also have some inclusions of two and possibly more layers. These multi-layer patches are an important consideration for any electronic applications of epitaxial graphene.

## 1.6 Substrate effects in epitaxial graphene

When epitaxial graphene is electrostatically gated, the change of carrier density in graphene  $\Delta n$  is significantly less than the density of electrons on the gate  $n_g$  [84–86]. The gate efficiency  $\Delta n/n_g$  in the experiments was on the

level of 0.1 or even lower. This effect has been attributed to charge transfer between graphene and localized surface states in the substrate [87], similar to the mechanism responsible for the Fermi level pinning in semiconductors. When the gate voltage is applied, only a part of the induced surface charge goes into graphene, while the rest goes into the surface states, so that chemical potentials in graphene and the surface states stay aligned. A simplified picture of this is shown in Figure 1.10.

This charge transfer also affects the QHE [88], because the Fermi level in graphene depends not only on the carrier density but also on magnetic field:  $\mathcal{E}_F = \mathcal{E}_F(n, B)$ , as shown in Figure 1.11. Without the magnetic field, the carrier density and the Fermi level have some values  $n_0$  and  $\mathcal{E}_0 = \mathcal{E}_F(n_0, 0)$ , respectively, and the Fermi levels in graphene and the surface states are aligned. Normally, the carrier density would always stay at  $n_0$ , but the effects of charge transfer make it change with the field. Consider a magnetic field such that the Fermi level at carrier density  $n_0$  is in the middle of a Landau level. Without the charge transfer, this would correspond to the middle of the transition between two plateaus (Figure 1.11a). At this point, the Fermi level has the same value as it had without magnetic field:  $\mathcal{E}_F(n_0, B) = \mathcal{E}_0$ , thus the charge transfer in this situation does not have any effect. As the field increases (Figure 1.11b), the Fermi level  $\mathcal{E}_F(n_0, B)$  will increase above  $\mathcal{E}_0$ , which would bring it above the Fermi level of the surface states. To keep the Fermi levels aligned, some electrons have to move from graphene into the substrate, decreasing the carrier density in graphene. Due to this decrease of the carrier density, the plateau will start at a smaller field as compared to a situation without the charge transfer. At some point on the plateau (Figure 1.11c),  $\mathcal{E}_F(n_0, B)$  is back to  $\mathcal{E}_0$ , and therefore the carrier density in graphene is back to  $n_0$ . As the magnetic field further increases (Figure 1.11d),  $\mathcal{E}_F(n_0, B)$  will decrease below  $\mathcal{E}_0$ , which will cause an increase of carrier density, and therefore the plateau will end at a higher field.

Thus the charge transfer widens the quantum Hall plateaus, and the effect is especially prominent for the  $\nu = 2$  plateau due to the largest separation between the lowest Landau levels. In fact, the end of the  $\nu = 2$  plateau in epitaxial graphene has never been observed: the plateau can start at 1 tesla and continue beyond 20 tesla [9]. Figure 1.12 shows a comparison of magnetic field dependence of the QHE critical current density in gallium arsenide and graphene: the region of fields where the quantization is observed is clearly much wider for graphene. Additionally, the current density itself is higher in graphene: 4 A/m at 7 tesla, compared to the typical maximum value of 1 A/m in GaAs. Furthermore, in graphene samples with a higher carrier density, crit-

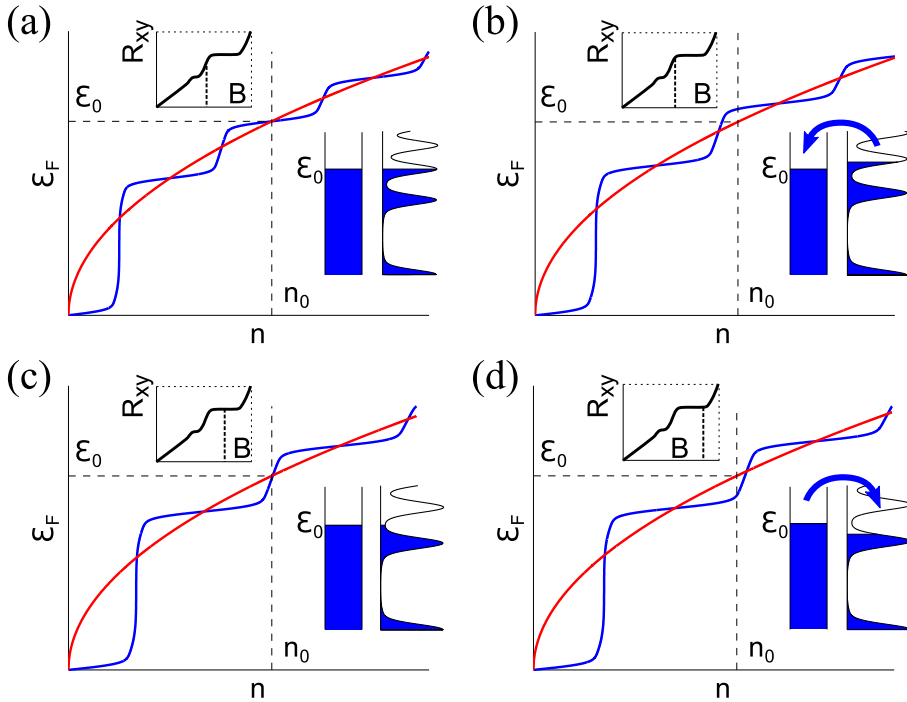


Figure 1.11: Fermi level dependence on carrier density with (blue; calculated assuming Gaussian shape of the LL's with an arbitrary width) and without (red) magnetic field. The plots and the insets show what the situation would be without the charge transfer, and arrows in the insets indicate how the charge transfer would change it. In the order of increasing field: a) the middle of the transition between the  $\nu = 10$  and  $\nu = 6$  plateaus; b) before the onset of the  $\nu = 6$  plateau; c) the middle of the  $\nu = 6$  plateau; d) the end of the  $\nu = 6$  plateau.

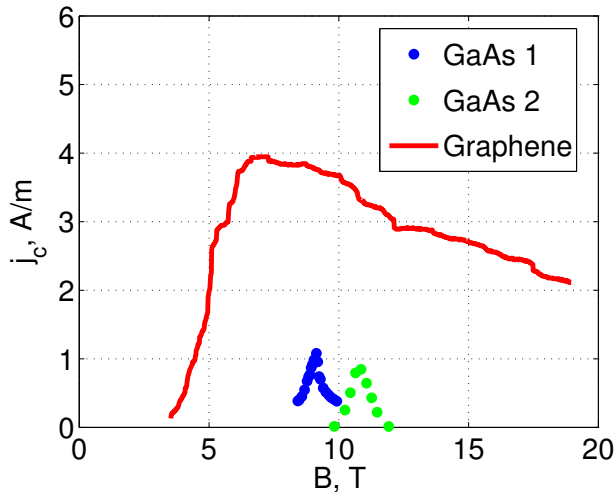


Figure 1.12: Magnetic field dependence of the QHE breakdown current density in gallium arsenide and epitaxial graphene. Data taken from [57, 61] (GaAs) and [9] (graphene).

ical current densities up to 40 A/m have been observed at 15-25 tesla [9, 10]. These remarkably high values of the breakdown current density have been attributed mainly to a better thermal coupling between the electrons and the lattice in epitaxial graphene [9], which is another special property of this substrate.

## 1.7 Quantum Hall circuits

Good quantization precision in the QHE is only observed for plateaus with a low even filling factor, usually  $\nu = 2$  and possibly  $\nu = 4$ . Therefore a single quantum Hall device can only provide a standard of resistance with a value  $h/2e^2 \approx 13 \text{ k}\Omega$  or  $h/4e^2 \approx 6.5 \text{ k}\Omega$ . However, resistance values equal to various rational multiples of  $R_H = h/\nu e^2$  can be achieved by adding interconnections between different contacts of the same device [89] or by connecting several devices in series, in parallel or in an arbitrary network [90]. The following sections will describe the analog of Kirchhoff's laws for a quantum Hall device in a circuit, and a practical method of making parallel connection which is insensitive to the parasitic resistance of the contacts and the connecting wires. Finally, direct contact between quantum Hall domains with different filling

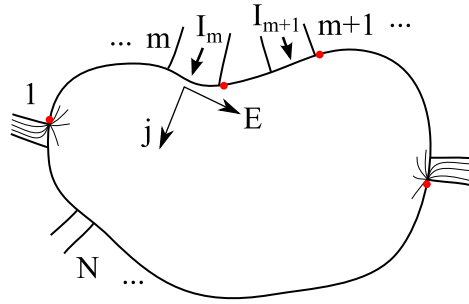


Figure 1.13: A sketch of a quantum Hall device. Red dots show places where the potential drop occurs (for the case  $R_H < 0$ ; for  $R_H > 0$  they will be on the other side of the contacts), and the rest of device boundary are equipotential lines.

factors will be described.

### 1.7.1 Quantum Hall device as a circuit element

The behavior of a quantum Hall device in an electric circuit can be described using resistivity tensor (1.10). By a quantum Hall device we mean a quantum Hall domain with a number of contacts on its border (Figure 1.13). Contacts which are inside the quantum Hall domain or completely encircle it as in Corbino disk geometry (Figure 1.8) will not be considered because no current can flow to or from such contacts. A simple approach using the local resistivity tensor yields the correct distribution of potential on the border of the device, although not in the bulk.

According to (1.10), the electric field is perpendicular to the current density in the quantum Hall domain. Therefore, the edges of the quantum Hall domain are equipotential lines since the current at an edge flows parallel to it. Potential drop across a contact is given by [91]

$$V = \int \vec{E} d\vec{l} = \int R_H \vec{j} d\vec{n} = R_H I$$

where  $I$  is the current flowing through that contact.

Electrostatic calculations show that this potential drop only occurs in a narrow region on one side of the contact [89]. The following rule applies: consider a current density vector  $\vec{j}$  pointing out of the contact, as shown for  $m$ -th contact in Figure 1.13. Then the electric field calculated as  $\vec{E} = \rho \vec{j}$  with resistivity (1.10) will point towards that particular side of the contact where the potential drop happens. This side will be different depending on the sign of

$R_H$ , which, in turn, is determined by the sign of charge carriers (electrons or holes) and the direction of magnetic field.

The potential of each contact is therefore equal to the potential of one of edge regions next to it. The potential difference between two neighbouring contacts is then given by [89]

$$V_{m+1} - V_m = \begin{cases} R_H I_{m+1} & , R_H > 0 \\ R_H I_m & , R_H < 0 \end{cases} \quad (1.16)$$

assuming that the contacts are numbered in the clockwise direction, with  $I_m > 0$  for the current flowing into the quantum Hall domain and  $I_m < 0$  for the current flowing into the contact.

Equations (1.16) provide a complete description of a multi-terminal quantum Hall device in an electric circuit.

### 1.7.2 Quantum Hall arrays

A quantum Hall array is a device consisting of a number of Hall bars connected in series or parallel, which nominally has resistance of a rational multiple of  $R_H$ . However, unlike for single Hall bars, the relation  $R_{xy} = (p/q) \cdot h/e^2$  cannot possibly be exact for an array. For example, consider two similar Hall bars which are connected in parallel as shown in Figure 1.14a. In an ‘‘ideal’’ circuit with resistanceless wires, since the two-point resistance of each Hall bar is the same (equal to  $R_H$ ),  $V_{2-4} = V_{2'-4'} = R_H I/2$  and  $R_{A-B,2-4} = R_{A-B,2'-4'} = R_H/2$ .

In a real device, though, the interconnecting wires have finite resistance, and so do the contacts to the Hall bars. If these finite connection resistances are taken into account (Figure 1.14b) then

$$R_{A-B,2-4} = R_H \frac{I_1}{I} = \frac{R_H}{2} \left( 1 - \frac{\epsilon_{11} - \epsilon_{21}}{2} - \frac{\epsilon_{13} - \epsilon_{23}}{2} \right) \quad (1.17)$$

where  $\epsilon_{ij} = R_{ij}/R_H$ . Assuming that the spread in  $\epsilon_{ij}$  is on the order of  $\epsilon_{ij}$ , (1.17) can be written as  $R_{A-B,2-4} = R_H/2 \cdot (1 + O(\epsilon))$ . This contribution of contact/lead resistance would drastically decrease the accuracy of a resistance standard, while in single Hall bars such parasitic resistance does not directly affect a four-point measurement.

The effect of connection resistance will always be present, but it can be significantly reduced by making additional interconnections between the Hall bars [92], so that  $K$  pairs of contacts of each Hall bar are connected to corresponding pairs of contacts of all other Hall bars, as shown in Figure 1.14c for two Hall bars and  $K = 3$ . If again an extra resistance is added at each contact

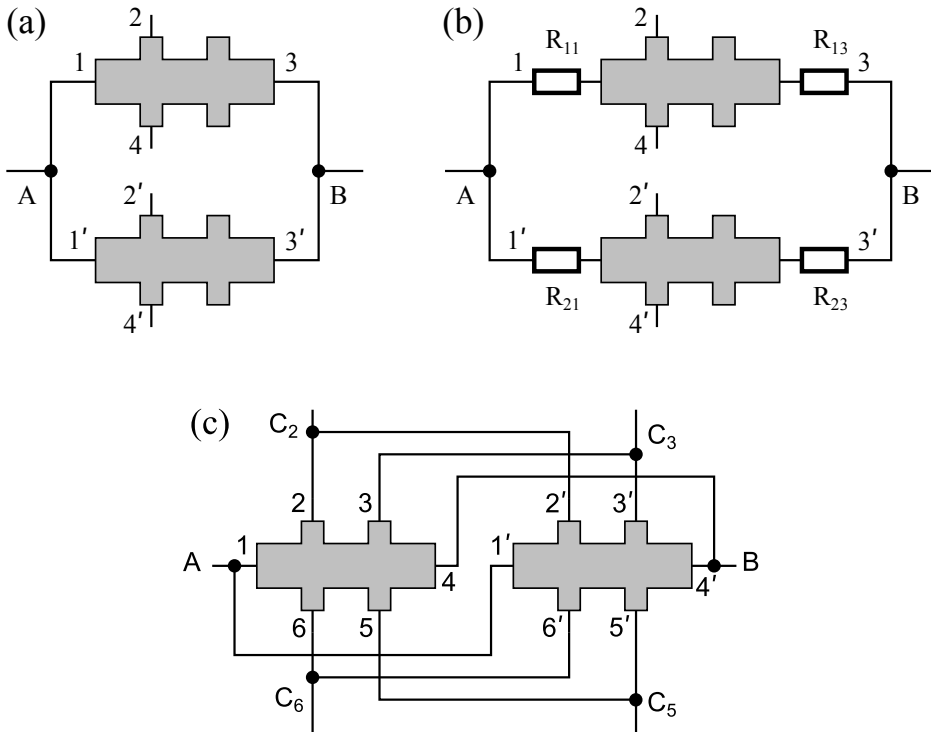


Figure 1.14: Parallel connection of quantum Hall bars. (a) Two Hall bars, simple parallel connection, ideal case. (b) Two Hall bars, simple parallel connection, real case with a finite connection resistance. (c) Two Hall bars, triple-parallel connection.

of each Hall bar, the various 4-point transverse resistances will be less affected in this case. For example, for two Hall bars,  $K = 2$  and  $R_H > 0$  [92]

$$\begin{aligned} R_{A-B,3-6} &\approx \frac{R_H}{2} \left( 1 + \frac{(\epsilon_{11} - \epsilon_{21})(\epsilon_{12} - \epsilon_{22})}{4} + \frac{(\epsilon_{13} - \epsilon_{23})(\epsilon_{14} - \epsilon_{24})}{4} \right) = \\ &= \frac{R_H}{2} (1 + O(\epsilon^2)) \end{aligned}$$

In general, for  $N$  Hall bars connected in parallel and any  $K \geq 1$  and  $1 \leq j \leq K$

$$\begin{aligned} R_{A-B,j-(j+K)} &= \frac{R_H}{N} (1 + O(\epsilon^j)), R_H > 0 \\ R_{A-B,(K+2-j)-(2K+2-j)} &= \frac{R_H}{N} (1 + O(\epsilon^j)), R_H < 0 \end{aligned} \quad (1.18)$$

The derivation of these formulas from (1.16) can be found in Appendix A. The two-point resistance between the source and the drain has  $O(\epsilon)$  correction, similar to the case simple parallel connection, but increasingly better precision (up to  $O(\epsilon^K)$ ) is available with different pairs of voltage probes. The probes that produce the best precision are the ones for  $j = K$ :  $K$  and  $2K$  for  $R_H > 0$ , and  $2$  and  $K + 2$  for  $R_H < 0$ . A similar multiple-connection idea can also be applied to series [92] and bridge [93] configurations, and a combination of these can yield various rational multiples of  $R_H$ , limited by how many Hall bars can be successfully integrated together in a real device.

### 1.7.3 Bordering QHE domains with different filling factors

There is another possibility for a contact between quantum Hall domains: two domains with different filling factors can join each other directly, without a metallic contact in between, as shown in Figure 1.15. When the two filling factors have the same sign, the situation has to be different from a contact through metallic region. For example, when the filling factors are equal, longitudinal resistance between the two domains is zero for a direct contact (at least, if the materials are the same), and  $h/\nu e^2$  for a series connection through a metal contact.

Similar to the metal-QHE domain interface, potential distribution across the border between two QHE domains can be correctly deduced from electrostatic calculations using resistivity tensor (1.10). It thus does not matter whether or not the domains are made of the same material; only the values

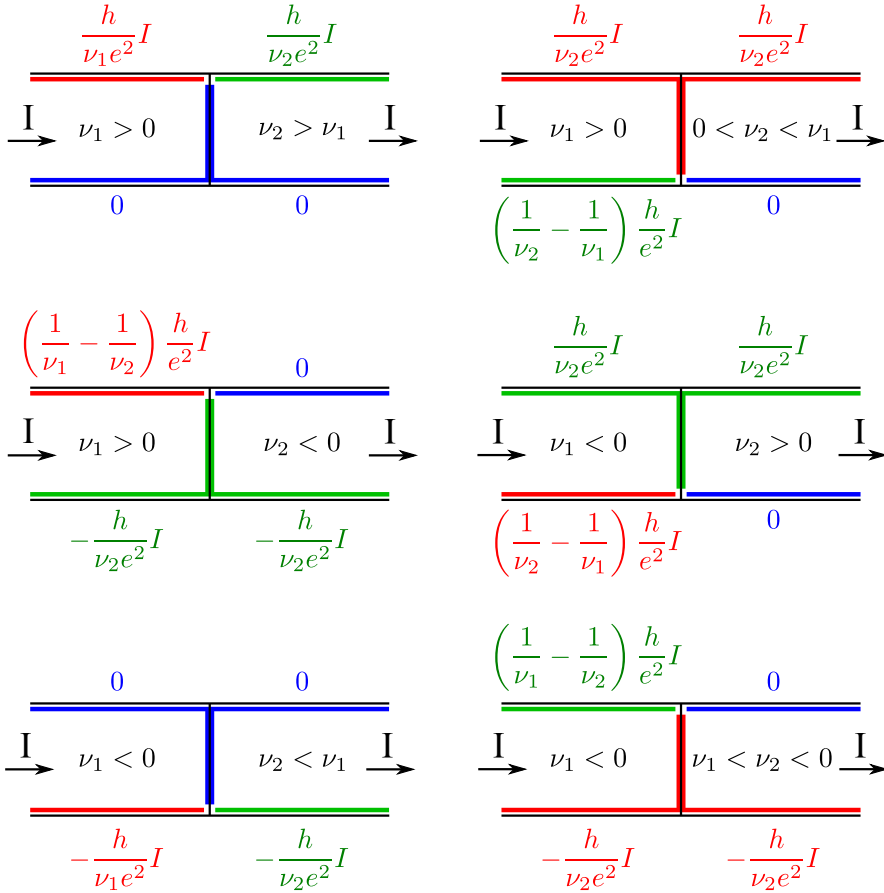


Figure 1.15: Potential distribution across the border between two quantum Hall domains with different filling factor, depending on the sign of the filling factors and the sign of their difference.

of the filling factors are relevant. The result is that the longitudinal resistance between the two domains on at least one of the two sides will always be zero [94, 95]. Which side will it be, can be determined from the fact that the longitudinal resistance on the other side, given the transverse resistances (1.9) in each domain, will never be negative.

The exact distribution of the potential will depend on the sign of the filling factors, and also on which filling factor is greater. All possible situations are shown in Figure 1.15. In particular, when the filling factors are of opposite signs, the situation is the same as if there was a metal contact (without any contact resistance) in between. These results agree with experimental data obtained both in quantum Hall domains made of the same material with the filling factor modulated by a local gate [94, 96–99] and in planar heterostructures of mono- and bilayer graphene [100, 101].

## 1.8 Optical reflection and absorption of graphene

The original discovery of exfoliated graphene was made possible by the fact that due to its electrical conductivity, even the monolayer can reflect and/or absorb enough light to be detected in an optical microscope. The visibility of graphene depends on the substrate, and can be quantified by the relative contrast

$$C_R = \left| \frac{R_G}{R_0} - 1 \right|; C_T = \left| \frac{T_G}{T_0} - 1 \right|$$

where  $R_G$  and  $T_G$  are reflection/transmission coefficients of the substrate with graphene, and  $R_0$  and  $T_0$  are those of the bare substrate. These quantities can be calculated from the first principles, and such calculations are commonly used to choose an optimal substrate that would provide the best contrast, thus facilitating optical inspection.

Being only one or few atomic layers thick, graphene does not have a refraction index<sup>7</sup>, and must instead be treated as purely 2-dimensional. Such treatment consists in modifying the boundary conditions in the derivation of the Fresnel equations [102] (Figure 1.16). For normal incidence, the boundary conditions without the conductive layer are those of continuity for  $\vec{E}$  and  $\vec{B}$ :

$$E_x(-0) = E_x(+0); B_y(-0) = B_y(+0)$$

---

<sup>7</sup>Which, however, did not prevent researchers from modeling graphene as a 0.335 nm thick film with a refraction index close to that of bulk graphite, leading to a surprisingly good agreement with experiments in some cases.

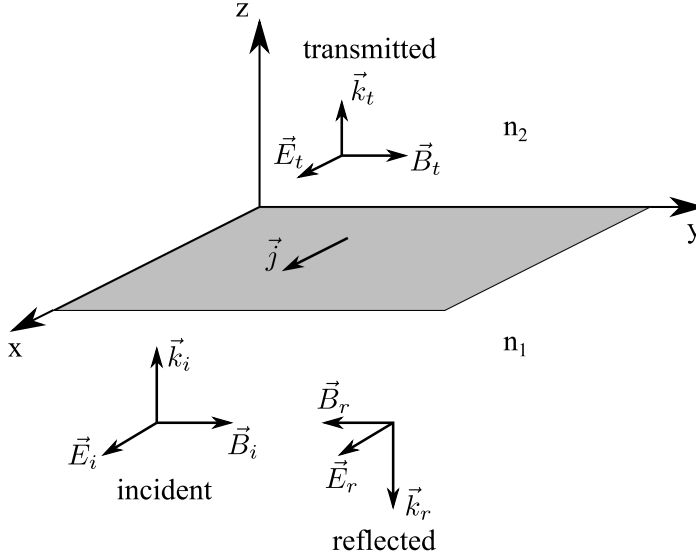


Figure 1.16: Fresnel reflection with a graphene layer at the border

which leads to the standard formulas for the reflection and transmission coefficients of the bare interface

$$R_0 = \frac{(n_1 - n_2)^2}{(n_1 + n_2)^2}; T_0 = \frac{4n_1 n_2}{(n_1 + n_2)^2}$$

In the presence of a conductive layer with 2-dimensional conductivity  $\sigma$  (which is the high-frequency conductivity at the frequency of the light), the boundary condition for the magnetic field is modified to

$$B_y(-0) - B_y(+0) = \mu_0 j_x(0) = \mu_0 \sigma E_x(0)$$

As a result, the reflection and transmission coefficients become

$$R_G = \frac{|n_1 - n_2 - \sigma Z_0|^2}{|n_1 + n_2 + \sigma Z_0|^2} \approx \frac{(n_1 - n_2 - \text{Re}(\sigma) Z_0)^2}{(n_1 + n_2 + \text{Re}(\sigma) Z_0)^2}$$

$$T_G \approx \frac{4n_1 n_2}{(n_1 + n_2 + \text{Re}(\sigma) Z_0)^2}$$

where  $Z_0 = \mu_0 c$  is the free space impedance. At the frequencies of visible light, the real part of the conductivity of single- or few-layer graphene is almost frequency-independent and is close to  $Ne^2/4\hbar$ , where  $N$  is the number of layers [102–104]. This yields expressions for the optical contrast

$$C_R \approx \frac{4n_1}{n_2^2 - n_1^2} \pi \alpha N; C_T \approx -\frac{2}{n_1 + n_2} \pi \alpha N \quad (1.19)$$

where  $\alpha$  is the fine structure constant.

If there is a thin transparent film at the surface of the substrate, such as a layer of silicon oxide on top of silicon, the contrast can be significantly increased due to interference effects [105, 106]. However, in the case of epitaxial graphene, high quality silicon carbide is only available as thick wafers, so the contrast cannot be enhanced by the interference, and is thus set (for normal incidence) by (1.19).



# Chapter 2

## Experimental techniques

### 2.1 Microfabrication

Choosing a suitable recipe for fabricating graphene devices is not necessarily a straightforward procedure. The reason is that exposing graphene to various substances at different fabrication steps could potentially affect its electronic properties due to contamination or even chemical modification. This can result, for example, in doping or increased disorder. Regarding quantum Hall devices, a strong disorder can break down the QHE or, in a less extreme case, “decrease the quality” of the QHE, that is, reduce the critical current. Another important concern for QHE devices is achieving low contact resistance (usually less than 100 ohm is required), and this can be affected by the choice of the contact material as well as by the impact of the preceding fabrication steps on the graphene-metal interface formed during contact deposition.

All our devices were made using a similar fabrication procedure. The procedure that we use has been essentially unchanged since our first successful results on the QHE in epitaxial graphene [107] which show that this fabrication can both yield low-resistance contacts and preserve resistance quantization (later results [10] having demonstrated that high critical currents are possible as well).

We usually employ electron beam lithography on every fabrication step. There are two types of fabrication steps: etching graphene by oxygen plasma through the mask of P(MMA-MAA) e-beam resist (Figure 2.1) and lift-off deposition using P(MMA-MAA) as the bottom layer (Figure 2.2). This way, P(MMA-MAA) and solvents used for its dissolution or development are the only substances which graphene ever gets in contact with. The residue of P(MMA-MAA) which is left behind on the surface of the devices after the fabrication

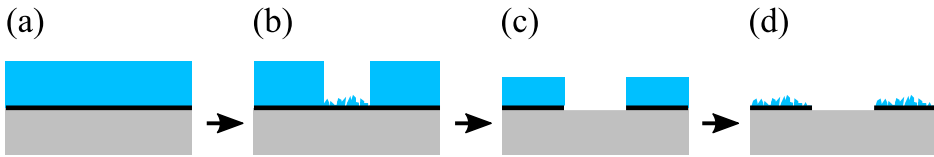


Figure 2.1: Patterning graphene by plasma etching. (a) The chip is covered with resist. (b) The resist is patterned by e-beam or photolithography. Developing the resist does not remove it completely, leaving behind a thin residue layer. (c) Graphene is etched by oxygen plasma. The plasma etches the resist as well, both vertically and sideways, so that the resulting opening in graphene is wider than the one lithographically defined. (d) The resist is removed, leaving behind residue on graphene.

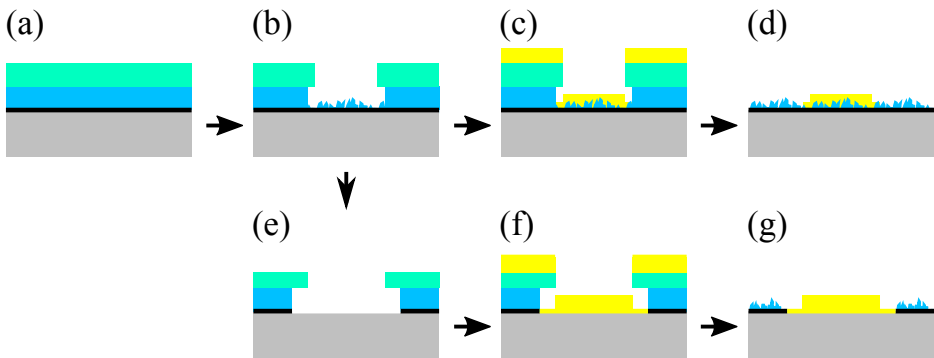


Figure 2.2: Lift-off deposition. (a) The chip is covered with two different resists. (b) The resist layers are patterned, leaving behind the residue. (c) The film is deposited directly on graphene. (d) The remaining resist, together with the excess deposited material, is removed. (e)-(g) Deposition preceded by oxygen plasma etching which removes graphene from under the deposited film. The final film protrudes beyond the opening in the top resist layer due to lateral mobility of the deposited material, which can result in electrical contact to graphene.

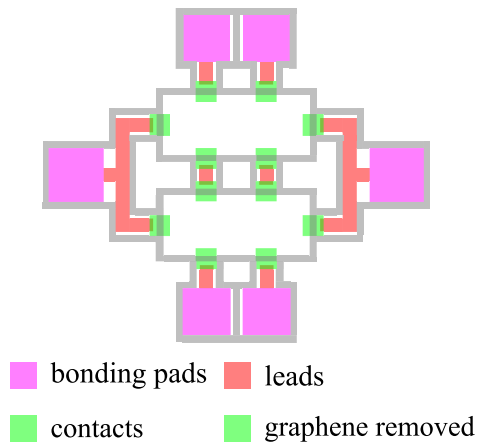


Figure 2.3: An example of a pattern for two interconnected Hall bars. Bonding pads and leads are deposited with removal of graphene, and are completely surrounded by openings in graphene.

(Figure 2.1d, 2.2d, g) is most likely irrelevant because we encapsulate the samples in the very same polymer before the measurements. Deep UV photolithography with the same resists is also possible, and the only reason for choosing e-beam lithography was variability of the devices' layout.

The contacts to graphene were made by evaporating 5 nm Ti and at least 30 nm Au. Despite the contamination of the graphene-metal interface by the residue of the resist in the lift-off method (Figure 2.2b, c), low (sometimes below 1 ohm) contact resistance has been achieved by this technique. All other deposition (that of wire bonding pads and various metallic leads) is preceded by oxygen plasma etching because the adhesion of the deposited films to silicon carbide is much better than to graphene: this makes wire bonding possible, and the leads become resistant to accidental scratching. Despite graphene being etched away from under the leads and bonding pads, they still often make an electrical contact to the surrounding graphene sheet (Figure 2.2f, g), so it is important to etch additional trenches all the way around them, as shown in Figure 2.3.

A detailed description of every fabrication step can be found in Appendix B.

## 2.2 Optical microscopy

Optical microscopy, when applicable, is the most convenient imaging technique available because it is very fast and simple. For graphene, it has been originally widely used on exfoliated flakes to determine their position, size and thickness. In chapter 5 we will demonstrate that optical microscopy can also be applied for characterization of epitaxial graphene.

The most basic use case for optical microscopy is observing distribution of reflection or transmission coefficient of visible light at the surface of the substrate by detecting the image with either the eye or a CCD matrix. The more advanced techniques that allow seeing objects invisible to the simple optical microscopy will be described in the following sections.

### 2.2.1 Differential interference contrast

The basic optical microscopy cannot easily detect, for example, films with refraction index only slightly different from that of the environment<sup>1</sup>. Such object has very small reflection coefficient and close to unity transmission, and therefore the amplitude of the transmitted or reflected light is not significantly altered by the presence of the film. However, if the film is sufficiently thick (comparable to the wavelength or thicker), it can cause a significant change in optical path length or, equivalently, phase of the light passing through it. This is an example of a phase object which only becomes visible if the distribution of the phase (not just the amplitude as in “regular” microscopy) of the light is measured. That task can be accomplished by various phase imaging methods.

One of these methods, available as an additional option in commercial optical microscopes, is the differential interference contrast [108, 109]. The sample is illuminated by linearly polarized light which has been split into two slightly shifted beams with polarization perpendicular to each other (and at 45° to the original polarization) by a birefringent prism (Figure 2.4). The second birefringent prism combines the two beams back into one after they interact with the sample. Depending on the phase shift between the two beams, the resulting beam will have, in general, elliptic polarization: the amplitudes of the components parallel and perpendicular to the direction of the original linear polarization will be  $|\cos(\Delta\phi/2)|$  and  $|\sin(\Delta\phi/2)|$ , respectively, where  $\Delta\phi$  is the phase shift due to the possible gradient of phase in the sample. An additional polarizer that transmits only one of these components will convert

---

<sup>1</sup>Such films are common in biological specimens, which was the original motivation for developing phase imaging techniques

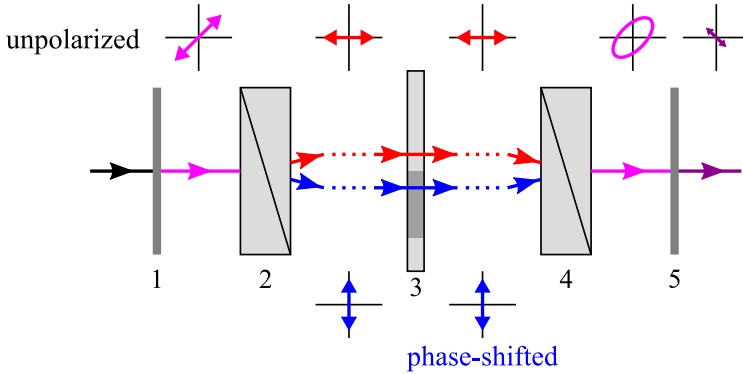


Figure 2.4: The setup for differential interference contrast microscopy. 1: polarizer; 2: birefringent prism; 3: sample; 4: second birefringent prism; 5: second polarizer.

this phase shift into amplitude, thus allowing direct imaging of phase gradients.

### 2.2.2 Transport of intensity phase imaging

Another method of phase imaging, which does not require any additional hardware, is based on the fact that phase gradients become visible in a defocused image [110]. The equation that relates phase gradients in the  $xy$  plane (the image plane) to the  $z$  component of the intensity gradient is derived from parabolic approximation to the Helmholtz equation [111]. This parabolic wave equation, also known as paraxial approximation [112, 113], is the equation satisfied by the Fresnel diffraction integral, and has the form<sup>2</sup>

$$\left( i \frac{\partial}{\partial z} + k + \frac{\nabla_{xy}^2}{2k} \right) u = 0$$

where  $\vec{\nabla}_{xy} = (\partial/\partial x, \partial/\partial y)$ ,  $k = 2\pi/\lambda$  is the wavenumber and  $u(\vec{r})$  is the complex amplitude of the wave field. Substituting  $u(\vec{r}) = \sqrt{I(\vec{r})} \cdot e^{i\phi(\vec{r})}$  leads to the transport of intensity equation

$$\frac{\partial I}{\partial z} = -\frac{1}{k} \vec{\nabla}_{xy} \cdot (I \cdot \vec{\nabla}_{xy} \phi) \quad (2.1)$$

<sup>2</sup>An often-encountered form of this equation with the  $ku$  term absent is obtained by substituting  $u = \tilde{u}e^{ikz}$

This equation can be readily applied to the wave field in an optical microscope. At the focal plane ( $z = z_0$ ),  $\sqrt{I(x, y, z_0)} e^{i\phi(x, y, z_0)} = \sqrt{I_0(x, y)} e^{i\phi_0(x, y)}$  is proportional to the complex transmission or reflection coefficient of the sample. From the experimental point of view, to get a qualitative image of a phase object, it is enough to simply defocus: even if the intensity at  $z = z_0$  is uniform, (2.1) ensures that a defocused image at  $z \neq z_0$  will show the phase gradients. However, it is also possible to get quantitative information about the phase. To do this, one can take two digital images at different focus settings (one focused,  $I_1(x, y)$  and one defocused,  $I_2(x, y)$ ) and subtract them to approximate the partial derivative in the  $z$  direction:

$$\frac{\partial I}{\partial z} \approx \frac{I_2 - I_1}{\Delta z}$$

Here  $\Delta z$  is the displacement of the final image of the sample with respect to the CCD matrix. The phase can then be calculated by numerically solving two Poisson equations:

$$\nabla^2 \psi = -\frac{k}{\Delta z} (I_2 - I_1) \quad (2.2)$$

$$\nabla^2 \phi = \vec{\nabla} (I_1 \vec{\nabla} \psi) \quad (2.3)$$

The intensity can be measured in arbitrary units. An additional parameter which does not enter (2.2) and (2.3) explicitly, but is required for a numerical solution, is the physical distance between two pixels of the image, which is the distance between the pixels of the CCD camera. However, the equations stay invariant if that parameter is replaced by the distance between the corresponding points on the sample, and at the same time  $\Delta z$  is replaced by the displacement of the sample, so the physical characteristics of the microscope are unimportant. Finally, for pure phase objects (uniform intensity in the focused image:  $I_1(x, y) \approx \text{const}$ ) there is only one Poisson equation to solve:

$$\nabla^2 \phi = -\frac{k}{\Delta z} \frac{I_2 - I_1}{\langle I_1 \rangle} \quad (2.4)$$

If this approximation is used,  $I_1(x, y)$  does not need to be a focused image: the average intensity is almost independent on the focus setting, so both images can be defocused.

### 2.2.3 Confocal microscopy

Confocal microscopy is the optical analog of scanning electron microscopy. The sample is illuminated with a focused laser beam which scans the surface, and the reflected light is focused on a detector. The technique often employs interferometry to measure the topography of the surface. The fact that a single detector is used for every pixel of a digital image is an advantage over the regular optical microscopy: the latter uses a CCD matrix where the sensitivity slightly varies over different pixels, leading to an increased noise.

## 2.3 Magnetotransport and QHE measurements

Room temperature measurements of resistivity and Hall coefficient do not require any special care: typical epitaxial graphene devices can withstand tens of volts and are not ESD sensitive. For example, we sometimes used a digital multimeter capable of four-point resistance measurement (that is, send current through one pair of contacts and measure voltage between a different pair of contacts), such as Keithley 2000, for both  $R_{xx}$  and  $R_{xy}$ , without any regard to the value of the measurement current. When the purpose of the measurement was preliminary characterization of the devices prior to cooling down, the room-temperature measurements had been performed inside a cryostat using its internal magnet to create the field for the Hall effect. For dedicated room-temperature measurements, we used two permanent neodymium magnets that created field close to 1 tesla in a gap between them. Since the transverse resistance  $R_{xy}$  is not exactly equal to the resistivity component  $\rho_{xy}$ , but is rather a linear combination of a form  $\alpha \cdot \rho_{xx} + \rho_{xy}$ ,  $R_{xy}$  must be measured at least at two values of magnetic field (for example, zero and one finite value), and then the Hall coefficient  $\rho_{xy}/B$  can be calculated as

$$\frac{\rho_{xy}}{B} = \frac{dR_{xy}}{dB}$$

(field dependence of the longitudinal resistivity  $\rho_{xx}$  is weak enough so that it can be ignored).

Low-temperature measurements in the quantum Hall regime were performed in helium flow cryostats with superconducting magnets. The quantum Hall effect raises additional concerns for electrical measurements. First, the measurement current must be limited so as not to exceed the critical current. For this reason, we were using setups with controlled current, such as a current source (Agilent 34420a) with a separate voltmeter or Quantum Design PPMS resistivity option. Typical measurement current was 1  $\mu\text{A}$  per Hall

bar: it is small enough not to break down the QHE in any reasonable device, but the corresponding Hall voltage of approximately 13 mV is big enough to be measured reliably. Also, since measurements of the quantized resistance should be as accurate as possible, the resistance was always measured as an average value for two opposite directions of the current in order to exclude the effect of thermal voltages and other possible sources of voltage offset.

## Chapter 3

# Carrier density control

The task of quantum resistance metrology usually consists in performing measurements on the  $\nu = 2$  quantum Hall plateau, and there is always a certain (generally, material-dependent) optimal value of the carrier density that is required for the best precision. The magnetic field at which the measurement should be performed is essentially fixed: the highest available in the particular experimental setup, because the separation between the Landau levels always increases with the field. The optimal carrier density is the one at which this magnetic field is within the  $\nu = 2$  plateau, and the breakdown current at this field is maximal. This carrier density can be roughly estimated in the following way: the  $\nu = 2$  plateau is reached when the classical Hall resistance becomes equal to the quantized value,

$$\frac{B}{en} \sim \frac{h}{2e^2}$$

which translates into an expression for the carrier density:

$$n \sim \frac{2eB}{h}$$

Thus, for example, the carrier density should be on the level of  $5 \cdot 10^{15} \text{ m}^{-2}$  for measurements at 10 tesla and  $2 \cdot 10^{15} \text{ m}^{-2}$  for 5 tesla. However, achieving the correct carrier density in epitaxial graphene is not straightforward since it is affected both by the substrate [87] and the environment [114–117]. The effect of the substrate can be evaluated by estimating the carrier density immediately after growth using contactless techniques such as Fermi level measurement by angle-resolved photoemission spectroscopy; strong electron doping on the level of  $10^{17} \text{ m}^{-2}$  is typically observed. This substrate-induced doping is then usually countered by hole doping due to adsorption of molecules from

the air [118]: over the course of several days or even weeks, the carrier density slowly drifts towards charge neutrality.

Using this doping by the ambient air to tune the carrier density is possible but problematic because it is such a slow and not completely controllable process. Instead, it would be advantageous to encapsulate graphene by depositing a thin film on top (one that would not cause a decrease of the critical current in the quantum Hall regime due to additional disorder) and achieve the desired carrier density by other means. When a huge (on the level of  $10^{16} \text{ m}^{-2}$  or more) change in doping is needed after the encapsulation, a conventional electrostatic top gate [84, 119, 120] is not an option due to the dielectric breakdown. Also, gate leakage during a QHE measurement would introduce a relative error equal to the ratio of the leakage current to the excitation current. For a typical measurement current of  $100 \mu\text{A}$ , it means that the gate leakage cannot exceed  $100 \text{ fA}$ , which further limits the usability of a gate electrode. This creates a need for other methods of controlling the carrier density. After discussing the limitations of photochemical gating [86], which is the technique that we have previously been using, a new approach involving gating by static charge (also described in paper 3) will be presented.

### 3.1 Limitations of photochemical gating

In the past, photochemical gating [86] has been used to perform QHE measurements on graphene devices by at least two different groups [10, 12]. In those experiments, the carrier density following encapsulation was between  $5 \cdot 10^{15}$  and  $1 \cdot 10^{16} \text{ m}^{-2}$ , which means that it only needed to be reduced by at most  $5 \cdot 10^{15} \text{ m}^{-2}$ . That could be successfully achieved by deep UV illumination.

However, in our subsequently fabricated samples the initial carrier density was often much higher, on the level of  $(3 - 4) \cdot 10^{16} \text{ m}^{-2}$ , so that stronger gating was necessary. Attempts to use photochemical gating on these highly doped samples showed that, depending on the exact spectrum of the UV light, it can be possible to reduce the carrier density from initial  $4 \cdot 10^{16} \text{ m}^{-2}$  close to charge neutrality by a prolonged exposure (such as 30 minutes at a nominal intensity of  $80 \text{ W/m}^2$ ), but at the expense of certain disadvantages. First, the effect was temporary: the carrier density always reverted to some  $2 \cdot 10^{16} \text{ m}^{-2}$  after a few days (in contrast to the “non-volatile” character of weaker gating), so that the exposure would need to be repeated before each measurement. The second problem was that, following the strong illumination, the polymers became mechanically unstable and cracked after a thermal cycle.

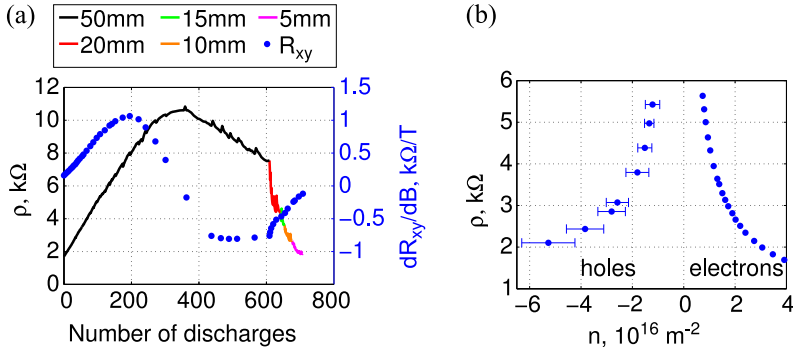


Figure 3.1: Tuning the carrier density in epitaxial graphene by corona discharge

These cracks were never observed in unexposed or weakly exposed polymers. The fact that these cracks can greatly reduce the yield of individual Hall bars made us look for other methods of tuning the carrier density.

## 3.2 Gating by static charge

Dielectric leakage and dielectric breakdown make it impractical to use a gate electrode to control the carrier density in graphene quantum Hall devices. However, these limitations can be circumvented if instead of a gate electrode, the electric field is created by ions forming static charge on the surface of the dielectric layer [121–124]. The reason why this approach can be superior to a metallic gate is because the strongest leakage, and also the breakdown, is thought to happen in a finite set of “weak spots” [124]. In a conventional gate, breakdown through a weak spot would drain the charge from the entire gate electrode. In contrast, a gate formed by static charge on a dielectric would only be discharged locally because the ions cannot easily move in the lateral direction.

We have employed the static charge technique to tune the carrier density in epitaxial graphene using P(MMA-MAA) as the dielectric. This polymer has been chosen because we have previously used it for encapsulation and photochemical gating, resulting in QHE measurements with a high critical current. The static charge on the surface of P(MMA-MAA) was created using Zerostat® anti-static<sup>1</sup> gun which produces pulses of corona discharge. Each pulse caused a decrease of electron doping (or, eventually, an increase of hole

<sup>1</sup>Ironically.

doping) in graphene (Figure 3.1a), followed by a drift of the carrier density in the opposite direction due to the charge leakage. The pulses can be repeated until the charge starts to leak as fast as it can be added, at which point the carrier density saturates. Reducing the distance between the tip that generates the discharge and the sample helps achieving a bigger change of the carrier density because the charge will be added faster.

In our previous experiments with a gate electrode on top of P(MMA-MAA) [86], electric fields up to 180 MV/m could be applied before the dielectric breakdown occurred, resulting in a change of carrier density from  $1.4 \cdot 10^{15} \text{ m}^{-2}$  to  $4 \cdot 10^{14} \text{ m}^{-2}$ . Using the static charge for gating, we were able to change the carrier density from  $4 \cdot 10^{16} \text{ electrons} \cdot \text{m}^{-2}$ , which is on the high side of what is usually observed following the encapsulation, to  $5 \cdot 10^{16} \text{ holes} \cdot \text{m}^{-2}$  (Figure 3.1b). The electric field created by the static charge can then be estimated as

$$E = \frac{e \cdot \Delta n}{r \epsilon \epsilon_0}$$

where  $\Delta n$  is the change of the carrier density,  $\epsilon \sim 4$  is the dielectric constant of P(MMA-MAA),  $e$  and  $\epsilon_0$  are the natural constants, and  $r$  is the gate efficiency described in section 4. Even assuming unity gate efficiency, the maximum electric field in our experiment would be 400 MV/m, and still no clear dielectric breakdown was observed, only fast leakage of the charge. However, reported values of the gate efficiency in epitaxial graphene are typically on the level of 0.1, which means that the actual electric field could be several GV/m.

The largest reported change of carrier density in epitaxial graphene by a metallic top gate with any dielectric was less than  $1 \cdot 10^{16} \text{ m}^{-2}$  [84]. In our experiment, a change of almost  $10^{17} \text{ m}^{-2}$  has been achieved. The charge leakage makes the carrier density constantly drift in ambient conditions; however, the leakage ceases when the sample is cooled down to liquid helium temperatures, and the carrier density will then be stable for at least several days. Thus gating by static charge can be used, and has been used [8] (see also paper 3), to reach the desired doping level for QHE measurements. Doing this is complicated by the fact that the target carrier density is usually in the range of ambipolar transport at room temperature and therefore cannot be directly measured before the cooldown. It is, however, possible to use resistivity as a measure of the carrier density: as long as hole doping is avoided, there is one-to-one correspondence between the two. The room temperature resistivity corresponding to the correct carrier density can be determined by trial and error.

# Chapter 4

## Effect of bilayer patches

Samples of monolayer epitaxial graphene on silicon carbide almost always have inclusions of two or more layers. These multilayer patches have electronic properties drastically different from those of the monolayer, creating potential problems for electronic applications of epitaxial graphene. Since three or more layers are rarely seen in majority-monolayer samples, we will limit ourselves to considering only bilayer patches, the presence of which is unavoidable. We demonstrate that, in agreement with theoretical expectations [125], these patches, regardless of details of their electronic properties, will break down quantum Hall devices if they have a certain “unfortunate” topology. The corresponding experimental findings are presented in paper 1. Later, in section 6.1, we will show that it is still possible to reliably produce QHE devices which are not affected by such bilayer inclusions.

### 4.1 Metallic bilayer

The carrier density in the bilayer patches in epitaxial graphene is usually much higher than that in the monolayer [126, 127], for two reasons. First, Fermi levels in monolayer and bilayer graphene (relative to the Dirac points) are, respectively,

$$\mathcal{E}_{ML} = \hbar v_F \sqrt{\pi n_{ML}}, \quad \mathcal{E}_{BL} = \frac{\pi \hbar^2 n_{BL}}{2m}$$

where  $v_F \approx 10^6$  m/s and  $m \approx 0.033m_e$  ( $m_e$  being the electron mass). This means that if the Fermi levels are equal:  $\mathcal{E}_{ML} = \mathcal{E}_{BL}$ , then  $n_{BL} > n_{ML}$  as long as  $n_{ML} < 4m^2 v_F^2 / \pi \hbar^2 \approx 1 \cdot 10^{17} \text{ m}^{-2}$ . Second, the Fermi level in bilayer patches is usually higher than in the surrounding monolayer [127] (or, in absolute energy

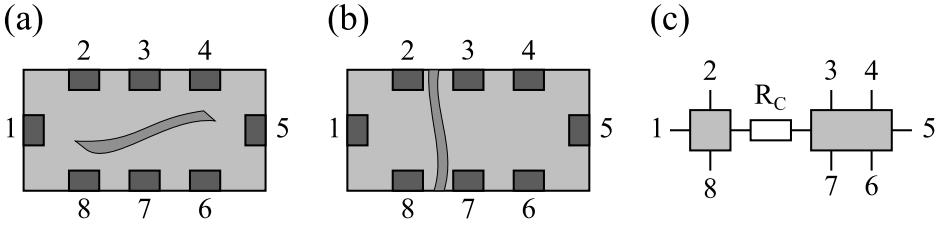


Figure 4.1: Two different topologies for a bilayer patch in a monolayer Hall bar. (a) The patch is totally inside the Hall bar and does not affect the QHE. (b), (c) The patch separates the Hall bar into two parts which will be connected in series when the patch is metallic.

scale, the Fermi levels are aligned but the Dirac point in the bilayer is lower), which further increases the difference in the carrier density.

As a result, when the monolayer has carrier density on the level of  $(2 - 5) \cdot 10^{15} \text{ m}^{-2}$  typical for the measurements of the quantum Hall effect, bilayer is usually highly doped, and thus will most often remain metallic while the monolayer enters the quantum Hall regime. The effect of a bilayer patch will then depend on the topology. For example, if the patch is completely inside the Hall bar (Figure 4.1a), then it will behave as an internal Corbino contact and have no effect other than decreasing the critical current due to decreased effective width of the device. If, however, the patch touches two opposite sides of the Hall bar (Figure 4.1b) then the quantum Hall domain will be separated into two parts connected in series by the patch. The transverse resistances measured using voltage probes 2-8, 3-7 or 4-6 will not be affected, and neither will be longitudinal resistances 3-4 and 7-8, but longitudinal resistances 2-3 and 8-7 will be close to the quantum Hall resistance of the monolayer  $R_H$ : namely,  $R_{3-4} = R_{7-6} = R_H + R_C$  where  $R_C$  is the (relatively small) connection resistance.

We have observed exactly this behavior in a Hall bar deliberately fabricated in such a way that there would be a bilayer patch between two pairs of voltage probes (Figure 4.2a). During the magnetotransport measurements (Figure 4.2b), the monolayer with carrier density  $5 \cdot 10^{15} \text{ m}^{-2}$  entered the quantum Hall regime above 8 tesla, so that transverse resistance measured using contacts 4 and 6 became quantized at  $h/2e^2$ , and longitudinal resistance between contacts 7 and 6 vanished. At the same time, longitudinal resistance between contacts 8 and 7,  $R_{8-7}$ , was close to the quantized value of  $h/2e^2$ , as expected. The fact that  $R_{8-7}$  was actually smaller than  $h/2e^2$ , which corresponds to apparently negative  $R_C$ , can be attributed to Hall effect in the bilayer. In-

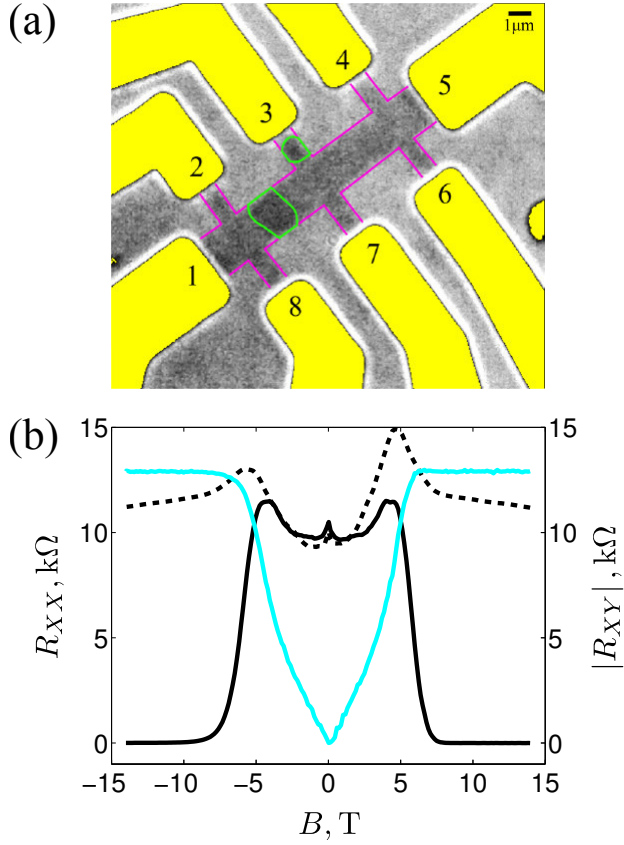


Figure 4.2: Measurement on a Hall bar with a metallic bilayer patch cutting across. (a) An optical transmission micrograph of the device with graphically superimposed layout; dark gray regions are bilayers (outlined in light green) and light gray regions are monolayers. (b) The corresponding transverse resistance (light blue) and longitudinal resistance (black) plots measured from contacts 4-6 and 7-6, respectively, in the entirely monolayer region at  $T = 4$  K. The black, dashed plot is the (nominally) longitudinal resistance measured from contacts 8-7 separated by a bilayer patch.

deed, if the bilayer were in the quantum Hall regime then, according to the theory described in section 1.7.3,  $R_{8-7}$  would be equal to  $h/2e^2 - |\rho_{xy}|$  where  $\rho_{xy}$  is the transverse resistivity of the bilayer. Assuming that a similar formula is true for metallic bilayer with transverse resistivity  $\rho_{xy} = B/en'$  (where  $n'$  is the carrier density in the bilayer), and that finite longitudinal resistivity of the bilayer does not play a big role, we obtain

$$R_{8-7}(B) \approx \frac{h}{2e^2} - \frac{|B|}{en'}$$

which is in agreement with the experimental data at high fields.

## 4.2 Insulating bilayer

As discussed in section 1.6 and chapter 3, epitaxial graphene has an intrinsic bottom gate inside the substrate with an uncontrollable amount of positive charge on it, which causes heavy electron doping of graphene. Low carrier density can be obtained by putting negative charge on a top gate, creating a double-gate configuration similar to the one used in some experiments on flakes [18]. Two gates of opposite polarity will counteract each other in terms of the change in carrier density, but electric fields that they create will add up, which will cause a sizable band gap in the bilayer to appear, as discussed in section 1.1. Therefore, the bilayer areas of epitaxial graphene should become insulating when the effect of the top gate is strong enough both to create the band gap and to drive the Fermi level into this gap.

We have observed insulating behavior of the bilayer in another sample where the bilayer patches did not cross the device completely, forming a constriction in the monolayer instead (Figure 4.3b). There was no explicit top gate, but atmospheric doping [118] was performing a similar role instead. Low-temperature magnetotransport measurements (Figure 4.3c) show carrier density  $5 \cdot 10^{14} \text{ m}^{-2}$  in the monolayer, much lower than in the previous device, and longitudinal resistance of some 160 k $\Omega$  at zero field. If the sample properties were uniform then with the length-to-width ratio of 6 this would correspond to resistivity of 27 k $\Omega$ . To compare, maximum resistivity observed in the vast majority of graphene flakes [31], as well as in our epitaxial graphene sample from section 3.2, is on the level of 10 k $\Omega$  or less. Therefore, the unusually high average resistivity in the device points towards high resistivity of the bilayer which is a signature of the insulating state. If we assume the bilayer to be completely insulating, the effective length-to-width ratio will be approximately 15 due to the presence of constrictions, resulting in resistivity of 11 k $\Omega$  which is close to the usual values observed in graphene.

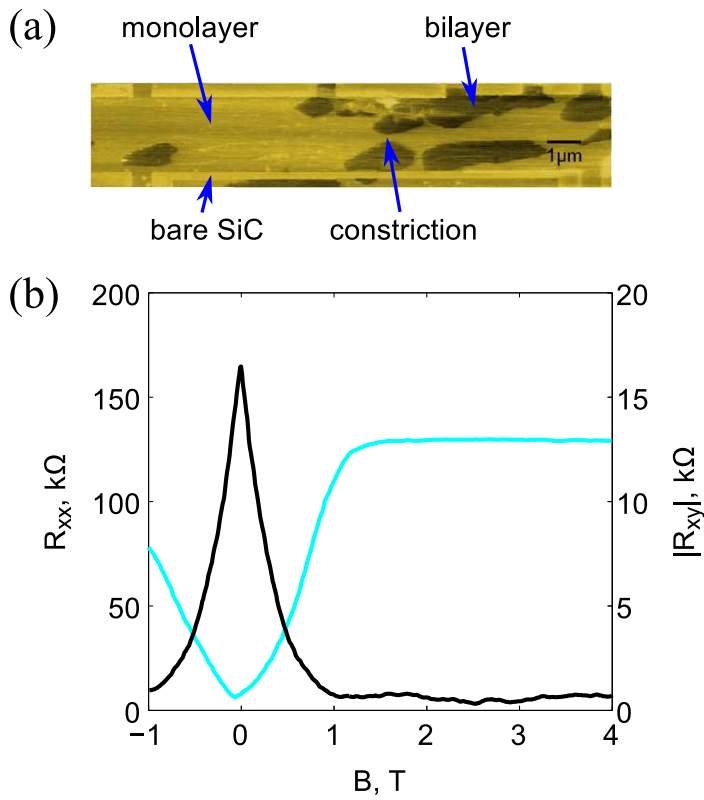


Figure 4.3: A device demonstrating insulating behavior of the bilayer. (a) Scanning Kelvin probe image of the device: the dark areas are the bilayer patches, and the lightest areas correspond to bare silicon carbide where the graphene has been etched away. (b) Magnetotransport measurements:  $R_{xy}$  measured using the left pair of voltage probes and  $R_{xx}$  with the bottom pair.

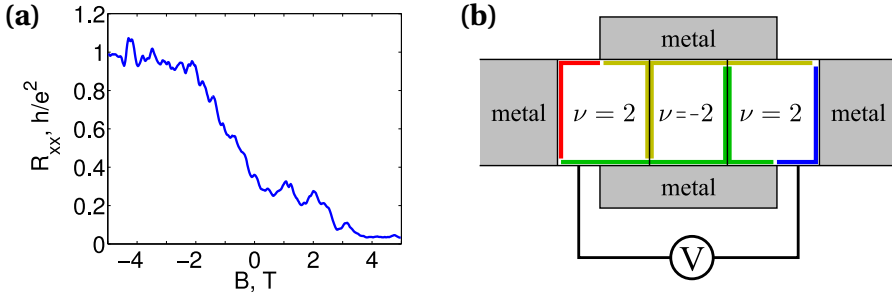


Figure 4.4: (a) Gate dependence of the total longitudinal resistance with a local gate above the constriction in the monolayer. (b) Potential distribution in an n-p-n junction with metallic bilayer on the sides, a model which fails to reproduce the measurement result.

More evidence for insulating behavior of the bilayer was obtained by placing an AFM tip above the constriction in the monolayer and applying voltage to the tip, while at the same time measuring longitudinal resistance across the constriction under quantum Hall conditions (Figure 4.4a). The tip acted as a local top gate, changing the carrier density in the constriction. At positive gate voltages, the longitudinal resistance was decreasing towards zero, meaning that the QHE in the constriction without the gate voltage was not well-developed, probably due to spatial variations of the carrier density. When positive gate voltage was applied to the local gate, the constriction became homogeneously electron-doped, causing better resistance quantization. At negative gate voltages, the longitudinal resistance saturated at a value close to  $h/e^2$ . The fact that the resistance had saturated suggests that the constriction became hole doped and entered quantum Hall regime with filling factor -2, forming an n-p-n junction.

If the bilayer was insulating then, according to section 1.7.3, the longitudinal resistance would be equal to  $h/e^2$  [98], in agreement with the experiment. If, however, the bilayer was metallic with low resistivity, electrostatic simulations reveal a configuration of equipotential lines shown in Figure 4.4b. By using resistivity tensor (1.10) and the current conservation law, it is then possible to calculate that the longitudinal resistance between the n-doped domains will be only  $h/3e^2$  (somewhat more if finite resistivity of the bilayer is taken into account). Thus we conclude that insulating (or, at least, high-resistive) behavior of the bilayer has been observed.

If a perfectly insulating bilayer patch crosses a Hall bar as in Figure 4.1b,

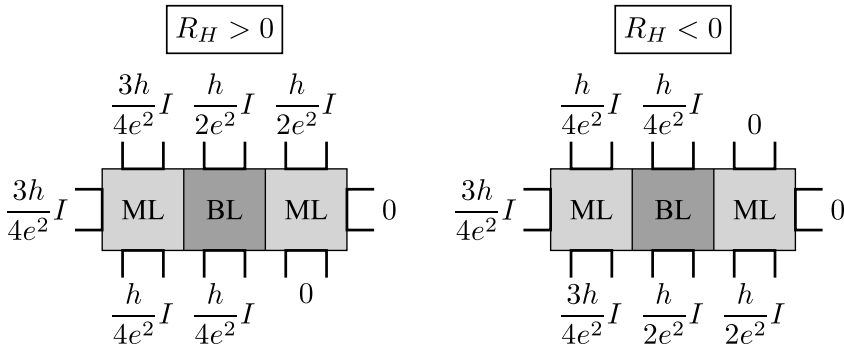


Figure 4.5: Potential distribution across a bilayer patch which is in the  $\nu = 4$  quantum Hall state in a monolayer  $\nu = 2$  quantum Hall device, in the units of the source-drain current

the Hall bar will be split into two disconnected parts. If it is a single Hall bar, the measurements can be performed on each part separately. On the other hand, if this happens to an element of the quantum Hall array, the array will be ruined. Without the connection resistances, the net resistance of the array would still be quantized, only at a slightly different rational fraction of  $h/e^2$ . However, such modification of the array schematics would invalidate the equations (1.18), causing decreased precision due to the increased effect of finite connection resistances.

### 4.3 Bilayer in the quantum Hall regime

The last possibility is that while the monolayer is in the  $\nu = 2$  quantum Hall state, the bilayer is in the quantum Hall regime as well. However, the bilayer normally doesn't have the  $\nu = 2$  state, so its filling factor will be different, for example,  $\nu = 4$ . According to the theory (section 1.7.3), potential distribution across a  $\nu = 2$  Hall bar with a  $\nu = 4$  bilayer patch in the middle will look as shown in Figure 4.5. The device will have wrong two-point resistance ( $3h/4e^2$  instead of  $h/2e^2$ ), and there will be longitudinal resistance of  $h/4e^2$  between the two monolayer parts. Transverse resistance between the different monolayer parts (voltage probes 2 and 6 or 4 and 8) will also be wrong:  $h/4e^2$  or  $3h/4e^2$  instead of  $h/2e^2$ . All resistances will still be quantized, but even if this quantization were exact, the breakdown current should be much smaller than in a pure monolayer device due to the bilayer being involved. As far as quantum Hall arrays are concerned, if such wrong quantization occurs in one of

the array elements, the effect of finite connection resistances will fail to get reduced because the equations (1.18) will no longer be valid, resulting in a decreased precision. Therefore, bilayer patches will break QHE devices even if the patches are in the quantum Hall regime.

#### **4.4 Summary**

While monolayer graphene is in the quantum Hall regime, the bilayer can be either metallic, insulating or in the quantum Hall regime with a different filling factor. Only the first two types of behavior have been observed in our experiments. However, regardless of which situation is realised, if a bilayer patch connects together two contacts of a quantum Hall device, or separates some contacts from the others, the affected contacts will be defective. This is less of a problem for single devices where it can be enough to choose five working contacts for a successful measurement. On the other hand, for quantum Hall arrays where every contact in every individual device must be working, it is important that all bilayer patches have such topology that they do not affect the QHE.

## Chapter 5

# Morphology characterization

As discussed in chapter 4, multi-layer patches which are present in epitaxial graphene can either destroy or preserve the quantum Hall effect, depending on the topology. The shape of these patches is closely related to geometry of steps on the surface of the substrate. Therefore, characterization of these morphology features is an important step in determining whether the material can be used for metrological applications.

Such characterization can be done by a variety of methods, but the ones that are most commonly used have significant disadvantages. Atomic force microscopy and other scanning probe techniques [128, 129] resolve the steps and the multilayer patches with an excellent resolution; however, imaging large areas this way takes very long time. The areas with different number of layers can also be identified by scanning electron microscopy [130, 131] or low-energy electron microscopy [132–134], but it leads to electron beam-induced contamination, and can be somewhat slow as well due to the need for high vacuum.

This chapter demonstrates that imaging of the steps and the bilayer patches can be done by optical microscopy, as described in paper 2. The optical techniques have an advantage of being simple, completely non-invasive, and very fast at the same time; and their lateral resolution, although limited by the wavelength of visible light, is sufficient for many practical purposes.

### 5.1 Optical imaging of the bilayer domains

Ever since the discovery of exfoliated graphene, it has been known that the optical contrast between a bare substrate and a single graphene layer, as well as between one and two or more graphene layers, can in principle be detected

by visual inspection in an optical microscope. However, this could only be done on substrates where the contrast can be enhanced by thin film interference, such as silicon with a layer of oxide on top. For epitaxial graphene, this is not an option because high quality graphene has only been produced on bulk silicon carbide, not thin-film-deposited one.

The optical contrast for epitaxial graphene is readily calculated using formulas (1.19) from section 1.8. If immersion microscopy is not used, the refraction indices are  $n_1 = 1$  and  $n_2 \approx 2.65$  or vice versa. This translates into the contrast of 1.3% per graphene layer in transmission and 1.5% per layer in reflection from outside the substrate, both of which are too low to be detected by the eye. For reflection from inside the substrate, the contrast is 4% per layer, but this cannot be used for imaging because the substrate would then prevent from obtaining a sharp image. Immersion microscopy with  $n_1 \approx 1.5$  could increase the reflection contrast to 3% per layer, but it is less straightforward than the “normal” microscopy as it requires special objective lenses as well as exposing graphene to a liquid, and 3% contrast is still hardly enough to be clearly seen by the eye. As a result, for a long time scanning probe microscopy and (usually low-energy) electron microscopy were the only techniques used for imaging the bilayer patches on epitaxial graphene.

However, optical contrast on the level of 1% can, in fact, be detected if digital imaging with subsequent post-processing is used, as long as the signal to noise ratio is sufficiently high. The contrast can be enhanced by an arbitrary factor  $N$  using a digital filter such as  $I' = I_{max}/2 + N \cdot (I - \langle I \rangle)$  where  $I$  is the intensity at each pixel,  $\langle I \rangle$  is the average intensity, and  $I_{max}/2$  is the middle of the dynamic range. This simple procedure, known as contrast stretching, can be done in real time in the imaging software, making optical microscopy a suitable tool for determining amount, size and shape of the bilayer patches across the entire substrate.

Examples of images are shown in Figure 5.1. To get the best results from the regular optical microscope, in addition to time averaging and subtracting polynomial background, a defocused image without any visible features has been divided out in order to cancel the static (non-time-dependent) noise of the CCD matrix (Figure 5.1f,g). The latter procedure is not required for a confocal microscope (Figure 5.1h) because it uses the same detector for every pixel of the image. However, even without any time-consuming procedures of averaging, cancelling the static noise or background subtraction, the quality of the images from a regular optical microscope (Figure 5.1e) is sufficient for a visual inspection.

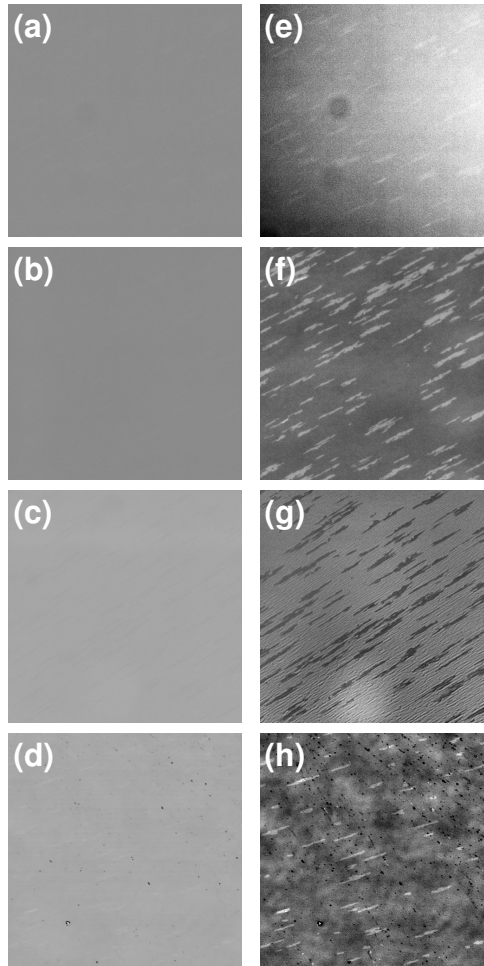


Figure 5.1: (a)-(c) Raw images from an optical microscope: (a) reflection, no averaging or additional post-processing; (b), (c) reflection and transmission, with 128x averaging, non-time-dependent noise being divided out, and polynomial background subtraction. (d) Raw image from the confocal microscope with only time averaging and polynomial background subtraction. The bilayer patches can hardly be seen on the raw images due to small contrast. (e)-(h) The same images after contrast stretching.  $1\ \mu\text{m}$  wide patches are clearly visible. Additionally,  $1\ \text{nm}$  high steps are seen on a part of the transmission image (g) due to defocusing caused by tilt of the substrate.

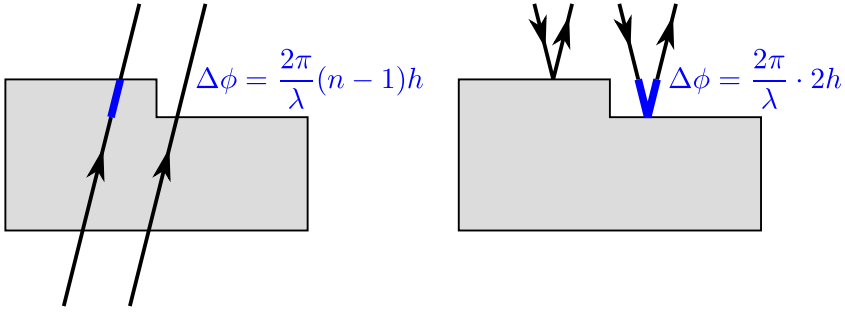


Figure 5.2: Transmission and reflection microscopy on epitaxial graphene. Sharp gradients of the phase of transmitted or reflected light are found at the steps.

## 5.2 Optical imaging of the steps

Nanometer-high steps on the surface of silicon carbide can also be detected optically. As seen in Figure 5.2, light waves reflected off different points on the surface, or transmitted through different places, accumulate different phase due to topography of the surface. A step on the surface creates a sharp gradient of the phase. The amplitude of reflected or transmitted light, however, is not affected: being at most 10 nanometers high, the steps do not cause any noticeable scattering of the light, and thus can only be seen using phase imaging methods.

We demonstrate this by using differential interference contrast (DIC) in reflection mode (Figure 5.3a) and transport of intensity (TI) in transmission mode (Figure 5.3c). DIC provides qualitative information about phase gradients (or, in our case, height gradients), so that the steps are seen as bright lines in Figure 5.3a. For the TI technique, we use the equation (2.4) to calculate the topography. Taking into account the relation between the topography and the phase  $\phi = const + k(n-1)h$ , the equation becomes

$$\nabla^2 h = -\frac{1}{(n-1)\Delta z} \frac{I_2 - I_1}{\langle I_1 \rangle} \quad (5.1)$$

When combined with contrast stretching, both DIC and TI techniques could resolve steps down to 1.5 nanometers in height (limited by the noise), as demonstrated by comparing the optical images to AFM images of the same areas (Figure 5.3b,d). Thus, not only the bilayer patches, but also all but the lowest steps can be optically imaged in real time.

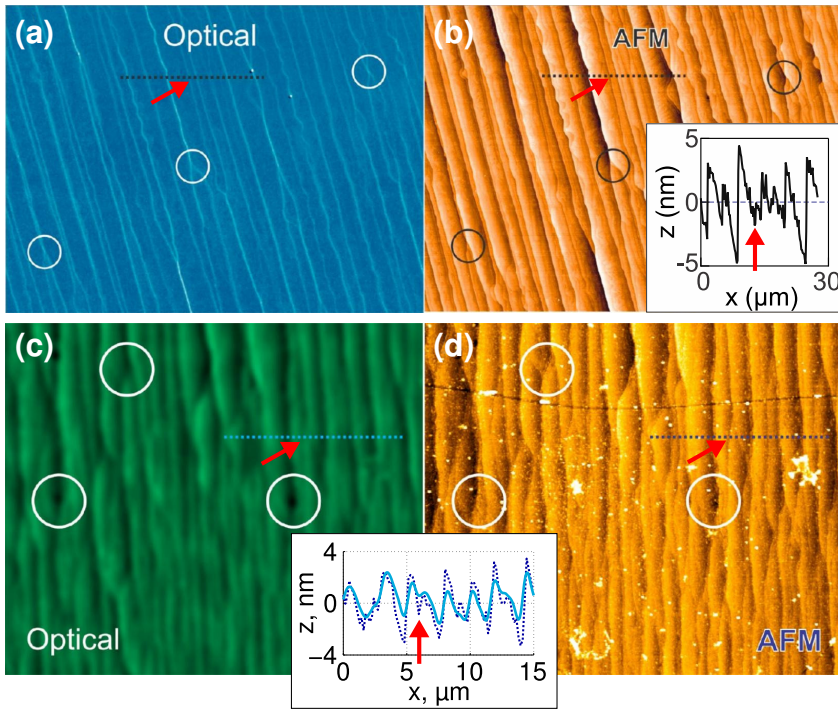


Figure 5.3: Observation of steps at the surface of silicon carbide by optical phase imaging: DIC (a) and TI (c). The latter image shows topography calculated by solving the equation (5.1). AFM topography images of the same areas (b, d) are shown for comparison. Insets show traces from topography images. Both optical techniques are capable of detecting 1.5 nanometer high steps which are highlighted by arrows.



## Chapter 6

# Quantum Hall arrays

The motivation behind making quantum Hall arrays, in particular ones employing parallel connection of Hall bars, is twofold. First, the task of measuring electric currents and resistances with high accuracy creates a need for high-precision resistors. These precision resistors are essentially variable resistors that are set to the correct value by calibrating against a quantum Hall device (often indirectly, through a chain of other resistors). Calibration of a resistor with the value, for instance, on the order of one ohm or less becomes technically easier and more precise if it is performed against a low-resistance array rather than a single Hall bar with resistance of 13 k $\Omega$ . The second advantage of such array is that it can sustain larger current than a single device of the same physical size. For example, an array of one hundred 30 micron wide Hall bars can occupy the same area as a single 600 micron wide Hall bar. If the critical current in one array element is  $I$  then the huge single Hall bar can sustain  $20I$ , compared to  $100I$  in the array.

Fabricating arrays on epitaxial graphene brings additional advantages over the traditional gallium arsenide, such as high critical current density and the ability to operate at higher temperature and lower fields. Also, due to charge transfer to the substrate, much weaker magnetic field dependence of the critical current has been observed in epitaxial graphene, as compared to gallium arsenide (Figure 1.12). This means that variations of the carrier density between individual Hall bars are less likely to decrease the critical current in the array: at a fixed magnetic field, some Hall bars will have suboptimal critical current if they have a different carrier density, but this effect will be less prominent in graphene.

In this chapter, we describe quantum Hall arrays consisting of 100 Hall bars connected in parallel, fabricated on epitaxial graphene, as reported in

paper 4. We show that on a particular class of substrates with a certain geometry of bilayer patches, it is possible to completely avoid the defects related to these patches by a correct design of the individual Hall bars. We use circuit simulation to evaluate various corrections to the Hall resistance of the array. In particular, we demonstrate that a single occurrence of any of the considered bilayer-related defects will prevent from achieving metrological precision. Finally, we present measurements on four fabricated arrays, identify the remaining problems and discuss the prospects of making metrologically accurate arrays on epitaxial graphene.

## 6.1 Device design

### 6.1.1 Hall bars and the choice of the substrate

Hall bars with 8 contacts were chosen, so that quadruple-parallel connection ( $K = 4$  in equations 1.18) is possible. The design of individual Hall bars was adapted to the morphology of the bilayer patches on the particular substrate, so that the patches would not affect the QHE. This is only possible if the bilayer areas are sufficiently small and sparse, so suitable substrates must be selected by observing the geometry of the bilayer patches, for example, by optical microscopy (Figure 5.1e is an example of an image that can be obtained in real time, and the image quality is clearly sufficient). An additional design constraint was keeping the Hall bars as small as possible (while still larger than the patches): this would allow fabricating many arrays on the same substrate, and possibly avoid problems with inhomogeneity of the carrier density over large areas.

The best substrates available to us had bilayer patches in the shape of 1 micron wide, up to 20 micron long stripes all oriented in the same direction, as shown in Figure 6.1. The shape of a Hall bar in our array devices was chosen to be a 40 microns long rectangle, oriented along the patches (Figure 6.1a). With this design, the patches cannot completely cross the Hall bar from one side to another. It is still possible that a bilayer stripe will connect two contacts on the side, but, as will be demonstrated in section 6.2.3, such defect would have much smaller effect on the net resistance of the array. This problem can also be avoided by further design modifications (Figure 6.1b): the Hall bar can be made longer so that the distance between the contacts on the side is increased to 20 microns, and  $20^\circ$  rotation of the Hall bars with respect to the patches would further decrease the chances of the defect occurring.

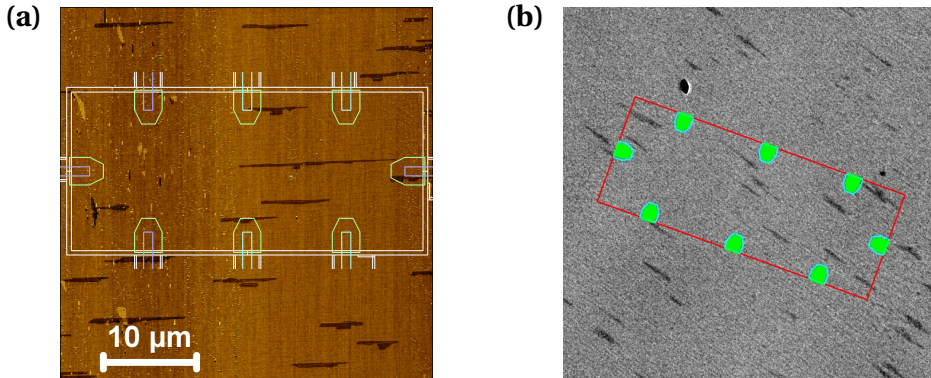


Figure 6.1: (a) A typical AFM phase image of the graphene substrate with the drawing of a Hall bar superimposed. Dark areas are the bilayer patches. (b) Optical transmission micrograph of a similar substrate with a modified design of a Hall bar, which avoids the possibility of two contacts on the side being connected by a bilayer patch.

### 6.1.2 Interconnections

Quadruple-parallel connection of 100 Hall bars has been implemented as a periodic pattern, a “unit cell” of which is shown in Figure 6.2b. The pattern was computer-generated by an AutoLisp script which is available in the electronic version of this thesis. The wires (gold, made by lift-off deposition) cannot be arranged in a single layer, so a dielectric film (100 nm of silicon dioxide) had to be deposited in the intersections where no electric contact was needed. The width (1  $\mu\text{m}$ ) and thickness (50 nm for the bottom layer, 150 nm for the top layer) of the wires were chosen so that their resistance would be sufficiently low in order for its effect on the resistance of the array (equations 1.18) to be within  $10^{-8}$ . The role of the redundant arrangement of the wires is twofold: first, a single discontinuity in some wire will not affect the device; second, as shown below in section 6.2.2, the effect of connection resistance on the Hall voltage measured between contacts 3 and 7 will be significantly reduced. Using this pair of contacts has advantages compared to the  $j = 4$  contacts (4 and 8 or 2 and 6): they give the same precision for both directions of magnetic field, they are directly opposite to each other and thus less affected by possible residual longitudinal resistivity [135], and also they are the furthest away from the source and drain contacts where the heat dissipation happens, which makes them less sensitive to the breakdown of the QHE at high currents.

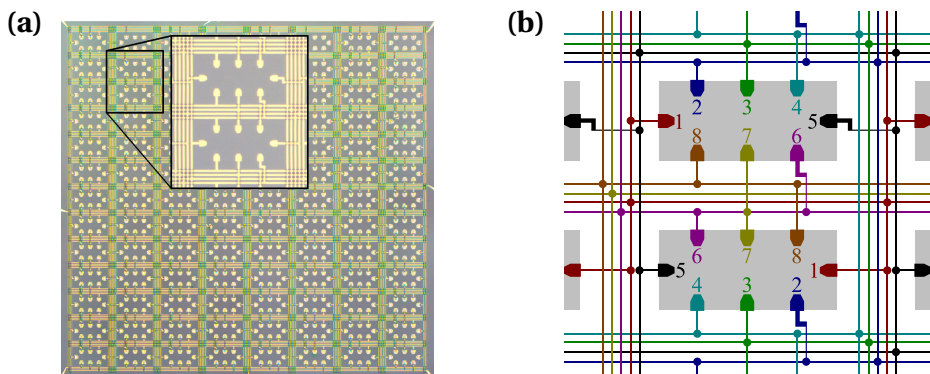


Figure 6.2: (a) A micrograph of an array of 100 Hall bars. The Hall bars are organized into a  $13 \times 8$  grid with four of them not connected. (b) A part of the schematics of the array corresponding to the inset of (a). The interconnecting wires are arranged with a significant redundancy.

## 6.2 Circuit simulations

### 6.2.1 The method

The method we used for simulating quantum Hall circuits was somewhat similar to the one used for resistive networks. A resistive network is a collection of nodes connected by resistors, and potentials at each node and currents through each resistor are to be found. Kirchhoff's current law for every node except the drain and possibly source(s), special equations for the source and drain nodes, and Ohm's law for each resistor provide a system of the required amount of linear equations.

A quantum Hall circuit contains also a number of QHE domains, and there are two types of resistive links: ones connecting two nodes, and ones connecting a node and a QHE domain. In our model, one node is the source where a fixed current enters the circuit, and one node is the drain. Potentials at each node (not in the QHE domains) and currents through each resistor are the unknowns. The equations for all the nodes and the links between the nodes are the same as those describing usual resistive network: Kirchhoff's current law for every node except the source and the drain, modified Kirchhoff's law for the source (the sum of currents is equal to the source current rather than zero), zero potential at the drain, and Ohm's law for each link. For a link between a node and a QHE domain, the equation is instead a combination of (1.16) and Ohm's law:

$$V - R_C I - (V' - R'_C I') = \begin{cases} R_H I & , R_H > 0 \\ R_H I' & , R_H < 0 \end{cases}$$

where  $V$  is the potential at the end of the link,  $R_C$  is the resistance of the link, and  $I$  is the current through the link (positive if directed into the quantum Hall domain);  $V'$ ,  $R'_C$  and  $I'$  are similar quantities for the next (in the clockwise direction) link in the same QHE domain.

The scripts performing these simulations are available in the electronic version of this thesis.

### 6.2.2 Effect of connection resistance

Corrections to the Hall resistance for different pairs of voltage probes of a quantum Hall array with quadruple-parallel connection, as per the general theory (equation 1.18), are shown in table 6.1, column “theory”. To get a better quantitative estimate, we have performed numeric simulations of the circuit (the one shown in Figure 6.2) with different values of wire resistivity, and the results are summarized in the column “simulation” of table 6.1. Here,  $\rho$  is resistance per unit of length of the vertical wires in the units of  $\Omega/\mu\text{m}$ , and resistance of the horizontal wires was assumed to be three times larger since in the actual device they were three times as thin.

The exponent extracted from the simulations is the same as the one deduced from the general theory everywhere except for the contact pair 3-7 where the simulations predict higher precision (third power instead of second), which is a special feature of the particular arrangement of the interconnecting wires that we are using. According to the table, the highest-precision contact pairs (4-8 or 2-6) give  $10^{-8}$  precision for  $\rho = 0.05 \Omega/\mu\text{m}$  at the correct direction of the magnetic field. The contact pair 3-7 is expected to give  $3 \cdot 10^{-7}$  precision for both directions of the field with the same wire resistance.

### 6.2.3 Bilayer-related defects

We have also used numeric simulations to evaluate the effect of different types of bilayer-related defects in the Hall bars, assuming that the bilayer patches are metallic. For example, if a bilayer patch is longer than the Hall bar, it is possible that it will cut along the device, touching both current leads, as shown in Figure 6.3a. We expect that this can be modeled as two separate quantum Hall domains connected in parallel with a resistive network in between, as shown in Figure 6.3. Circuit simulations show that one such split Hall bar can reduce the net resistance of the array by about 0.5%.

voltage probes	theory		simulation	
	$B > 0$	$B < 0$	$B > 0$	$B < 0$
2-8	$O(\rho^2)$	$O(\rho^2)$	$(0.20\rho)^2$	$(0.19\rho)^2$
3-7	$O(\rho^2)$	$O(\rho^2)$	$(0.14\rho)^3$	$(0.13\rho)^3$
4-6	$O(\rho^2)$	$O(\rho^2)$	$(0.22\rho)^2$	$(0.22\rho)^2$
3-8	$O(\rho^3)$	$O(\rho^2)$	$(0.05\rho)^3$	$(0.19\rho)^2$
4-7	$O(\rho^3)$	$O(\rho^2)$	$(0.13\rho)^3$	$(0.22\rho)^2$
2-7	$O(\rho^2)$	$O(\rho^3)$	$(0.20\rho)^2$	$(0.13\rho)^3$
3-6	$O(\rho^2)$	$O(\rho^3)$	$(0.22\rho)^2$	$(0.05\rho)^3$
4-8	$O(\rho^4)$	$O(\rho^2)$	$(0.20\rho)^4$	$(0.29\rho)^2$
2-6	$O(\rho^2)$	$O(\rho^4)$	$(0.29\rho)^2$	$(0.20\rho)^4$

Table 6.1: The effect of finite connection resistance on the Hall resistance of the array for different pairs of voltage probes, according to the theory (equations 1.18) and to the numeric simulations.  $\rho$  is the specific resistance of the vertical wires in  $\Omega/\mu\text{m}$ .

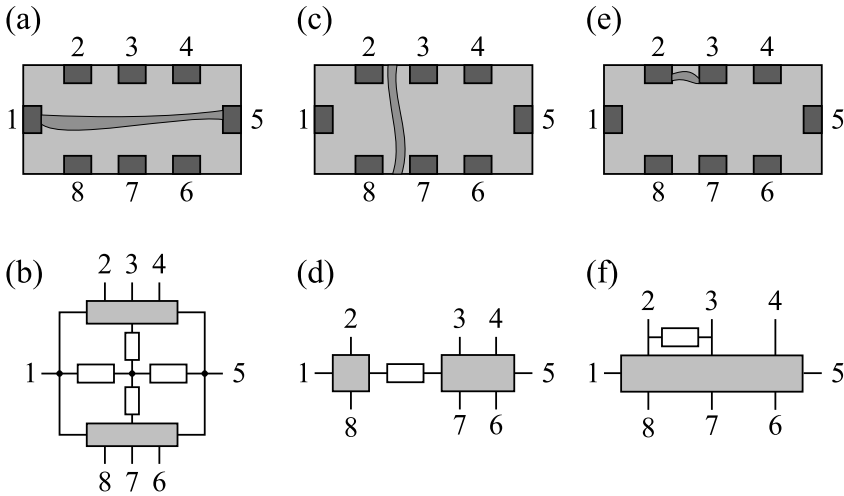


Figure 6.3: Defects related to bilayer patches. (a), (b) A Hall bar with a bilayer region along the channel and its equivalent circuit. (c), (d) A Hall bar with a bilayer region across the channel and its equivalent circuit. (e), (f) A Hall bar with a bilayer region at the side and its equivalent circuit.

If a patch of bilayer connects two opposite sides of a Hall bar as shown in Figure 6.3c, this will be equivalent to series connection of two Hall bars (Figure 6.3d), as discussed in section 4.1. According to the numeric simulations, one such defect in an array of 100 Hall bars will cause a  $10^{-5}$  relative deviation in resistance, and two defects can cause a deviation of  $10^{-4}$ . Finally, a shorter patch can connect two contacts on a side (Figure 6.3e, f), but, since the potential difference between the affected contacts is small, even 50 randomly placed defects of this type will only cause  $1 \cdot 10^{-5}$  relative deviation in the net resistance of the array. All these results, together with the calculated effect of high-resistance contacts, are shown in table 6.2. To summarize, any of these defects makes it impossible to reach precision better than  $10^{-7}$ .

#### 6.2.4 Leakage of the insulation

A practical way of measuring leakage in the dielectric that separates intersecting wires in the array is to fabricate the interconnecting wires without the Hall bars and measure two-point resistances between various pairs of contacts. The resistances between all pairs of contacts are likely to have approximately the same value,  $R_I$ . In this case, the leakage resistance can be modeled by introducing a resistor  $4R_I$  between every pair of contacts in the array, which

Defect type	$\Delta R_{xy}/R_{xy}$
one bilayer patch cutting along a Hall bar	0.5%
one bilayer patch cutting across a Hall bar	$10^{-5}$
two bilayer patches cutting across a Hall bar	$10^{-4}$
one bilayer patch connecting contacts on the side	$10^{-7}$
10-50 bilayer patches connecting contacts on the side	$10^{-5}$
one 5 k $\Omega$ contact	$10^{-7}$
ten 3-5 k $\Omega$ contacts	$10^{-6}$

Table 6.2: Effect of various structural defects on the net resistance of the array of 100 Hall bars.

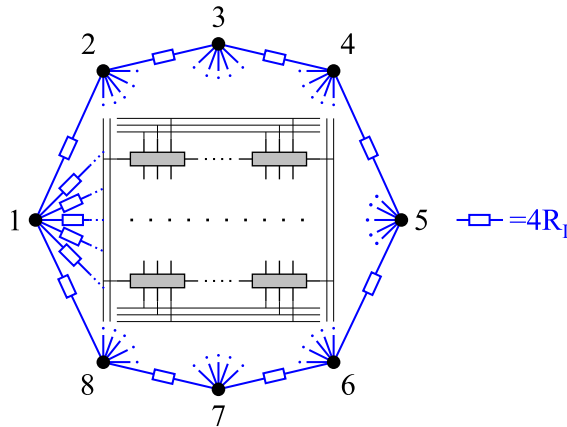


Figure 6.4: Modeling insulation leakage in a quantum Hall array.

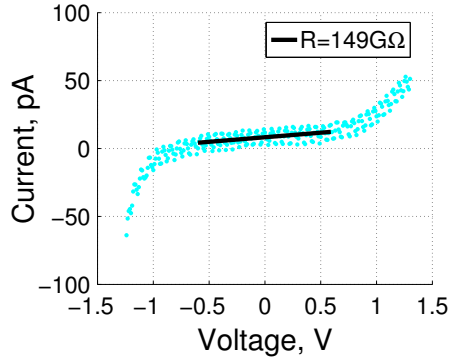


Figure 6.5: Measurement of the insulation leakage in an array of 100 Hall bars.

will give the correct two-point leakage resistance. Numeric simulation of the full circuit then shows that the relative correction to the Hall resistance of the array  $R_{xy}$  is approximately  $\Delta R_{xy}/R_{xy} \approx 4R_{xy}/R_I$ . For example, for an array of 100 Hall bars with  $R_{xy} \approx 129 \Omega$ ,  $10^{-8}$  precision can be reached when  $R_I > 50 \text{ G}\Omega$ .

## 6.3 Measurements on the arrays

### 6.3.1 Connection resistance and leakage

To measure resistance of the interconnects in the array, wires of a similar geometry (1 micron wide, 150 nm thick, up to 300 micron long) were separately fabricated using the same recipe. The resistance of these wires was measured at the temperature of 2 kelvin, giving one-dimensional resistivity of  $0.065 \Omega/\mu\text{m}$ . The resistivity of 50 nm thick wires was estimated as being three times higher, or  $0.2 \Omega/\mu\text{m}$ . According to section 6.2.2, this translates to maximum precision of  $3 \cdot 10^{-8}$ , or  $10^{-6}$  precision if the central pair of voltage probes is used.

In order to measure leakage of the insulation at the intersections of the interconnecting wires, a structure identical to the array of 100 Hall bars was fabricated on a bare insulating substrate (oxidized silicon). Resistance between two terminals of this device was measured to be  $150 \text{ G}\Omega$  at room temperature for voltages below 0.5 V (Figure 6.5), which we assume as a lower-bound estimate for the insulation resistance  $R_I$ . According to section 6.2.4, the relative contribution of the leakage to the resistance of the array of 100 Hall bars would then be at most on the level of  $3 \cdot 10^{-9}$ . In fact, the effect of the leakage at low temperatures should be even smaller.

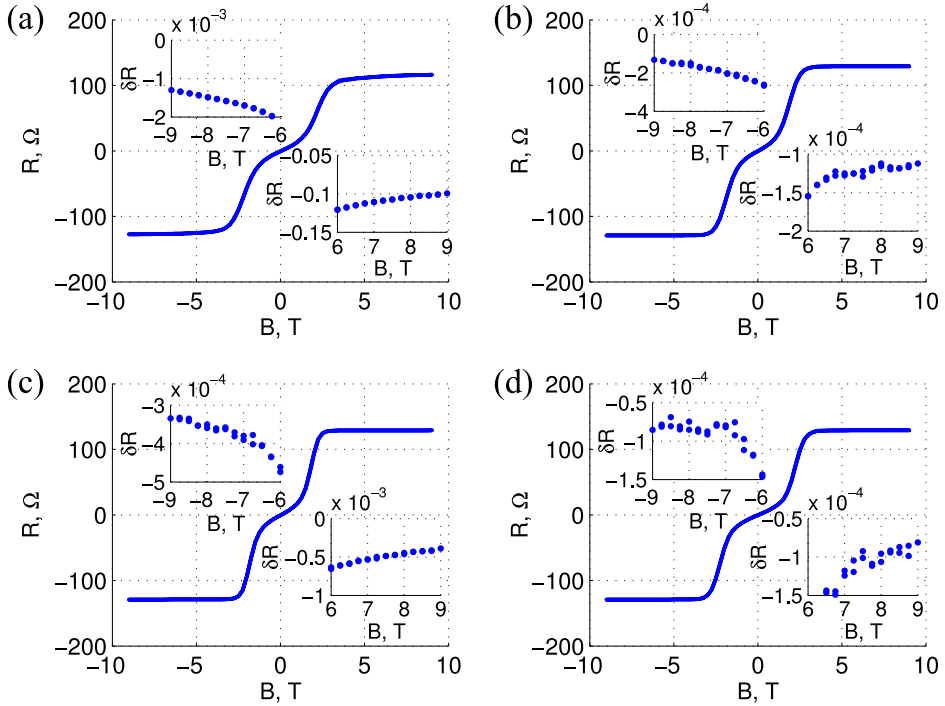


Figure 6.6: Measurements of  $R_{xy}$  vs. magnetic field in the quantum Hall arrays. (a) - (d) correspond to devices A - D. Insets show deviation from the ideal value  $R_K/200$ ,  $\delta R = 200 \cdot R/R_K - 1$  for  $B > 0$  and  $-200 \cdot R/R_K$  for  $B < 0$ , at high fields where the quantum Hall plateaus were expected to be fully developed. The only plateau that is actually fully developed is the one for device D at negative fields.

### 6.3.2 QHE measurements

Measurements of the quantum Hall resistance were performed on arrays of 100 Hall bars, as well as on single Hall bars fabricated on the same substrate. Before the measurement, photochemical gating was used to reduce the carrier density from  $3 \cdot 10^{16} \text{ m}^{-2}$  to  $4 \cdot 10^{15} \text{ m}^{-2}$ , as confirmed by Hall measurements at low fields. For the arrays, the Hall voltage was measured between contacts 3 and 7.

Results of the measurement on four arrays of 100 Hall bars (devices A, B, C and D) in magnetic fields up to 9 tesla are shown in Figure 6.6. The four devices showed different relative deviations of  $R_{xy}$  from the ideal value of  $R_K/200 \approx 129.064 \Omega$ , which are shown in the insets of Figure 6.6 and summa-

Device	$-200 \cdot R_{xy}/R_K - 1, B < 0$	$200 \cdot R_{xy}/R_K - 1, B > 0$
A	$-1.3 \cdot 10^{-2}$	$-0.1$
B	$-1.5 \cdot 10^{-4}$	$-1.1 \cdot 10^{-4}$
C	$-3.3 \cdot 10^{-4}$	$-4 \cdot 10^{-4}$
D	$-8 \cdot 10^{-5}$	$-9 \cdot 10^{-5}$

Table 6.3: Relative deviations between the measured Hall resistance of the four arrays and the ideal value  $R_K/200$  at the highest magnetic fields

ized in Table 6.3. Device A was clearly defective, with 10% deviation of  $R_{xy}$  for positive field and 1% for negative field. Devices B and C performed better, showing deviations on the level of  $1 \cdot 10^{-4}$  and  $4 \cdot 10^{-4}$ , respectively, but the plateaus were not fully developed for any direction of the magnetic field. Device D performed the best: it showed a well defined plateau with a relative deviation of  $8 \cdot 10^{-5}$  from the ideal value above 7 tesla for negative fields, and the deviation in  $R_{xy}$  was approaching the same value at the maximum positive field.

Our interpretation of these results is the following. The measured deviation of  $R_{xy}$  from the ideal value is affected not only by defective behavior of the devices, but also by the imprecision of the current source and the voltmeters. In these measurements, different voltmeters (or, at least, different channels of a two-channel voltmeter) were used on different devices. However, in a separate check, the result on a particular device did not depend on which voltmeter was used, within the relative precision of  $10^{-5}$ . This leads to a conclusion that all voltmeters either were sufficiently precise or had the same systematic error; either way, they could not have caused different values of  $R_{xy}$  to be measured. The possible systematic error of the current source could not have caused the discrepancies, either, because a single source was used for all four devices. Therefore, Hall resistance in the four devices was actually different, which we attribute to defective behavior of devices A-C. The device D, however, did show what appears to be a fully developed plateau, and since neither the current source nor the voltmeters were calibrated, measurement error on the level of  $10^{-4}$  is to be expected. We conclude that the device D has performed correctly within the measurement precision of  $10^{-4}$  at negative fields above 7 tesla, and would likely have performed similarly at higher positive fields as well.

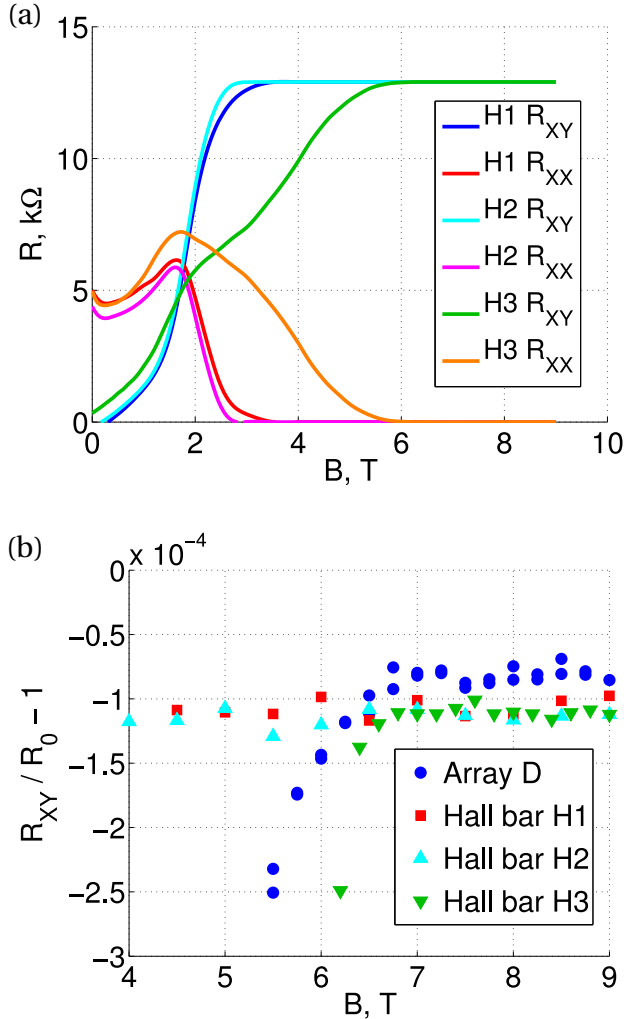


Figure 6.7: (a)  $R_{xy}$  and  $R_{xx}$  as a function of magnetic field in three single Hall bars: H1, H2 and H3. Measurements at negative fields were not performed since it was sufficient to achieve good quantization for one direction of the field. (b) Relative deviation of  $R_{xy}$  for the array D and three Hall bars at the strongest fields (positive fields for the Hall bars, negative fields for the array).  $R_0 = R_K/2$  for single Hall bars and  $-R_K/200$  for the array. The discrepancy between the single Hall bars and the array is attributed to the imprecision of the voltmeter at different ranges.

A hint at the possible reason for the defective behavior of arrays A-C is provided by measurements on single Hall bars that were fabricated on the same chip. As can be seen in Figure 6.7 a and b,  $R_{xy}$  in the array D as well as in Hall bars H1 and H2 reaches 1% precision around 3 tesla. The Hall bars H1 and H2 go on to reach the best observed precision at 4 or 4.5 Tesla, which we assume to be the normal behavior of the material at this carrier density. However, the array D reaches its best precision only at 7 tesla (Figure 6.7b). That could happen if a few Hall bars in the array had a plateau starting at higher fields due to non-uniform doping, similar to what was observed in the device H3. A similar but more severe problem could be a possible reason for the observed behavior of arrays B and C which did not show fully developed plateaus up to 9 Tesla. We attribute this non-uniform doping to the mechanical instability of the polymers used for photochemical gating, a problem described in section 3.1. If this is the case, the problem can be avoided by using other methods of controlling the carrier density, such as doping by exposure to different environments [136, 137] or gating by corona discharge (section 3.2), which should allow making a metrologically accurate array on graphene.



# Summary and outlook

Reliable mass-production of quantum Hall devices on epitaxial graphene is not straightforward. One of the issues on the way to this goal is achieving the correct carrier density in the material after fabrication. We have found that one of the techniques previously used, namely photochemical gating, is not sufficiently reliable for practical applications due to problems with mechanical stability of the polymer layer. At the same time, we have introduced a new method of gating by corona discharge, and demonstrated that it allows to perform well-reproducible measurements in the quantum Hall regime. This is a valuable addition to the arsenal of available techniques, which also includes such methods as electrolyte gating and environmental doping.

Another important issue is the inevitable presence of bilayer. We distinguish three possible transport regimes for the bilayer patches: they can be either metallic (which is the most common situation), insulating or in the quantum Hall regime with a filling factor different from that in the monolayer. The first two regimes have been observed in our experiments. When a bilayer region completely crosses a quantum Hall device, the device will be broken, which we have confirmed by a direct measurement in the metallic regime, and expect to happen for the other two regimes as well. Therefore, avoiding huge bilayer patches that run all the way from one side of the device to the other is of utmost importance.

The way to prevent the quantum Hall devices from being ruined by the bilayer is to select a substrate where the bilayer patches are sufficiently small and sparse. For this, a time-efficient way to image the patches is a must. To this end, we have shown that, by using simple real-time digital post-processing, it is possible to see the bilayer patches in an optical microscope, despite the small contrast. This allows visual inspection of the bilayer content across a centimeter-size wafer in a matter of minutes, thus determining whether or not the substrate is suitable for fabricating quantum Hall devices.

Finally, we have undertaken the task of making a quantum Hall array with 100 Hall bars on epitaxial graphene. In order for the array to work, every in-

dividual element of it must perform correctly, which requires a completely new level of reliability from the graphene technology. We have identified a class of substrates with sufficiently low bilayer content, and adapted the geometry of a Hall bar to the shape of the bilayer patches to make sure that the patches will not disrupt the performance of the devices. One out of four fabricated arrays has performed correctly within the measurement precision, and we theorize that the observed defective behavior was related to the unreliable photochemical gating that we were using, rather than to the properties of the material. This would mean that the quality of the available epitaxial graphene is already sufficient for it to replace gallium arsenide as a platform for quantum Hall devices, and making further technological improvements is the only thing remaining before graphene can become the new material of choice for quantum resistance metrology. In particular, the experiments with quantum Hall arrays need to be redone with a better carrier density control, and long-term stability of the devices needs to be better investigated. The instability of contact resistance (see Appendix B, section B.3) also merits a more detailed study.

## Appendix A

# Arbitrary multiple-parallel connection

Consider a circuit consisting of  $N$  Hall bars with  $2K$  contacts each in a multiple-parallel connection (Figure A.1). Potential at point  $C_j$  for each Hall bar is the same since these points are connected together:

$$\phi_{ij} + \epsilon_{ij} R_H I_{ij} = \phi_{1j} + \epsilon_{1j} R_H I_{1j}$$

A similar equation can be written for contact number  $j + 1$ :

$$\phi_{i,j+1} + \epsilon_{i,j+1} R_H I_{i,j+1} = \phi_{1,j+1} + \epsilon_{1,j+1} R_H I_{1,j+1}$$

Subtracting the two equations, taking into account that  $\phi_{i,j+1} - \phi_{ij} = R_H I_{i,j+1}$  according to (1.16) (for  $R_H > 0$ ), gives

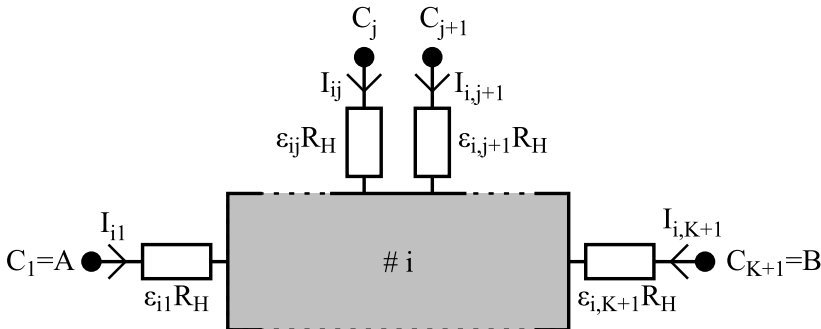


Figure A.1: Arbitrary multiple-parallel connection of any number of Hall bars

$$R_H(1 + \epsilon_{i,j+1})I_{i,j+1} - \epsilon_{ij}R_H I_{ij} = R_H(1 + \epsilon_{1,j+1})I_{1,j+1} - \epsilon_{1j}R_H I_{1j}$$

which under the assumption  $\epsilon_{ij} \ll 1$  simplifies to

$$I_{i,j+1} \approx I_{1,j+1} + \epsilon_{ij}I_{ij} - \epsilon_{1j}I_{1j} \quad (\text{A.1})$$

Substituting (A.1) into Kirchhoff's law  $I_{1,j+1} + I_{2,j+1} + \dots + I_{N,j+1} = 0$  yields an expression for  $I_{1,j+1}$ , and then (A.1) can be used one more time to find  $I_{i,j+1}$ :

$$I_{i,j+1} = \epsilon_{ij}I_{ij} - \frac{1}{N} \sum_{n=1}^N \epsilon_{nj}I_{nj}$$

The currents in source and drain electrodes are  $I_{i,1} \approx I/N$  and  $I_{i,K} \approx -I/N$ , thus

$$\begin{aligned} I_{i,j} &= O(e^{j-1}) \cdot I/N \\ I_{i,j+K} &= O(e^{j-1}) \cdot I/N \end{aligned}, \quad j \leq K \quad (\text{A.2})$$

Next, voltage difference between outer voltage probes number  $j$  and  $j + K$  (points  $C_j$  and  $C_{j+K}$ ) is

$$\begin{aligned} V_j - V_{j+K} &= \phi_{ij} + \epsilon_{ij}R_H I_{ij} - \phi_{i,j+K} - \epsilon_{i,j+K}R_H I_{i,j+K} = \\ &= - \sum_{n=1}^K (\phi_{i,j+n} - \phi_{i,j+n-1}) + R_H (\epsilon_{ij}I_{ij} - \epsilon_{i,j+K}I_{i,j+K}) = \\ &= R_H (-I_{i,j+1} - I_{i,j+2} - \dots - I_{i,K+1} - \dots - I_{i,j+K} + \epsilon_{ij}I_{ij} - \epsilon_{i,j+K}I_{i,j+K}) \end{aligned}$$

where (1.16) has been used to obtain the last expression. After averaging over all  $i = 1 \dots N$ , this becomes

$$V_j - V_{j+K} = R_H \left( \frac{I}{N} + \sum_{i=1}^N \epsilon_{ij}I_{ij} - \sum_{i=1}^N \epsilon_{i,j+K}I_{i,j+K} \right)$$

since  $\sum_{i=1}^N I_{i,K+1} = -I$  and all other  $\sum_{i=1}^N I_{i,j+n} = 0$ . Taking into account (A.2), we finally get

$$V_j - V_{j+K} = \frac{R_H}{N} I \left( 1 + O(e^j) \right), \quad 1 \leq j \leq K$$

The result for  $R_H < 0$  (the second of equations 1.18) is obtained in a similar way.

# Appendix B

## Fabrication recipes

Each major fabrication step contains e-beam lithography which involves spin-coating the sample with e-beam resist. Spinning speed and the dilution ratio of the resist are not always specified; these parameters are to be determined from the resist thickness. For a small chip such as 7x7 mm, it is important to spin fast enough so as to avoid excessive edge beading. The thickest resist layers (such as 500 nm or more of P(MMA-MAA)) should be made by spinning a thinner layer two or three times in a row.

### B.1 Lift-off deposition

- Spin-coat P(MMA-MAA), resist thickness should exceed the height of the highest structure present after the deposition.
- Bake for 2 minutes at 160° C on a hot plate.
- Spin-coat ARP, thickness is unimportant. In this work: ARP 6200.09 (6200/2) diluted 2:1 in anisole at 4000 RPM, 100 nm thick.
- Bake for 2 minutes at 160° C on a hot plate.
- Expose with e-beam at 50 kV with dose  $250 \mu\text{C}/\text{cm}^2$ .
- Develop for 30 seconds in o-xylene or hexyl acetate.
- Rinse for 5 seconds in isopropanol, rinse another 5 seconds in a different vessel of isopropanol, blow dry with nitrogen.
- Develop for 2 minutes in a mixture of isopropanol and water (93:7 by volume), blow dry with nitrogen.

- If needed, remove graphene with oxygen plasma: 30 seconds at 50 W in BatchTop RIE.
- Perform the deposition.
- Lift off the extra material in acetone for 10 hours.
- Rinse with acetone, rinse with isopropanol, blow dry with nitrogen.

## B.2 Patterning graphene

- Spin-coat P(MMA-MAA), 300+ nm thick. In this work: 10% solution in ethyl lactate at 6000 RPM, 350 nm thick.
- Bake for 2 minutes at 160° C on a hot plate.
- Expose with e-beam at 50 kV with dose 500  $\mu\text{C}/\text{cm}^2$ .
- Develop in a mixture of isopropanol and water (93:7 by volume) for 1 minute, blow dry with nitrogen.
- Oxygen plasma etching: 1 minute at 50 W in BatchTop RIE.
- Strip the resist in acetone for 10 hours, rinse with isopropanol, blow dry with nitrogen.

## B.3 Suggested sequence for fabricating the quantum Hall array

- Lift-off deposition of alignment marks, bonding pads, and leads to the devices: 5 nm Ti, 50 nm Au (e-beam evaporation), P(MMA-MAA) 100+ nm thick, with graphene removal. Let leads to single Hall bars extend all the way to the location of contacts.
- Lift-off deposition of contacts: 5 nm Ti, 50 nm Au, P(MMA-MAA) 100+ nm thick, no graphene removal. From this point on, contact resistance in single Hall bars can be checked at any time. We have observed that some of the contacts can sometimes obtain high resistance following spin-coating and removing the resist, whereafter larger contacts can be deposited on top of the old ones to restore low contact resistance.
- Graphene patterning by oxygen plasma.

### *B.3. SUGGESTED SEQUENCE FOR FABRICATING THE QUANTUM HALL ARRAY*<sup>83</sup>

- Lift-off deposition of vertical interconnecting wires: 5 nm Ti, 100 nm Au (e-beam evaporation), P(MMA-MAA) 150+ nm thick, with graphene removal.
- Lift-off deposition of the insulation: 200 nm silicon oxide (e-beam evaporation), P(MMA-MAA) 500+ nm thick, with graphene removal.
- Lift-off deposition of the horizontal interconnecting wires: 5 nm Ti, 300 nm Au (e-beam evaporation), P(MMA-MAA) 800+ nm thick, with graphene removal.
- Optionally: let interconnecting wires end short of the contacts, check that there is no electrical connection between any contacts at this point, then deposit the missing parts of the interconnects.



# Bibliography

- [1] F. Schopfer and W. Poirier, “Testing universality of the quantum Hall effect by means of the Wheatstone bridge,” *Journal of Applied Physics* **102** no. 5, (2007) 054903.
- [2] F. Schopfer and W. Poirier, “Quantum resistance standard accuracy close to the zero-dissipation state,” *Journal of Applied Physics* **114** no. 6, (2013) 064508. <http://arxiv.org/pdf/1301.5241>.
- [3] F. Piquemal, A. Bounouh, L. Devoille, N. Feltin, O. Thevenot, and G. Trapon, “Fundamental electrical standards and the quantum metrological triangle,” *Comptes Rendus Physique* **5** no. 8, (2004) 857–879.
- [4] A. A. Penin, “Quantum Hall effect in quantum electrodynamics,” *Physical Review B* **79** no. 11, (2009) 113303. <http://arxiv.org/pdf/0809.0486>.
- [5] G. Trapon, O. Thévenot, J. Lacueille, and W. Poirier, “Determination of the von Klitzing constant  $R_K$  in terms of the BNM calculable capacitor—fifteen years of investigations,” *Metrologia* **40** no. 4, (2003) 159.
- [6] P. J. Mohr, B. N. Taylor, and D. B. Newell, “CODATA Recommended Values of the Fundamental Physical Constants: 2010a,” *Journal of Physical and Chemical Reference Data* **41** no. 4, (2012) 043109. <http://arxiv.org/pdf/1203.5425>.
- [7] R. Ribeiro-Palau, F. Lafont, J. Brun-Picard, D. Kazazis, A. Michon, F. Cheynis, O. Couturaud, C. Consejo, B. Jouault, W. Poirier, and F. Schopfer, “Graphene surpasses GaAs/AlGaAs for the application of the quantum Hall effect in metrology,” arXiv:1504.06511v1 [cond-mat.mes-hall].

- [8] T. J. B. M. Janssen, S. Rozhko, I. Antonov, A. Tzalenchuk, J. M. Williams, Z. Melhem, H. He, S. Lara-Avila, S. Kubatkin, and R. Yakimova, "Operation of graphene quantum Hall resistance standard in a cryogen-free table-top system," *2D Materials* **2** no. 3, (2015) 035015, [arXiv:1507.04601](https://arxiv.org/abs/1507.04601) [cond-mat.mes-hall].
- [9] J. Alexander-Webber, A. Baker, T. Janssen, A. Tzalenchuk, S. Lara-Avila, S. Kubatkin, R. Yakimova, B. Piot, D. Maude, and R. Nicholas, "Phase Space for the Breakdown of the Quantum Hall Effect in Epitaxial Graphene," *Physical review letters* **111** no. 9, (2013) 096601. <http://arxiv.org/pdf/1304.4897>.
- [10] T. Janssen, J. Williams, N. Fletcher, R. Goebel, A. Tzalenchuk, R. Yakimova, S. Lara-Avila, S. Kubatkin, and V. Fal'ko, "Precision comparison of the quantum Hall effect in graphene and gallium arsenide," *Metrologia* **49** no. 3, (2012) 294. <http://arxiv.org/pdf/1202.2985>.
- [11] F. Lafont, R. Ribeiro-Palau, D. Kazazis, A. Michon, O. Couturaud, C. Consejo, T. Chassagne, M. Zielinski, M. Portail, B. Jouault, F. Schopfer, and W. Poirier, "Quantum Hall resistance standards from graphene grown by chemical vapour deposition on silicon carbide," *Nat Comms* **6** (Apr, 2015) 6806. <http://arxiv.org/pdf/1407.3615v2>.
- [12] A. Satrapinski, S. Novikov, and N. Lebedeva, "Precision quantum Hall resistance measurement on epitaxial graphene device in low magnetic field," *Applied Physics Letters* **103** no. 17, (2013) 173509. <http://arxiv.org/pdf/1308.0456>.
- [13] K. S. Novoselov, A. K. Geim, S. V. Morozov, D. Jiang, Y. Zhang, S. V. Dubonos, I. V. Grigorieva, and A. A. Firsov, "Electric Field Effect in Atomically Thin Carbon Films," *Science* **306** no. 5696, (2004) 666–669, <http://www.sciencemag.org/content/306/5696/666.full.pdf>.
- [14] C. Berger, Z. Song, T. Li, X. Li, A. Y. Ogbazghi, R. Feng, Z. Dai, A. N. Marchenkov, E. H. Conrad, P. N. First, and W. A. de Heer, "Ultrathin epitaxial graphite: 2D electron gas properties and a route toward graphene-based nanoelectronics," *The Journal of Physical Chemistry B* **108** no. 52, (2004) 19912–19916. <http://arxiv.org/pdf/cond-mat/0410240>.

- [15] P. R. Wallace, "The Band Theory of Graphite," *Phys. Rev.* **71** (May, 1947) 622–634.
- [16] E. McCann, "Electronic properties of monolayer and bilayer graphene," in *Graphene Nanoelectronics*, pp. 237–275. May, 2012. arXiv:1205.4849v1 [cond-mat.mes-hall].
- [17] E. McCann and M. Koshino, "The electronic properties of bilayer graphene," *Reports on Progress in Physics* **76** no. 5, (2013) 056503. <http://arxiv.org/pdf/1205.6953>.
- [18] J. B. Oostinga, H. B. Heersche, X. Liu, A. F. Morpurgo, and L. M. Vandersypen, "Gate-induced insulating state in bilayer graphene devices," *Nature materials* **7** no. 2, (2008) 151–157.
- [19] W. Zhu, V. Perebeinos, M. Freitag, and P. Avouris, "Carrier scattering, mobilities, and electrostatic potential in monolayer, bilayer, and trilayer graphene," *Physical Review B* **80** no. 23, (2009) 235402. <http://arxiv.org/pdf/0908.0749>.
- [20] K. Nomura and A. MacDonald, "Quantum transport of massless dirac fermions," *Physical review letters* **98** no. 7, (2007) 076602. [http://www.researchgate.net/profile/A\\_Macdonald/publication/6448259\\_Quantum\\_transport\\_of\\_massless\\_Dirac\\_fermions/links/00b495171be55029a9000000.pdf](http://www.researchgate.net/profile/A_Macdonald/publication/6448259_Quantum_transport_of_massless_Dirac_fermions/links/00b495171be55029a9000000.pdf).
- [21] E. Hwang, S. Adam, and S. D. Sarma, "Carrier transport in two-dimensional graphene layers," *Physical Review Letters* **98** no. 18, (2007) 186806. <http://arxiv.org/pdf/cond-mat/0610157>.
- [22] J. Martin, N. Akerman, G. Ulbricht, T. Lohmann, J. Smet, K. Von Klitzing, and A. Yacoby, "Observation of electron–hole puddles in graphene using a scanning single-electron transistor," *Nature Physics* **4** no. 2, (2008) 144–148. <http://arxiv.org/pdf/0705.2180>.
- [23] D. B. Farmer, V. Perebeinos, Y.-M. Lin, C. Dimitrakopoulos, and P. Avouris, "Charge trapping and scattering in epitaxial graphene," *Physical Review B* **84** no. 20, (2011) 205417. [http://researcher.ibm.com/files/us-vperebe/Farmer\\_trap.pdf](http://researcher.ibm.com/files/us-vperebe/Farmer_trap.pdf).
- [24] P. Wehrfritz and T. Seyller, "The Hall coefficient: a tool for characterizing graphene field effect transistors," *2D Materials* **1** no. 3, (2014) 035004.

- [25] S. D. Sarma, S. Adam, E. Hwang, and E. Rossi, "Electronic transport in two-dimensional graphene," *Reviews of Modern Physics* **83** no. 2, (2011) 407. <http://arxiv.org/pdf/1003.4731>.
- [26] E. Fradkin, "Critical behavior of disordered degenerate semiconductors. II. Spectrum and transport properties in mean-field theory," *Physical Review B* **33** no. 5, (1986) 3263.
- [27] A. W. Ludwig, M. P. Fisher, R. Shankar, and G. Grinstein, "Integer quantum Hall transition: An alternative approach and exact results," *Physical Review B* **50** no. 11, (1994) 7526. <https://www.kitp.ucsb.edu/sites/default/files/users/mpaf/publications/p47.pdf>.
- [28] N. H. Shon and T. Ando, "Quantum transport in two-dimensional graphite system," *Journal of the Physical Society of Japan* **67** no. 7, (1998) 2421–2429.
- [29] M. Katsnelson, "Zitterbewegung, chirality, and minimal conductivity in graphene," *The European Physical Journal B-Condensed Matter and Complex Systems* **51** no. 2, (2006) 157–160.
- [30] J. Tworzydło, B. Trauzettel, M. Titov, A. Rycerz, and C. W. Beenakker, "Sub-Poissonian shot noise in graphene," *Physical Review Letters* **96** no. 24, (2006) 246802. <http://arxiv.org/pdf/cond-mat/0603315>.
- [31] A. K. Geim and K. S. Novoselov, "The rise of graphene," *Nature materials* **6** no. 3, (2007) 183–191. <http://arxiv.org/pdf/cond-mat/0702595>.
- [32] K. v. Klitzing, G. Dorda, and M. Pepper, "New method for high-accuracy determination of the fine-structure constant based on quantized Hall resistance," *Physical Review Letters* **45** no. 6, (1980) 494. <http://lamp.tu-graz.ac.at/~hadley/ss2/IQHE/klitzingPRL.pdf>.
- [33] J. Schurr, J. Melcher, K. Pierz, G. Hein, and F.-J. Ahlers, "The width of AC quantum Hall plateaus," *Instrumentation and Measurement, IEEE Transactions on* **53** no. 3, (2004) 826–829.
- [34] J. Weis and K. Von Klitzing, "Metrology and microscopic picture of the integer quantum Hall effect," *Philosophical Transactions of the Royal Society A: Mathematical, Physical and Engineering Sciences* **369** no. 1953, (2011) 3954–3974.

- [35] E. Ahlswede, P. Weitz, J. Weis, K. Von Klitzing, and K. Eberl, "Hall potential profiles in the quantum Hall regime measured by a scanning force microscope," *Physica B: Condensed Matter* **298** no. 1, (2001) 562–566.
- [36] K. Güven and R. R. Gerhardt, "Self-consistent local equilibrium model for density profile and distribution of dissipative currents in a Hall bar under strong magnetic fields," *Physical Review B* **67** no. 11, (2003) 115327. <http://arxiv.org/pdf/cond-mat/0210186>.
- [37] L. Landau, "Diamagnetismus der metalle," *Zeitschrift für Physik* **64** no. 9-10, (1930) 629–637.
- [38] [http://en.wikipedia.org/wiki/Landau\\_quantization](http://en.wikipedia.org/wiki/Landau_quantization).
- [39] A. H. MacDonald, T. M. Rice, and W. F. Brinkman, "Hall voltage and current distributions in an ideal two-dimensional system," *Phys. Rev. B* **28** (Sep, 1983) 3648–3650.
- [40] S. A. Trugman, "Localization, percolation, and the quantum Hall effect," *Phys. Rev. B* **27** (Jun, 1983) 7539–7546.
- [41] R. Joynt and R. E. Prange, "Conditions for the quantum Hall effect," *Phys. Rev. B* **29** (Mar, 1984) 3303–3317.
- [42] R. B. Laughlin, "Quantized Hall conductivity in two dimensions," *Phys. Rev. B* **23** (May, 1981) 5632–5633.
- [43] B. I. Halperin, "Quantized Hall conductance, current-carrying edge states, and the existence of extended states in a two-dimensional disordered potential," *Physical Review B* **25** no. 4, (1982) 2185. <http://sites.fas.harvard.edu/~phys191r/References/e3/halperin1982.pdf>.
- [44] D. Yoshioka, ed., *The Quantum Hall Effect*. Springer-Verlag Berlin Heidelberg, 2002.
- [45] Q. Niu, D. J. Thouless, and Y.-S. Wu, "Quantized Hall conductance as a topological invariant," *Physical Review B* **31** no. 6, (1985) 3372. <http://content.lib.utah.edu/utils/getfile/collection/uspace/id/2339/filename/1446.pdf>.

- [46] R. Kubo, "Statistical-mechanical theory of irreversible processes. I. General theory and simple applications to magnetic and conduction problems," *Journal of the Physical Society of Japan* **12** no. 6, (1957) 570–586.  
<http://journals.jps.jp/doi/abs/10.1143/JPSJ.12.570>;  
<http://staff.ulsu.ru/moliver/ref/kubo/kubo57.pdf>.
- [47] P. Allen, "Chapter 6 Electron Transport," in *Conceptual Foundations of Materials – A Standard Model for Ground- and Excited-State Properties*, S. G. Louie and M. L. Cohen, eds., vol. 2 of *Contemporary Concepts of Condensed Matter Science*, pp. 165–218. Elsevier, 2006.
- [48] M. Kohmoto, "Topological invariant and the quantization of the Hall conductance," *Annals of Physics* **160** no. 2, (1985) 343–354.
- [49] Q. Niu and D. Thouless, "Quantised adiabatic charge transport in the presence of substrate disorder and many-body interaction," *Journal of Physics A: Mathematical and General* **17** no. 12, (1984) 2453.
- [50] D. Thouless, "Topological interpretations of quantum Hall conductance," *Journal of Mathematical Physics* **35** no. 10, (1994) 5362–5372. <http://scitation.aip.org/content/aip/journal/jmp/35/10/10.1063/1.530757>.
- [51] A. S. Schwarz, *Topology for physicists*, vol. 308. Springer Science & Business Media, 1994.  
<http://www.springer.com/book/9783540547549>.
- [52] C. Nash and S. Sen, *Topology and Geometry for Physicists*. Academic Press, 1988.
- [53] K. Ishikawa and T. Matsuyama, "A microscopic theory of the quantum Hall effect," *Nuclear Physics B* **280** (1987) 523–548.
- [54] N. Imai, K. Ishikawa, T. Matsuyama, and I. Tanaka, "Field theory in a strong magnetic field and the quantum Hall effect: Integer Hall effect," *Physical Review B* **42** no. 16, (1990) 10610.
- [55] K. Ishikawa, N. Maeda, and K. Tadaki, "Integer Quantum Hall Effect with Realistic Boundary Condition : Exact Quantization and Breakdown," *Phys. Rev. B* **54** (Apr., 1996) 17819,  
[arXiv:cond-mat/9507086v2](https://arxiv.org/abs/cond-mat/9507086v2) [cond-mat].  
<http://arxiv.org/pdf/cond-mat/9507086v2>.

- [56] J. Kinoshita, K. Inagaki, C. Yamanouchi, J. Moriyama, S. Kawaji, *et al.*, “High precision measurements of the hall effect for silicon mos inversion layers in strong magnetic fields,” *Surface Science* **113** no. 1, (1982) 16–21.
- [57] G. Eber, K. Von Klitzing, K. Ploog, and G. Weinmann, “Two-dimensional magneto-quantum transport on GaAs-AlxGa1-xAs heterostructures under non-ohmic conditions,” *Journal of Physics C: Solid State Physics* **16** no. 28, (1983) 5441.
- [58] M. Cage, R. Dziuba, B. Field, E. Williams, S. Girvin, A. Gossard, D. Tsui, and R. Wagner, “Dissipation and dynamic nonlinear behavior in the quantum Hall regime,” *Physical review letters* **51** no. 15, (1983) 1374.
- [59] F. Kuchar, G. Bauer, G. Weimann, and H. Burkhard, “Non-equilibrium behaviour of the two-dimensional electron gas in the quantized Hall resistance regime of GaAs/Al 0.3 Ga 0.7 As,” *Surface Science* **142** no. 1, (1984) 196–202.
- [60] M. Cage, B. Field, R. Dziuba, S. Girvin, A. Gossard, and D. Tsui, “Temperature dependence of the quantum Hall resistance,” *Physical Review B* **30** no. 4, (1984) 2286.
- [61] B. Jeckelmann and B. Jeanneret, “The quantum Hall effect as an electrical resistance standard,” *Measurement Science and Technology* **14** no. 8, (2003) 1229. [https://nanoelectronics.unibas.ch/education/MesoPhysics/Quantum\\_Hall\\_Metrology.pdf](https://nanoelectronics.unibas.ch/education/MesoPhysics/Quantum_Hall_Metrology.pdf).
- [62] S. Kawaji, K. Hirakawa, M. Nagata, T. Okamoto, T. Fukuse, and T. Gotoh, “Breakdown of the quantum Hall effect in GaAs/AlGaAs heterostructures due to current,” *Journal of the Physical Society of Japan* **63** no. 6, (1994) 2303–2313.
- [63] A. Boisen, P. Bo, A. Kristensen, P. Lindelof, *et al.*, “Nonlinear current-voltage characteristics at quantum Hall resistance minima,” *Physical Review B* **50** no. 3, (1994) 1957.
- [64] R. Haug, K. von Klitzing, and K. Ploog, “Hot Electron Magnetotransport in AlxGa1-xAs-GaAs Samples of Different Geometry,” in *High Magnetic Fields in Semiconductor Physics II*, pp. 185–189. Springer, 1989. [http://link.springer.com/chapter/10.1007/978-3-642-83810-1\\_29](http://link.springer.com/chapter/10.1007/978-3-642-83810-1_29).

- [65] N. Balaban, U. Meirav, and H. Shtrikman, "Crossover between different regimes of current distribution in the quantum Hall effect," *Physical Review B* **52** no. 8, (1995) R5503.
- [66] S. Komiyama, T. Takamasu, S. Hiyamizu, and S. Sasa, "Breakdown of the quantum Hall effect due to electron heating," *Solid state communications* **54** no. 6, (1985) 479–484.
- [67] S. Komiyama and Y. Kawaguchi, "Heat instability of quantum Hall conductors," *Physical Review B* **61** no. 3, (2000) 2014.
- [68] s. G. Nachtwei, "Breakdown of the quantum Hall effect," *Physica E: Low-dimensional Systems and Nanostructures* **4** no. 2, (1999) 79–101. [http://www.iap.tu-bs.de/Forschung/quantentransport/artikel/1999\\_PhysicaE\\_Nachtwei.pdf](http://www.iap.tu-bs.de/Forschung/quantentransport/artikel/1999_PhysicaE_Nachtwei.pdf).
- [69] Y. Zhang, Z. Jiang, J. Small, M. Purewal, Y.-W. Tan, M. Fazlollahi, J. Chudow, J. Jaszczak, H. Stormer, and P. Kim, "Landau-level splitting in graphene in high magnetic fields," *Physical review letters* **96** no. 13, (2006) 136806. <http://arxiv.org/pdf/cond-mat/0602649>.
- [70] M. Ezawa, "Intrinsic Zeeman effect in graphene," *Journal of the Physical Society of Japan* **76** no. 9, (2007) 094701. <http://arxiv.org/pdf/0707.0353>.
- [71] S.-S. Feng and M. Mochena, "Analysis of the Zeeman effect on the energy spectrum in graphenes," *Journal of Experimental and Theoretical Physics* **113** no. 2, (2011) 276–281.
- [72] Z. F. Ezawa, *Quantum Hall Effects. Field Theoretical Approach and Related Topics*. World Scientific, 2 ed., 2008. <http://www.worldscientific.com/worldscibooks/10.1142/6242>.
- [73] W. Strupinski, K. Grodecki, A. Wysmolek, R. Stepniewski, T. Szkopek, P. Gaskell, A. Gruneis, D. Haberer, R. Bozek, J. Krupka, *et al.*, "Graphene epitaxy by chemical vapor deposition on SiC," *Nano letters* **11** no. 4, (2011) 1786–1791.
- [74] A. Bergvall, J. M. Carlsson, and T. Lofwander, "Destroyed quantum Hall effect in graphene with [0001] tilt grain boundaries," *arXiv:1408.0394* (Aug, 2014). <http://arxiv.org/abs/1408.0394>.

- [75] R. Ribeiro-Palau, F. Lafont, F. Schopfer, W. Poirier, V. Bouchiat, Z. Han, A. Cresti, A. Cummings, and S. Roche, "Quantum Hall effect in polycrystalline CVD graphene: grain boundaries impact," *APS March Meeting 2014* **G37.00008** (2014) .  
<http://meetings.aps.org/link/BAPS.2014.MAR.G37.8>.
- [76] W. Chen, H. Xu, L. Liu, X. Gao, D. Qi, G. Peng, S. C. Tan, Y. Feng, K. P. Loh, and A. T. S. Wee, "Atomic structure of the 6H-SiC(0001) nanomesh," *Surface Science* **596** no. 1–3, (2005) 176–186.
- [77] S. Goler, C. Coletti, V. Piazza, P. Pingue, F. Colangelo, V. Pellegrini, K. V. Emtsev, S. Forti, U. Starke, F. Beltram, and S. Heun, "Revealing the atomic structure of the buffer layer between SiC(0001) and epitaxial graphene," *Carbon* **51** no. 0, (2013) 249–254.
- [78] P. Lauffer, K. V. Emtsev, R. Graupner, T. Seyller, L. Ley, S. A. Reshanov, and H. B. Weber, "Atomic and electronic structure of few-layer graphene on SiC(0001) studied with scanning tunneling microscopy and spectroscopy," *Phys. Rev. B* **77** (Apr, 2008) 155426.
- [79] S.-H. Ji, J. Hannon, R. Tromp, V. Perebeinos, J. Tersoff, and F. Ross, "Atomic-scale transport in epitaxial graphene," *Nature materials* **11** no. 2, (2012) 114–119.
- [80] S. W. Poon, W. Chen, E. S. Tok, and A. T. Wee, "Probing epitaxial growth of graphene on silicon carbide by metal decoration," *Applied Physics Letters* **92** no. 10, (2008) 104102.
- [81] J. Robinson, X. Weng, K. Trumbull, R. Cavalero, M. Wetherington, E. Frantz, M. LaBella, Z. Hughes, M. Fanton, and D. Snyder, "Nucleation of epitaxial graphene on SiC (0001)," *Acs Nano* **4** no. 1, (2009) 153–158.
- [82] W. Norimatsu and M. Kusunoki, "Formation process of graphene on SiC (0001)," *Physica E: Low-dimensional Systems and Nanostructures* **42** no. 4, (2010) 691–694.
- [83] T. Ohta, N. C. Bartelt, S. Nie, K. Thürmer, and G. Kellogg, "Role of carbon surface diffusion on the growth of epitaxial graphene on SiC," *Physical Review B* **81** no. 12, (2010) 121411.
- [84] T. Shen, J. Gu, M. Xu, Y. Wu, M. Bolen, M. Capano, L. Engel, and P. Ye, "Observation of quantum-Hall effect in gated epitaxial graphene grown on SiC (0001)," *Applied Physics Letters* **95** no. 17, (2009) 172105.  
<http://arxiv.org/pdf/0908.3822>.

- [85] B. Jouault, N. Camara, B. Jabakhanji, A. Caboni, C. Consejo, P. Godignon, D. Maude, and J. Camassel, "Quantum Hall effect in bottom-gated epitaxial graphene grown on the C-face of SiC," *Applied Physics Letters* **100** no. 5, (2012) 052102. [http://www.researchgate.net/profile/Bilal\\_Jabakhanji/publication/257951505\\_Quantum\\_Hall\\_effect\\_in\\_bottom-gated\\_epitaxial\\_graphene\\_grown\\_on\\_the\\_C-face\\_of\\_SiC/links/54afd9060cf2255208dbaf6d.pdf](http://www.researchgate.net/profile/Bilal_Jabakhanji/publication/257951505_Quantum_Hall_effect_in_bottom-gated_epitaxial_graphene_grown_on_the_C-face_of_SiC/links/54afd9060cf2255208dbaf6d.pdf).
- [86] S. Lara-Avila, K. Moth-Poulsen, R. Yakimova, T. Bjørnholm, V. Fal'ko, A. Tzalenchuk, and S. Kubatkin, "Non-Volatile Photochemical Gating of an Epitaxial Graphene/Polymer Heterostructure," *Advanced Materials* **23** no. 7, (2011) 878–882. <http://www.physics.lancs.ac.uk/research/condmatt/theory/papers/000287668500011.pdf>.
- [87] S. Kopylov, A. Tzalenchuk, S. Kubatkin, and V. I. Fal'ko, "Charge transfer between epitaxial graphene and silicon carbide," *Applied Physics Letters* **97** (July, 2010) 112109, arXiv:1007.4340v1 [cond-mat.mtrl-sci].
- [88] T. J. B. M. Janssen, A. Tzalenchuk, R. Yakimova, S. Kubatkin, S. Lara-Avila, S. Kopylov, and V. I. Fal'ko, "Anomalously strong pinning of the filling factor  $\nu=2$  in epitaxial graphene," *Phys. Rev. B* **83** (Jun, 2011) 233402. <http://arxiv.org/pdf/1009.3450>.
- [89] F. F. Fang and P. J. Stiles, "Quantized magnetoresistance in multiply connected perimeters in two-dimensional systems," *Phys. Rev. B* **29** (Mar, 1984) 3749–3751.
- [90] M. Ortolano, M. Abrate, and L. Callegaro, "On the synthesis of quantum Hall array resistance standards," *Metrologia* **52** no. 1, (2015) 31. <http://arxiv.org/pdf/1311.0756>.
- [91] F. F. Fang and P. J. Stiles, "Quantized magnetoresistance in two-dimensional electron systems," *Phys. Rev. B* **27** (May, 1983) 6487–6488.
- [92] F. Delahaye, "Series and parallel connection of multiterminal quantum Hall-effect devices," *Journal of Applied Physics* **73** no. 11, (1993) 7914–7920.
- [93] L. Callegaro and M. Ortolano, "Bridge connection of quantum Hall elementary devices," arXiv:1310.5583v1 [physics.ins-det].

- [94] R. Haug, A. MacDonald, P. Streda, and K. Von Klitzing, "Quantized multichannel magnetotransport through a barrier in two dimensions," *Physical review letters* **61** no. 24, (1988) 2797.
- [95] D. Abanin and L. Levitov, "Quantized transport in graphene pn junctions in a magnetic field," *Science* **317** no. 5838, (2007) 641–643. <http://arxiv.org/pdf/0704.3608>.
- [96] D. Syphers and P. Stiles, "Contiguous two-dimensional regions in the quantized Hall regime," *Physical Review B* **32** no. 10, (1985) 6620.
- [97] J. Williams, L. DiCarlo, and C. Marcus, "Quantum Hall effect in a gate-controlled pn junction of graphene," *Science* **317** no. 5838, (2007) 638–641. <http://citeseerx.ist.psu.edu/viewdoc/download?doi=10.1.1.205.3671&rep=rep1&type=pdf>.
- [98] D.-K. Ki and H.-J. Lee, "Quantum Hall resistances of a multiterminal top-gated graphene device," *Physical Review B* **79** no. 19, (2009) 195327. <http://arxiv.org/pdf/0903.0213>.
- [99] D.-K. Ki, S.-G. Nam, H.-J. Lee, and B. Özyilmaz, "Dependence of quantum-Hall conductance on the edge-state equilibration position in a bipolar graphene sheet," *Physical Review B* **81** no. 3, (2010) 033301. <http://arxiv.org/pdf/0912.2791>.
- [100] J. Tian, Y. Jiang, I. Childres, H. Cao, J. Hu, and Y. P. Chen, "Quantum Hall effect in monolayer-bilayer graphene planar junctions," *Physical Review B* **88** no. 12, (2013) 125410. <http://arxiv.org/pdf/1308.4058>.
- [101] A. Iagallo, S. Tanabe, S. Roddaro, M. Takamura, Y. Sekine, H. Hibino, V. Miseikis, C. Coletti, V. Piazza, F. Beltram, *et al.*, "Bilayer-induced asymmetric quantum Hall effect in epitaxial graphene," *Semiconductor Science and Technology* **30** no. 5, (2015) 055007. <http://arxiv.org/pdf/1410.2024>.
- [102] T. Stauber, N. Peres, and A. Geim, "Optical conductivity of graphene in the visible region of the spectrum," *Physical Review B* **78** no. 8, (2008) 085432. <http://arxiv.org/pdf/0803.1802>.
- [103] L. Falkovsky and A. Varlamov, "Space-time dispersion of graphene conductivity," *The European Physical Journal B-Condensed Matter and Complex Systems* **56** no. 4, (2007) 281–284. <http://arxiv.org/pdf/cond-mat/0606800>.

- [104] L. Hao and L. Sheng, "Optical conductivity of multilayer graphene," *Solid State Communications* **149** no. 43, (2009) 1962–1966.
- [105] P. Blake, E. Hill, A. C. Neto, K. Novoselov, D. Jiang, R. Yang, T. Booth, and A. Geim, "Making graphene visible," *Applied Physics Letters* **91** no. 6, (2007) 063124. <http://ieeexplore.ieee.org/iel5/4816218/4830842/04830974.pdf?arnumber=4830974>.
- [106] X. Wang, M. Zhao, and D. D. Nolte, "Optical contrast and clarity of graphene on an arbitrary substrate," *Applied Physics Letters* **95** no. 8, (2009) 081102–081102. <https://www.physics.purdue.edu/quantum/files/CarbonNano/optical-contrast.pdf>.
- [107] A. Tzalenchuk, S. Lara-Avila, A. Kalaboukhov, S. Paolillo, M. Syväjärvi, R. Yakimova, O. Kazakova, T. Janssen, V. Fal'Ko, and S. Kubatkin, "Towards a quantum resistance standard based on epitaxial graphene," *Nature nanotechnology* **5** no. 3, (2010) 186–189.
- [108] R. Allen, G. David, and G. Nomarski, "The zeiss-Nomarski differential interference equipment for transmitted-light microscopy," *Zeitschrift für wissenschaftliche Mikroskopie und mikroskopische Technik* **69** no. 4, (1969) 193–221. <http://europemc.org/abstract/med/5361069>; [http://zeiss-campus.magnet.fsu.edu/referencelibrary/pdfs/Allen\\_etal\\_Zeit\\_Wissen\\_Mikro\\_Tech\\_69-193-1969.pdf](http://zeiss-campus.magnet.fsu.edu/referencelibrary/pdfs/Allen_etal_Zeit_Wissen_Mikro_Tech_69-193-1969.pdf).
- [109] W. Lang, "Nomarski differential interference-contrast microscopy," *Zeiss Information* **70** (1968) 114–120. [http://zeiss-campus.magnet.fsu.edu/referencelibrary/pdfs/lang\\_zeiss\\_information\\_76\\_69-76\\_1971.pdf](http://zeiss-campus.magnet.fsu.edu/referencelibrary/pdfs/lang_zeiss_information_76_69-76_1971.pdf).
- [110] N. Streibl, "Phase imaging by the transport equation of intensity," *Optics communications* **49** no. 1, (1984) 6–10.
- [111] M. Reed Teague, "Deterministic phase retrieval: a Green's function solution," *JOSA* **73** no. 11, (1983) 1434–1441.
- [112] R. Grella, "Fresnel propagation and diffraction and paraxial wave equation," *Journal of Optics* **13** no. 6, (1982) 367.
- [113] [http://en.wikipedia.org/wiki/Helmholtz\\_equation#Paraxial\\_approximation](http://en.wikipedia.org/wiki/Helmholtz_equation#Paraxial_approximation).
- [114] W. Yuan and G. Shi, "Graphene-based gas sensors," *Journal of Materials Chemistry A* **1** no. 35, (2013) 10078–10091.

- [115] L. Kong, A. Enders, T. S. Rahman, and P. A. Dowben, "Molecular adsorption on graphene," *Journal of Physics: Condensed Matter* **26** no. 44, (2014) 443001. [http://www.researchgate.net/profile/A\\_Enders/publication/266563299\\_Molecular\\_adsorption\\_on\\_graphene/links/547ca88e0cf2cfe203c1f9f3.pdf](http://www.researchgate.net/profile/A_Enders/publication/266563299_Molecular_adsorption_on_graphene/links/547ca88e0cf2cfe203c1f9f3.pdf).
- [116] H. Liu, Y. Liu, and D. Zhu, "Chemical doping of graphene," *Journal of materials chemistry* **21** no. 10, (2011) 3335–3345.
- [117] H. Pinto, R. Jones, J. Goss, and P. Briddon, "Mechanisms of doping graphene," *physica status solidi (a)* **207** no. 9, (2010) 2131–2136. <http://arxiv.org/pdf/1003.0624>.
- [118] Z. H. Ni, H. M. Wang, Z. Q. Luo, Y. Y. Wang, T. Yu, Y. H. Wu, and Z. X. Shen, "The effect of vacuum annealing on graphene," *Journal of Raman Spectroscopy* **41** no. 5, (2010) 479–483. <http://www1.spms.ntu.edu.sg/~yuting/Publications/Publication%202010/The%20effect%20of%20vacuum%20annealing%20on%20graphene.pdf>.
- [119] S. Tanabe, Y. Sekine, H. Kageshima, M. Nagase, and H. Hibino, "Half-integer quantum Hall effect in gate-controlled epitaxial graphene devices," *Applied Physics Express* **3** no. 7, (2010) 075102.
- [120] T. Shen, A. T. Neal, M. L. Bolen, J. Gu, L. W. Engel, M. A. Capano, and P. D. Ye, "Quantum-Hall plateau-plateau transition in top-gated epitaxial graphene grown on SiC (0001)," *Journal of Applied Physics* **111** no. 1, (2012) 013716. <http://arxiv.org/pdf/1112.4345>.
- [121] R. Williams and A. Willis, "Electron multiplication and surface charge on zinc oxide single crystals," *Journal of Applied Physics* **39** no. 8, (1968) 3731–3736.
- [122] R. Williams and M. Woods, "High electric fields in silicon dioxide produced by corona charging," *Journal of Applied Physics* **44** no. 3, (1973) 1026–1028.
- [123] D. Schroder, M. Fung, R. Verkuil, S. Pandey, W. Howland, and M. Kleefstra, "Corona-oxide-semiconductor device characterization," *Solid-State Electronics* **42** no. 4, (1998) 505–512.
- [124] R. Comizzoli, "Uses of corona discharges in the semiconductor industry," *Journal of the Electrochemical Society* **134** no. 2, (1987) 424–429.

- [125] T. Löfwander, P. San-Jose, and E. Prada, "Quantum Hall effect in graphene with twisted bilayer stripe defects," *Phys. Rev. B* **87** (May, 2013) 205429.
- [126] T. Yager, A. Lartsev, R. Yakimova, S. Lara-Avila, and S. Kubatkin, "Wafer-scale homogeneity of transport properties in epitaxial graphene on SiC," *Carbon* **87** (2015) 409–414.
- [127] V. Panchal, C. Giusca, A. Lartsev, R. Yakimova, and O. Kazakova, "Local electric field screening in bi-layer graphene devices," *Frontiers in Physics* **2** (2014) 3.
- [128] J. A. Kellar, J. M. Alaboson, Q. H. Wang, and M. C. Hersam, "Identifying and characterizing epitaxial graphene domains on partially graphitized SiC (0001) surfaces using scanning probe microscopy," *Applied Physics Letters* **96** no. 14, (2010) 143103. [http://faculty.engineering.asu.edu/wang/wp-content/uploads/2014/08/Kellar\\_APL\\_2010.pdf](http://faculty.engineering.asu.edu/wang/wp-content/uploads/2014/08/Kellar_APL_2010.pdf).
- [129] T. Burnett, R. Yakimova, and O. Kazakova, "Mapping of Local Electrical Properties in Epitaxial Graphene Using Electrostatic Force Microscopy," *Nano Letters* **11** no. 6, (2011) 2324–2328, <http://pubs.acs.org/doi/pdf/10.1021/nl200581g>.
- [130] J. Hong, S. Niyogi, E. Bekyarova, M. E. Itkis, P. Ramesh, N. Amos, D. Litvinov, C. Berger, W. A. de Heer, S. Khizroev, *et al.*, "Effect of nitrophenyl functionalization on the magnetic properties of epitaxial graphene," *Small* **7** no. 9, (2011) 1175–1180.
- [131] I. Jozwik-Biala, K. Gródecki, J. Baranowski, W. Strupinski, I. Pasternak, and A. Krajewska, "Low-kV SEM Imaging of Epitaxial Graphene Grown on Various Substrates," *Microscopy and Microanalysis* **20** no. S3, (2014) 18–19.
- [132] H. Hibino, H. Kageshima, F. Maeda, M. Nagase, Y. Kobayashi, Y. Kobayashi, and H. Yamaguchi, "Thickness determination of graphene layers formed on SiC using low-energy electron microscopy," *e-Journal of Surface Science and Nanotechnology* **6** (2008) 107–110.
- [133] H. Kageshima, H. Hibino, and M. Nagase, "Epitaxial Graphene Growth Studied by Low-Energy Electron Microscopy and First-Principles," in *Materials Science Forum*, vol. 645, pp. 597–602, Trans Tech Publ. 2010.

- [134] R. Yakimova, C. Virojanadara, D. Gogova, M. Syväjärvi, D. Siche, K. Larsson, and L. I. Johansson, "Analysis of the formation conditions for large area epitaxial graphene on SiC substrates," in *Materials Science Forum*, vol. 645, pp. 565–568, Trans Tech Publ. 2010.  
<http://www.diva-portal.org/smash/get/diva2:338101/FULLTEXT01.pdf>.
- [135] W. Poirier, A. Bounouh, K. Hayashi, H. Fhima, F. Piquemal, G. Genevès, and J. André, "RK/100 and RK/200 quantum Hall array resistance standards," *Journal of applied physics* **92** no. 5, (2002) 2844–2854.  
<http://arxiv.org/pdf/cond-mat/0203231>.
- [136] Y. Yang, L.-I. Huang, Y. Fukuyama, F.-H. Liu, M. A. Real, P. Barbara, C.-T. Liang, D. B. Newell, and R. E. Elmquist, "Low carrier density epitaxial graphene devices on SiC," *Small* **11** no. 1, (2015) 90–95.  
<http://arxiv.org/pdf/1404.1048>.
- [137] T. Yager, M. J. Webb, H. Grennberg, R. Yakimova, S. Lara-Avila, and S. Kubatkin, "High mobility epitaxial graphene devices via aqueous-ozone processing," *Applied Physics Letters* **106** no. 6, (2015) 063503. <http://www.diva-portal.org/smash/get/diva2:798868/FULLTEXT01.pdf>.

